Gustavo Corrêa Alves da Silva

Topological optimization of structures produced through 3D printing of fiber-reinforced cementitious materials

Topological optimization of structure produced through 3D printing of fiber reinforced cementitious

Gustavo Corrêa Alves da Silva

UMinho | 2021

janeiro de 2021

Universidade do Minho
Escola de Engenharia

Gustavo Corrêa Alves da Silva

Topological optimization of structures produced through 3D printing of fiber reinforced cementitious materials

Dissertação de Mestrado
Ciclo de Estudos Integrados Conducentes ao Grau de Mestre em Engenharia Civil

Trabalho efetuado sob a orientação do
Professor Doutor Vítor Manuel do Couto Fernandes da Cunha
Professor Doutor Eduardo Nuno Borges Pereira

Janeiro de 2021

DIREITOS DE AUTOR E CONDIÇÕES DE UTILIZAÇÃO DO TRABALHO POR TERCEIROS

Este é um trabalho académico que pode ser utilizado por terceiros desde que respeitadas as regras e boas práticas internacionalmente aceites, no que concerne aos direitos de autor e direitos conexos.

Assim, o presente trabalho pode ser utilizado nos termos previstos na licença abaixo indicado.

Caso o utilizador necessite de permissão para poder fazer um uso do trabalho em condições não previstas no licenciamento indicado, deverá contactar o autor, através do RepositórioUM da Universidade do Minho.

Licença concedida aos utilizadores deste trabalho

AGRADECIMENTOS

STATEMENT OF INTEGRITY

I hereby declare having conducted this academic work with integrity. I confirm that I have not used plagiarism or any form of undue use of information or falsification of results along the process leading to its elaboration. I further declare that I have fully acknowledged the Code of Ethical Conduct of the University of Minho.

ABSTRACT

Topology optimization can play an important role in the Architecture, Engineering and Construction (AEC) sector. This technology along with digital manufacturing can be a game changer in the future of civil construction, allowing to build, in a short time period, lighter constructions with very geometry complexity but keeping the same of even better structural functioning. These optimized structures when coupled with a material with high capacity efforts redistribution, e.g. fibre reinforced cementitious material (FRC), can partially or totally substitute   the conventional reinforcement, consequently less raw material is use, contributing for a better sustainable development.

Following this idea, this dissertation will focus on study topology optimization processes along with the use of FRC materials. Initially a comparison between some topology optimization software's will be carried out, in order to proper evaluate to most suitable for the realization of the present work. In a second stage, considering only the linear behavior of the material, different topology optimization analyses will be done. These analyses will be based on the geometry and the intended structural application (support and load conditions), in addition to the optimization goal (design variable and constraint). This part aims to assess the influence of height / length ratio (H/L ratio) of the beam, in the optimization outcome. After that, a study of the influence of reinforcement amount in the optimization will be done.

Afterwards, some finite element analysis (FEA) for one of the optimized structures will be performed and assessed using distinct approaches for obtaining the tensile stress – strain relationship, namely by adopting the ultimate limit state (USL) and service limit state (SLS) tensile diagrams according to the recommendations presented in FIB Model Code 2010. These simulations will serve to evaluate the nonlinear behavior of the FRC structure. For this study six FRC with different strength classes were considered. Finally, an optimized structural element obtained through the FEA was sliced for 3D printing and the influence of the nozzle dimensions, i.e. printing resolution was checked.

KEYWORDS: Digital manufacturing (3D printing), fiber-reinforced concrete (FRC), finite element analysis (FEA), Industry 4.0, Structural/topology optimization.

RESUMO

A otimização da topologia pode desempenhar um papel importante no setor de Arquitetura, Engenharia e Construção (AEC). Esta tecnologia aliada à manufatura digital pode completamente revolucionar o futuro da construção civil, permitindo construir, num curto espaço de tempo, construções mais leves, mas mantendo o mesmo ou ainda melhor funcionamento estrutural. Estas estruturas otimizadas quando conjugadas a um material com alta capacidade de redistribuição de esforços, por ex. materiais cimentícios reforçado com fibras (FRC), pode substituir parcial ou totalmente o reforço convencional, onde consequentemente menos matéria-prima será utilizada, contribuindo-se assim, para um melhor desenvolvimento sustentável.

Seguindo essa ideia, esta dissertação terá como foco estudar processos de otimização de topológica juntamente com o uso de materiais FRC. Inicialmente será realizada uma comparação entre alguns softwares de otimização de topológica, a fim de avaliar adequadamente o mais adequado para a realização do presente trabalho. Em uma segunda etapa, considerando apenas o comportamento linear do material, serão realizados diferentes processos de otimização topológica. Essas otimizações serão baseadas na geometria e na aplicação estrutural pretendida e no objetivo da otimização. Esta parte visa avaliar a influencia da relação altura/comprimento da viga (relação H/L), no resultado da otimização.

Posteriormente, algumas análises de elementos finitos (FEM) para uma das estruturas otimizadas serão realizadas e avaliadas usando duas abordagens distintas para a obtenção da relação tensão de tração – deformação, uma para estado limite último (ELU) e estado limite de serviço (ELS), seguindo as recomendações presentes no FIB Model Code 2010. Estas simulações servirão para avaliar o comportamento não linear da estrutura de FRC. Para este estudo foram considerados seis FRC com diferentes classes de força. Finalmente, para um elemento estrutural otimizado anteriormente, foi realizada uma simulação de impressão 3D, de modo a estudar a influencia do tamanho do bico de impressão, ou seja, a resolução de impressão foi verificada.

Palavras-Chave: Betão reforçado com fibra (FRC), impressão 3D, Indústria 4.0, método dos elementos finitos (MEF), Otimização estrutural/topológica.

CONTENTS

LIST OF FIGURES

LIST OF TABLES

1. INTRODUCTION

1.1 Problem Statement

The Industry Sector has had a great impact in the development of the modern world, being crucial to the increasingly life quality that society has been experiencing and demanding up to the modern times. In order to provide response to the societal necessities, the demand of raw materials has been rapidly increasing, especially in the Architecture, Engineering and Construction (AEC) industry, being the latter, one of the sectors that consumes more natural resources. With that said, due to the progressively increasing of awareness regarding sustainability issues, it becomes necessary to pursue constructions and structural elements that employ a rational material usage, but at the same time complying with their structural requirements.

Nowadays, with the developments on computer computation capacity, advanced numerical softwares based on the Finite Element Method (FEM) offer a panoply of features, being an example of those features structural optimization capabilities. Therefore, it becomes possible to design optimized structures, being this a step towards a contribution to an increasingly sustainable development. One problem that surges with this, is that most of the optimized structures / elements have an enhanced geometry complexity, becoming either almost impossible to manufacture through standard building techniques or with a very high cost, by e.g. in concrete structures, due to the higher cost of intricate formwork to accommodate the geometrical complexity.

Digital manufacturing is a new way to build, that promises to solve many problems related to the traditional construction methods. Athwart, this technology enables to build very complex geometries in a shorter time, as well as to obviate the cost regarding the geometrical complexity. Therefore, basically, this methodology will be of interest to manufacture structures / structural elements obtained through numerical topological optimization methods.

Following the aforementioned rational, one of the motivations for the research presented in this dissertation is to explore and employ topological optimization processes in structural elements to be produced through additive manufacturing techniques, a.k.a. 3D printing.

1.2 Objectives

Topology optimization of structures produced through 3D printing is a thematic that is increasingly acquiring the attention of the scientific community and consequently the attention of the construction sector with the advent of the digital fabrication of concrete, which enables the production of objects / elements with considerable higher geometrical complexity, when compared to the traditional construction methods. In spite of being a topic that has been studied for some time in the scientific community, still requires a lot of research and mainly integration with new digital construction technologies, such as additive manufacturing.

The main goal of the present dissertation aims to assess and deploy concepts inherent to industry 4.0, in the design, analysis and production of structures manufactured through 3D printing of cementitious materials reinforced with fibers. The topological optimization to be carried out will be based on the geometry and the intended structural application (support and load conditions), in addition to the optimization goal (design variable and constraint).

Initially the principal objective will be to do a profound study about the most known software's and tools that allow parametric modelling and topology optimization processes, in order to conclude that will be the most suitable, as well as that can successfully guarantee the interoperability between the design phase, optimization and analysis of the intended structure.

Then a study about the most suitable parameter's settings and optimization algorithms to be used during the topology optimization process. Moreover, the influence of other variables, such as by e.g. mesh refinement; optimization variables; etc will be assessed, in order to lead to the best optimization results possible. Afterwards, some optimization processes will be carried out, considering only the linear behavior of the material. Lastly some finite element analysis (FEA) will be done, but now considering the nonlinear behavior of fiber-reinforced cementitious material with distinct strength class strengths. This study, as stated before, will be used to evaluate the performance of the optimized structure along with the fiber reinforced cementitious material.

Finally, an optimized structural element obtained through the FEA was sliced for 3D printing and the influence of the nozzle dimensions, i.e. printing resolution was checked.

1.3 Dissertation Structure

The dissertation is organized as follows:

- Chapter 2 will be focused on a review of the different subjects inherent to this theme, such as by example the additive manufacturing techniques and topology optimization algorithms currently available. This task will make it possible to acquire knowledge in areas directly linked to the theme of this dissertation, namely: manufacturing practices currently used, innovative manufacturing practices, more specifically the most efficient processes of additive manufacturing / 3D printing and the most known topology optimization methodologies.

- Chapter 3 presents a survey of software's currently available that offer not only parametric modelling tools, but also finite element analysis (FEA) and topological optimization processes. It is important to state that regarding FEA, the software should provide nonlinear capabilities, since in the case of employing fiber-reinforced cementitious materials, which have enhanced residual strength and ductility are therefore their stress redistribution capability benefits are observed on the post-cracking stage.

- Chapter 4 focus on the topology optimization processes, considering only the linear behavior of the material. The goal is to conduct a study regarding the influence of distinct parameters in the optimization outcome, such as height to length of the beam ratio (H/L ratio), supports conditions, mesh refinement and variables in the optimization algorithm.

- Chapter 5 presents a parametric study regarding the nonlinear behavior for one of the optimized structural elements. The study will focus on the nonlinear structural behavior of a fiber-reinforced cementitious (FRC) beam with an optimized topology. The material laws for characterizing the tensile behavior of the FRC were defined accordingly distinct approaches proposed in the CEB-FIP Model Code 2010.

Chapter 6 draws the main conclusions of this dissertation and provides some outlook for future works development, namely on the numerical modelling of 3D printed FRC structural elements.

2. LITERATURE REVIEW

2.1 Industry 4.0

At a time where the industry is globally positioned as the engine of economic growth, thus playing a fundamental role in maintaining employment and social stability, the fast development of technology allows an unprecedented repositioning of the industrial sector (SIEMENS, 2017).

The industry, as it is known today, has suffered several changes / revolutions throughout history and has grown systematically, according to novel discoveries and developments that occurred during the course of the past centuries (Figure 1). The First Industrial Revolution started at the end of the 18th century, in which steam powered machines, have made possible a mechanized industrial production. Since then, other revolutions have changed the course and paradigms of the industrial production history. Between the end of the 19th century and the beginning of the 20th century, has arisen the Second Industrial Revolution, also known as electrical revolution, where factories began to operate and manufacture with power tools, which allowed to shift to mass production that unveiled a significant efficiency increase. The Third Industrial Revolution occurred in the seventies, and led to the emergence and evolution of computerized systems, allowing to fully automate the different industrial tasks during the production chain (Santos et al., 2018).
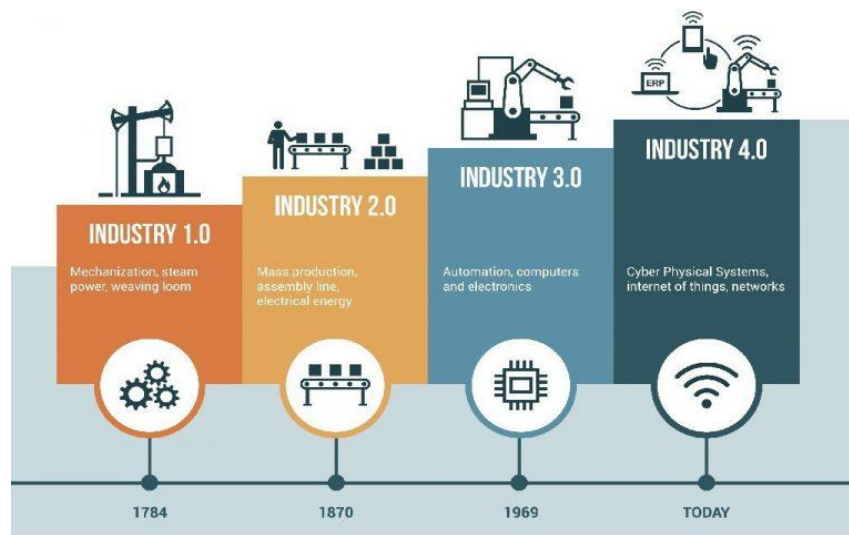
Figure 1 - The four industrial revolutions (The Fourth Industrial Revolution - CADM)

Today, society is experiencing a profound digital transformation at an industrial level. This revolution, called by Fourth Industrial Revolution or Industry 4.0, is characterized by the conceptual fusion of technologies that shorten the boundary between physical, digital and human systems. These changes are more visible in some more innovative sectors, such as aeronautic, automotive, electronics and biology industries, due to its commitment to overall efficiency and innovation (L. Barretoa et al., 2018). This transformation is strongly focused on continuous improvement of efficiency, safety and productivity of operations in order to maximize the return of the investments, made at the first place, in other words to maximize ROCE (Return on Capital Employed). In order to pursue the latter premises, Industry 4.0 is essentially based on nine pillars / technologies (Figure 2), mentioned below (Puskás & Bohács, 2019):

- Data and Analytics
- Autonomous Robots
- Simulation
- Horizontal and Vertical System Integration
- The Industrial Internet of Things
- Cybersecurity
- Cloud Computing
- Additive Manufacturing
- Augmented Reality

Figure 2 - Technological Pillars of industry 4.0 (Puskás & Bohács, 2019)

Many of these nine pillars, which form the foundation of Industry 4.0 philosophy, are nowadays in use in industrial manufacturing. Nonetheless, with the emergence and dissemination of the Industry 4.0 paradigms, they are being synergistically used in order to transform production. Therefore isolated, optimized cells will come together as a fully integrated, automated, and optimized production flow, making it possible gather and analyze data between machines, allowing faster, more flexible and more efficient production processes, generating high-quality and highly personalized products at reduced costs. This revolution will also change the traditional production relationships among suppliers, producers, and customers—as well as between human and machine (Gerbert et al., 2015). Finally, this revolution may also enable a shift on the industrial production paradigms, i.e. from a mass production towards a mass customization as well as from "make to stock" to "dynamic make to order".

The raw material usage and optimization of topological geometry of structures / structural elements has become an increasingly critical point in the Architecture, Engineering and Construction (AEC) sector, inherent to the increasingly more demanding sustainability requirements. While many strategies to reduce / optimize the amount of raw materials used, focus on the end of a building's life cycle by trying to employ circularity concepts based on recycling / reusing, on the other hand, there is a great potential to reduce the use of raw materials in the design and execution phases of a structural project. that the aforementioned, acquires special preponderance in materials that are more difficult to recycle, such as concrete (Allwood et al., 2011). Many techniques that aim to reduce / optimize material usage in the conception / project phase resort to the use of light concrete, or hollow sections, or even the use of pre-stress.

Currently, the optimization of raw materials in structures / structural elements may take advantage of numerical techniques, such as advanced computational methods currently available under the scope of the finite element method (FEM) that enable the optimization of size, shape, and topology, ensuring an adequate material / structural behavior while complying with a rational usage of raw materials. With this, a new problem arises, which resides on the complex geometric shapes that may result from the topological optimization process through computational calculation, which can often lead to highly complex geometries, and consequently enhanced difficulties to manufacture with controlled costs, or even turning it to be impossible to manufacture (Søndergaard & Per Dombernowsky, 2011).

Digital manufacturing is the production of physical objects using virtual models and aims to create a digital continuity / interoperability between the design and execution of the object. Digital manufacturing processes

can include additive and subtractive manufacturing. Briefly, in the first technique, the additive process corresponds to the addition of material, by successive overlapping of multiple layers, forming a 3D model / prototype (Figure 3). This process is the most interesting, as it does not incur on considerable waste of material, inherent to the subtractive process, which increases the ecological footprint. Additive manufacturing is a manufacturing process that promises to overcome most of the obstacles associated with traditional manufacturing / construction methods, allowing optimization through computational methods, as well transposing an topological optimization with practically no constraints at the manufacturing level (Jipa et al., 2016).

| (a) | (b) |
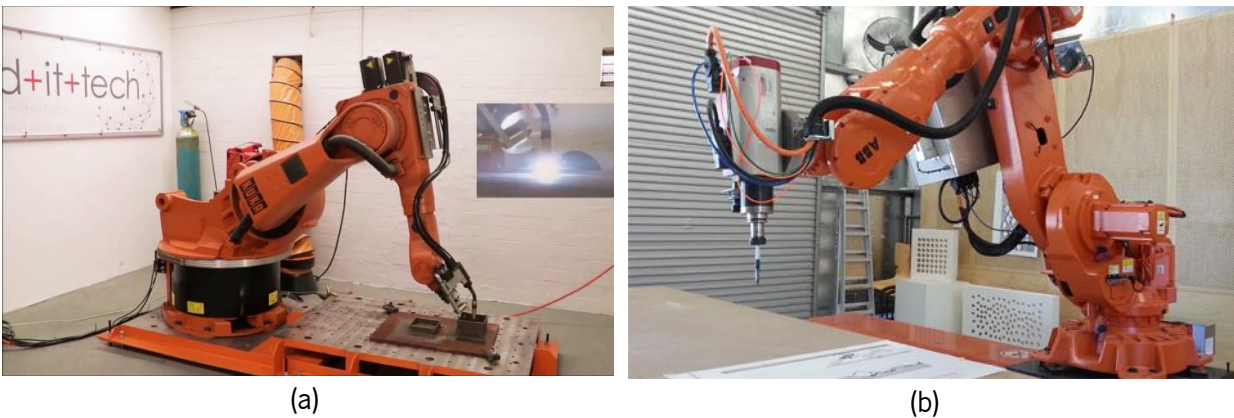
Figure 3 - (a) Additive manufacturing robotic (Add It Tech Pty Ltd | 3D Printing Services, n.d.) and (b) Subtractive manufacturing robotic arm (ABB Group. Leading digital technologies for industry — ABB Group, n.d.)

The industry of Architecture, Engineering and Construction (AEC) is still not that much involved in the digital manufacturing, due to multiple aspects that this sector has been facing during the last decades. From those aspects it can be highlighted: low efficiency of workers, increasing rate of onsite accidents, lack of skilled workers and inability of controlling the onsite construction efficiently (Barbosa et al., 2017; Hook et al., 2016). However, due to the abovementioned the construction sector can withdraw huge benefits from embracing digitalization. Therefore, the construction industry, namely large companies will necessarily have to start to invest more in the digital construction, not only in terms of the integrated approach of the design and production phases, but also in the improvement of efficiency of manufacturing / production processes. However, within the scope of research and innovation, very interesting digital construction processes are

already beginning to be seen, namely, novel constructive processes for producing elements within the scope of civil construction applications, aiming to cope with problems / drawbacks in the conventional constructions methods (Barbosa, 2017; Hook, 2016; Lim et al., 2012b). These digitization processes consist on 3D concrete printing (3DCP), which is mostly based on additive manufacturing (AM) techniques, specially developed / adapted to be used with concrete as material in the AEC industry. Those AM techniques consist mostly on "extrusion – based" and "powder – based" processes, which essentially consists on the "layer-by-layer" printing of a cementitious matrices. Among these, fiber – reinforced cementitious materials have huge application potential with AM techniques since the reinforcement is already comprised within the printed matrix (Smarsly et al., 2020).

The emergence and evolution of additive manufacturing processes unveils many advantages over conventional construction methods. Among those, it can be highlighted: i) the production of complex geometry architectural / structural elements (without using any extra tools or molds); ii) waste reduction; iii) safer construction processes; iv) decreasing construction's cost and time of complex geometrical shapes; v) relatively easiness to add multi-functionality and functionally graded properties to the layered elements (Buswell et al., 2007; Hopkinson et al., 2006; Lim et al., 2012b; Ngo et al., 2018). These advancements on robotized / automated production of elements from buildings / infrastructures allows the AEC sector to move towards industry 4.0, making it possible to materialize complex geometrical elements that can be modeled parametrically and throughout topology optimization processes.

In the following sections, the most up-to-date technologies in the field of 3DCP are overviewed, their potential, advantages and drawbacks are detailed and discussed. It will also be overviewed different strengthening techniques for 3DCP. Afterwards different methodologies and software for parametric modeling and topology optimization, current available, will be analyzed, in order to assess which one will be the most suitable software to be used in the scope of the present dissertation.

2.2 Current 3D concrete printing technologies

2.2.1 Introduction

As stated before, additive manufacturing, commonly known as 3D Printing, is defined as the addition of material, by successive overlapping of multiple layers, forming a 3D prototype / object, directly from a digital file that includes its geometry. It can be often referred as: additive fabrication, additive processes, additive techniques, additive layer manufacturing, freeform fabrication, accordingly to (ASTM F2792-10).

Among additive manufacturing processes, there are two main approaches, powder-based and wet-extrusion 3DCP, being the latter more widely disseminated. The powder-based approach is established on two main techniques, the one developed by (Pegna, 1997), which corresponds to the idea of a free-form construction using layer by layer selective deposition of Portland cement.

In this first technique the elements were made by placing a matrix material layer (sand), which was selectively covered by a reactive agent (cement) (Lowke et al., 2018). Later on appeared other powder-based technique, called by D-shape technology and was invented by the Italian engineer Enrico Dini. This approach essentially consists in injecting an adhesive binder into a powdered material, which is deposited layer upon layer. The adhesive binder serves to bind the powders together (Delgado Camacho et al., 2018).

On the other hand, the wet-extrusion approach corresponds to the extrusion of a cementitious material (in its fresh state) through a nozzle and depositing it layer-by-layer, forming a 3D model. This approach is the most commonly used in AM techniques of cement-based materials and has the advantage that the material can be extruded using a pump system already used in conventional construction (Delgado Camacho et al., 2018).

2.2.2 Contour crafting

The Contour Crafting (CC) method was developed by Prof. Khoshnevis at University of Southern California in the late nineties (B. Khoshnevis et al., 2001; Behrokh Khoshnevis & Dutton, 1998). CC technique is an additive manufacturing (AM) technology that uses computer control to exploit the superior surface-forming

capability of troweling in order to create smooth and accurate planar and free-form surfaces out of extruded materials (Behrokh Khoshnevis & Dutton, 1998). CC is a hybrid method constituted by a layer manufacturing process (extrusion-based) for forming the object, and by a filling process through pouring or injection, that build the object core (B. Khoshnevis et al., 2001; Behrokh Khoshnevis & Dutton, 1998). In relation to current layered fabrication processes (AM techniques), this method has some important advantages, such as: better surface quality, higher fabrication speed and the ability to use a diverse range of materials such as plaster, cement, clay, and concrete (B. Khoshnevis et al., 2001; Behrokh Khoshnevis, 2004; Behrokh Khoshnevis & Dutton, 1998).

Other key advantage of CC is the possibility of integration with other robotics methods for installing internal components such as pipes, electrical conductors, and reinforcement modules to enhance mechanical property (Behrokh Khoshnevis & Dutton, 1998; Kwon, 2002).

Since the ancient times, artists and craftsmen have effectively used simple tools such as trowels, blades, sculpturing knives, and putty knives for forming materials in paste (Behrokh Khoshnevis et al., 2005). However, even with the advance of mechanized processes, based on computer numerical control and robotics, this primary step of using these simple but powerful tools continues to be done manually.

In CC approach, this step comes into consideration, by using computer control to take advantage of the superior surface forming capability of troweling to create smooth and accurate, planar, and free-form surfaces (Behrokh Khoshnevis et al., 2005). This method uses two trowels (see Figure 4) that are attached to the extrusion nozzle, thus allowing a superior quality finishing. In this approach only the outer surface of the object, that serves as a formwork (as well as a few internal hatches) are made by extrusion.

The hollows are filled with a cement-based mortar / concrete, thus allowing high-speed manufacturing (Behrokh Khoshnevis, Yao, et al., 2006). Figure 5 shows a schematic example of a possible application of the the CC technique in an *in-situ* construction operation.

(a)   (b)

Figure 4 - The nozzle system of Contour Crafting technology with the side trowels. (a) Nozzle assembly and rotation mechanism and (b) Contour Crafting nozzle constructing a hollow wall (J. Zhang & Khoshnevis, 2013).
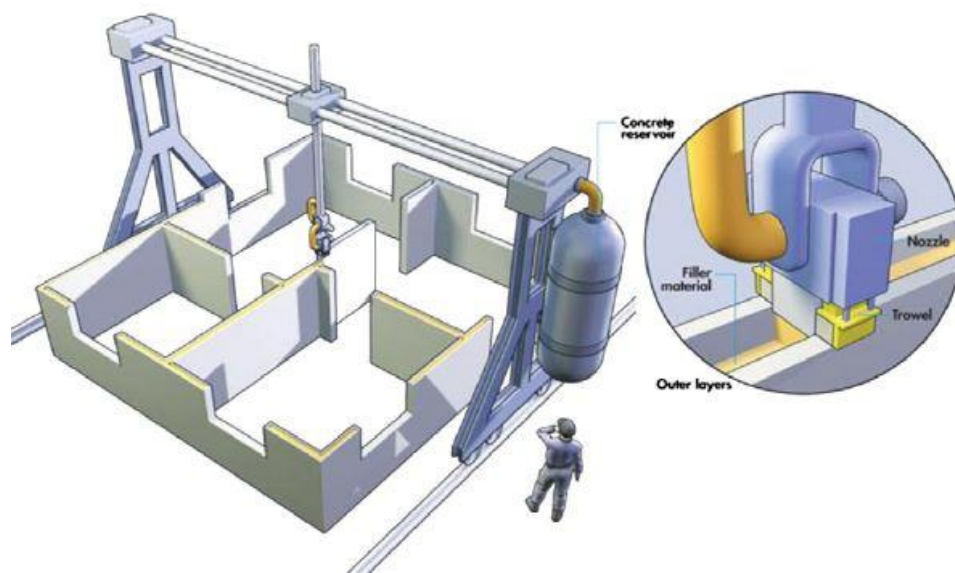
Figure 5 - Contour Crafting in construction operation (J. Zhang & Khoshnevis, 2013).

The CC method, has some certain limitations (B. Khoshnevis et al., 2001; Behrokh Khoshnevis & Dutton, 1998). One of them is due to the use of the side trowel, since very small hollow volume, such as small holes, cannot be made, because they cannot accommodate the side trowel. In addition, probably, it is not possible no create features that are relatively thin (e.g. vertical blade) by using the side trowel. Other limitations regarding this method are related to the size of the extrusion nozzle's orifice and with the control of the viscosity of the extrude material. Figure 6 shows some features created using the Contour Crafting technology.

(a)   (b)
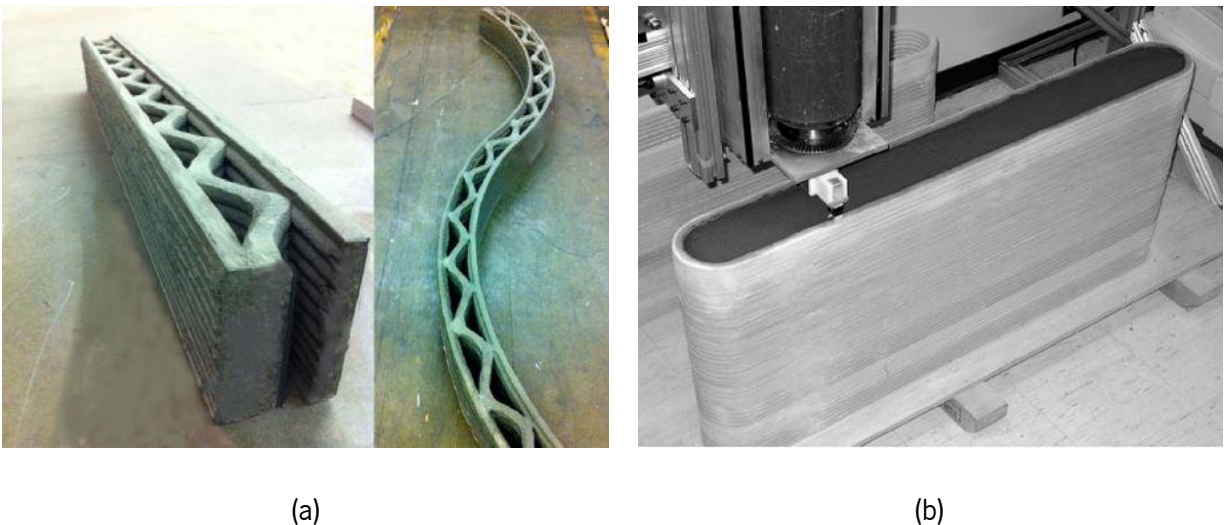
Figure 6 - Objects created using CC technology. (a) Wall section and (b) Top view of a concrete wall (Behrokh Khoshnevis, Hwang, et al., 2006; X. Zhang et al., 2018).

2.2.3 Wet-extrusion technology(s)

Wet-extrusion technology is basically similar to the CC approach, it is a construction method that has the capability of fabricating a predesigned building element in 2D layers on top of each other, the repetition of which completes a 3D model.

The main printing methods based on wet-extrusion technology were developed by the Loughborough University, Eindhoven University of Technology, by Gosselin et al., and using mobile robots.

Wet-extrusion technology (by Loughborough University) was developed at the Loughborough University in the United Kingdom (Lim et al., 2009). Similar to the most rapid manufacturing processes, this

method starts with data preparation. The object that is desired to be printed, is designed as a 3D CAD model, and then converted to an STL file format, which is then subsequently sliced with desired layer depth. A printing path for each layer is generated and a G-code file (based on low level language for machines) for printing is created (Lim; et al., 2011). The main difference to the conventional AM methods is the additional post-processing step that optimizes the generated printing path of the deposition head, thus reducing the printing time as well possible material overprint, due to the turn on/off operation of nozzle, by minimizing the non-printing movements of the deposition head (Lim; et al., 2011).

The concrete printing (CP) machine at the Loughborough University consists of a 5.4 m in length by 4.4 m in width by 5.4 m in height frame, along X, Y and Z axis, respectively (see Figure 7). The printing head is located on a mobile horizontal beam. The beam moves in the Y and Z directions, while the printing head moves exclusively along the X axis. The concrete mixture is placed on a hopper on the top of the printing head and then extruded as a pre-defined filament shape. The current flow rate for printing is set to less than 1.4 kg/min in order to support the small nozzle diameter of 9 mm (Lim; et al., 2011). The nozzle is rounded shaped, thus facilitating the control of the machine movement.

(a)   (b)

Figure 7 - Concrete Printing technology by Loughborough University. (a) Structural frame and (b) Movable horizontal beam with the printing head (Lim; et al., 2011; Lim et al., 2012a).

Like other (AM) techniques, this method has some limitations. The size of the printed object is constrained by the geometry of the CP frame (Lim et al., 2009). The existence of cross beams over the frame in order

the maximize the stiffness, limits the maximum height of the printed object. In addition, the movable beam and the printing head brings limitations to the actual area of the printed parts.

Wet-extrusion technology (by Eindhoven University of Technology) is a technique based on the CC approach, and was been developed at the Eindhoven University of Technology (TU/e) (Bos et al., 2016). The printing system has a 4-degree-of-freedom (DOF) gantry robot serving a print area of 9 x 4.5x 2.8 m³ (see Figure 8a). Concrete is mixed with water and pumped into a hose, by a mixer-pump located on the side of the set-up. The hose is connected to the printer head (see Figure 8b) situated at the end of the vertical arm, which is able to perform linear displacements along X, Y and Z direction and allow a rotation around Z axis (Bos et al., 2016).

(a)   (b)
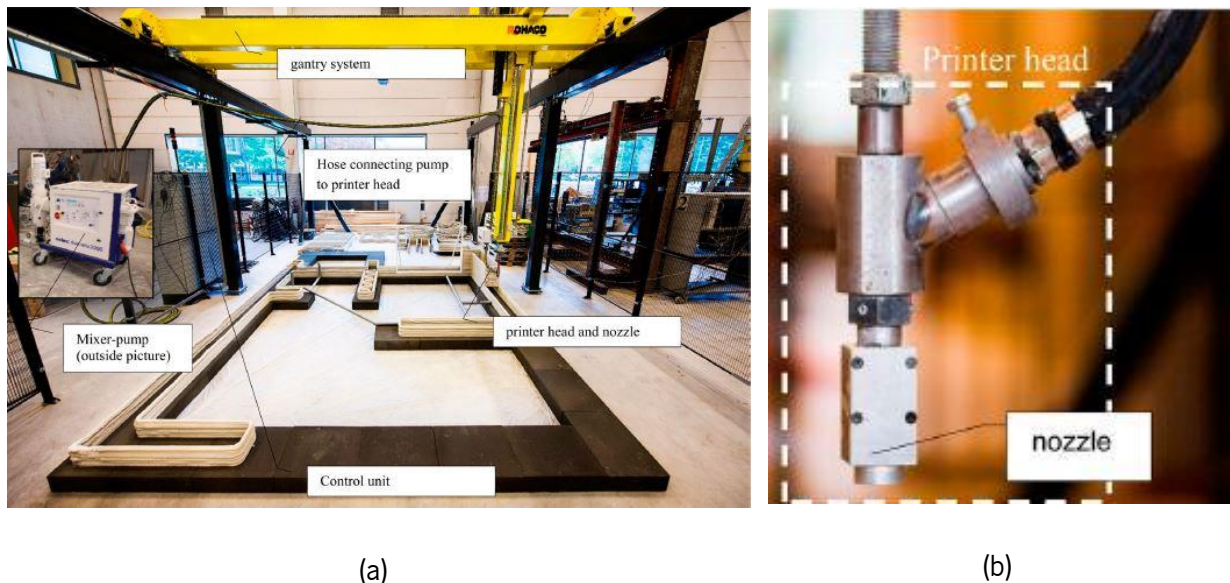
Figure 8 - Wet-extrusion technology by Eindhoven University of Technology. (a) 3DCP facility at the TU Eindhoven and (b) Printer head and nozzle (Bos et al., 2016).

As many other 3DCP technology one of the limitations of this approach, it is associated with the height of the print head above the print surface, which has considerable influence on the geometry and properties of the printed object (Bos et al., 2016).

Wet-extrusion technology (by Gosselin et al.) is a large-scale AM technology, developed by Gosselin et al. (2016). This technology is based on a FDM-like technique (Fused Deposition Modeling), where the material is deposited layer–by- layer through the printing head, and has the capability of creating ultra-high performance concrete (UHPC). The high mechanical performance of the material combined with the relatively small diameter of the extrude (4-6 mm) (Gosselin et al., 2016). This technology uses a different way of building path optimization called as tangential continuity method (TCM), (see Figure 9). The developers claim that this technique is more suitable of large-scale AM since the building paths are actually 3-dimensional, i.e. made of non-planar layers with locally varying thickness, thus allowing better exploiting of the geometrical potentialities of 3D printing technologies (Gosselin et al., 2016). One obvious advantage of this approach is the continuity between the different layers, thus avoiding the geometrical gaps between two layers which often limit the possibilities of AM processes, most notably FDM and powder-based processes.
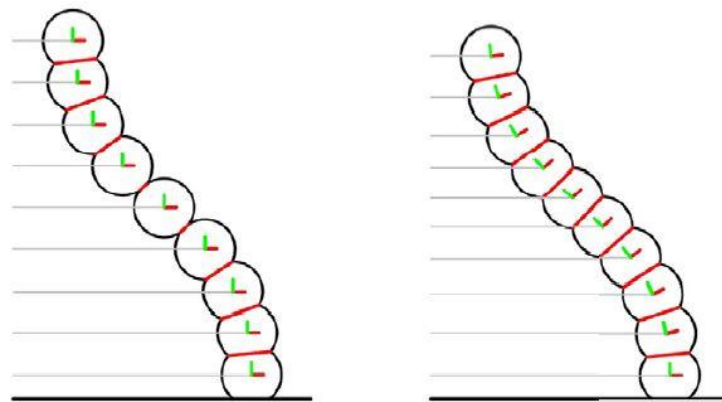
Figure 9 - Schematic cut perpendicular to layers 3D printed using the cantilever method commonly found in commercial 2D slicing software (l) and TCM method (right) (Gosselin et al., 2016).

The machine used in this technique was developed in-house with exception of the robotic arm which is an industrial ABB 6620 6-axis, used for spatial displacement (Gosselin et al., 2016). The remaining hardware parts consist in a print-head mounted on the robot as well as two peristaltic pumps, one for the premix and one for the accelerating agent, and a premix mixer, all three parts deported from the robotic arm. Figure 10 shows a schematic sketch of the 3D printing setup.
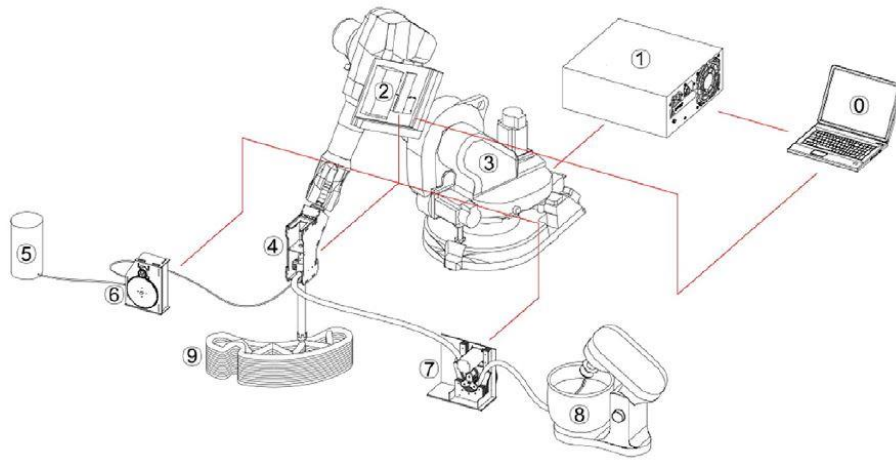
Figure 10 - Schematic of the 3D printing setup: 0. System command; 1. Robot Controller; 2. Printing Controller; 3. Robotic Arm; 4. Printhead; 5. Accelerating agent; 6. Peristaltic pump for accelerating agent; 7. Peristaltic pump for premix; 8. Premix mixer; 9. 3

Wet-extrusion technology (using mobile robots) has been proposed by X.Zhang et al. (2018), This system allows the users to add as many robots as needed in a shared environment in order to print a large structure, simultaneously. The robots are capable of localization, collision avoidance and efficient coordinated printing through optimal robot placement (X. Zhang et al., 2018).

One of the main limitations of the current printing systems available is their lack of scalability. Majority of the current approaches of 3D printing are based on a gantry system that requires a massive external framework in order to support the single printing head, thus limiting the size of the printed object. This methodology claims to solve those problems because stands on the idea of using multiples mobile robotic printers, that offers greater practical scalability and more time efficiency compared to others 3D printing technologies (X. Zhang et al., 2018). Each mobile robot printer consists of a holonomic mobile platform, a 6-axis robotic arm, a stereo camera and a pump (see Figure 11a). Figure 11b shows the printing of a large structure made using this collaborative printing methodology.

(a)   (b)
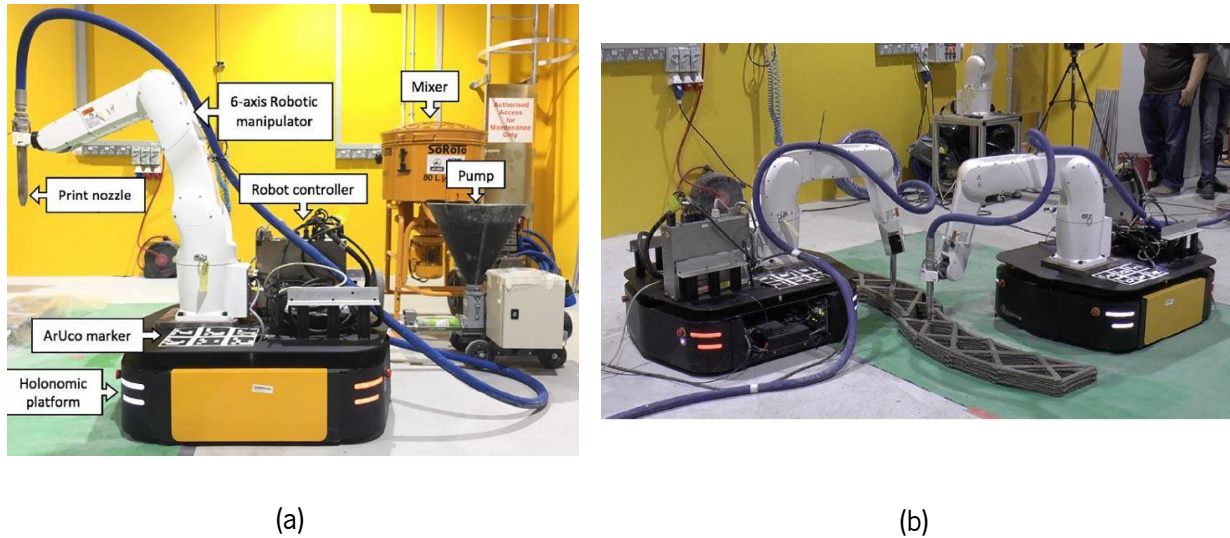
Figure 11 - Wet-extrusion technology using mobile robots. (a) System setup for one robot printer and (b) Concurrent printing of a large, single-piece, concrete structure by two mobile robot printers (X. Zhang et al., 2018).

2.2.4 CONPrint3D

Most of the extrusion-based additive concrete manufacturing approaches, are not suitable for large-scale, on-site mass construction. The main reason is their focus on high spatial resolution, the use of fine filaments, and the concentration on in-plant rather than on-site-fabrication (Mechtcherine et al., 2019). The use of fine filaments brings advantages, such as: high resolution on the construction process, allowing fabrication of highly detailed structures; lightweight printheads, which can be of very simple design as well. In order to provide the necessary control of material flow and geometrical precision, the use of a circular vertically oriented nozzle is often sufficient. However, fine filaments also mean both low production rates and the need for very fine-grained mortars, which do not comply with the existing concrete codes (Mechtcherine et al., 2019). The use of large-size filaments brings some advantages, such as: high productivity construction processes; use of concrete with coarse aggregates in accordance with valid national and international norms (Mechtcherine et al., 2019). Nowadays, rectangular-shaped extruders with larger dimensions, besides the productivity advantages bring also benefits regarding the overall mechanical behavior of a printed element due to a better layer interfacial bond behavior as consequence of the higher interface area between two adjacent layers (Zahabizadeh et al. 2019; Zahabizadeh et al. 2020).

The methodology in applying 3D-printing in the field of on-site concrete construction is being investigated since 2014, at the TU Dresden, in the scope of the research initiative ZukunftBau (Future Construction) of the German Federal Institute for Research on Building, Urban Affairs and Spatial Development (BBSR)'s (Nerella et al., 2016). The main reason of this project is to develop a formwork-free monolithic construction process using 3D-printing, called by CONPrint3D. Figure 12 depicts schematically the main components of CONPrint3D.
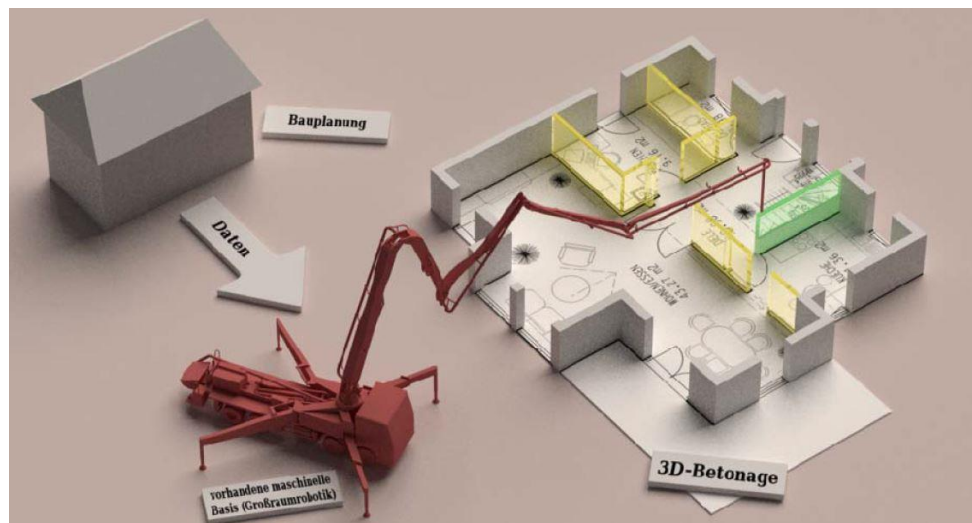
Figure 12 - Illustration of CONPrint3D approach (Nerella et al., 2016).

The main aspects of this technology are to develop a timely, labor and resource efficient advanced construction process, as well as make the process economically viable while achieving broader acceptance from the existing industry practitioners (Nerella et al., 2016). In order to achieve those objectives, this technology uses, as much as possible, existing construction and production techniques, adapting only new process to construction on-site constraints. One vital aspect of the project strategy is using, as a mechanical platform a modified truck-mounted concrete pump and a custom-developed print head attached to the boom, this ensures the continuous extrusion of the concrete and the geometrical precision on the construction site (Krause et al., 2018; Nerella et al., 2016). The methodology of the control process is a BIM-based planning, basically the geometric and material data, as well the geometrical precision data are extracted from the 3D building model, then processed and transferred to the modified concrete pump, allowing direct implementation of a previously created concreting plan in the machine control for automated movement

(Krause et al., 2018). As stated before, this technology uses an extrusion-based process, so the fresh concrete that comes from the print head is laid out layer by layer with lateral shaping elements (see Figure 13)

(a)   (b)
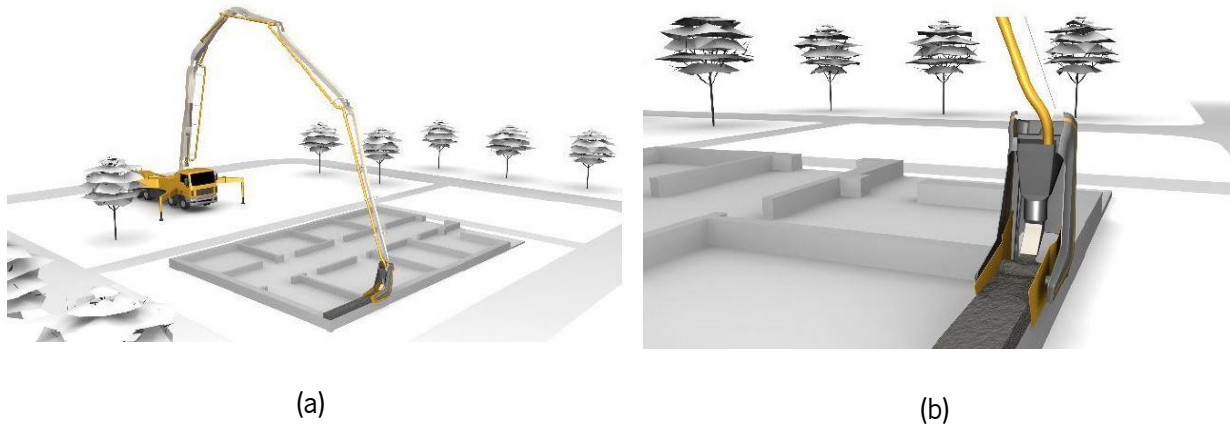
Figure 13 - CONPrint3D approach. (a) Geometrically precise installation of the concrete by modified truck-mounted concrete pump and (b) Extrusion-based installation of fresh concrete using a newly developed print head (Krause et al., 2018).

2.2.5 Powder-Based 3DCP technology

The powder-based technology, as stated before essentially consists in injecting an adhesive binder (e.g. magnesium oxide and magnesium chloride) into a powdered material. The best-known system using the powder-based approach is the D-shape technology, which is a three-dimensional printing system for producing conglomerate building or building blocks (Cesaretti et al., 2014). Unlike the methods that use the cement-like paste in the fresh state (i.e. wet-extrusion technologies), this system uses powder-based materials. This technology can be used according to two different methods invented and patented by the Italian Enrico Dini (Cesaretti et al., 2014). In the first printing method the entire building structure is produced directly on site, while the second methods correspond to the assembly of a set of building blocks, fabricated "off-site" – or in the construction site. This last approach often requires additional reinforcements.

The D-shape method uses a machine with a width of 6 m that comprises several massive plotters and a print head comprising up to 300 nozzles at 20 mm inter-axis distance in order to produce large objects (Lowke et al., 2018). This print head travels along two directions in the *X-Y* plane and hardens the powder using a

certain binder. The binder is deposited exclusively on places where the building material should become solid and the remaining is kept loose and removed at a later stage (Cesaretti et al., 2014; Sanjayan & Nematollahi, 2018). A set of four stepper motors move the frame on the *Z* axis. Figure 14 shows the complete system of the D-shape 3D Printer used with this technique (Cesaretti et al., 2014).

(a)	(b)

Figure 14 - D-shape technology. (a) Complete printing system and (b) detail of the printing head comprising over 300 nozzles (Cesaretti et al., 2014).

The core of the system is the "printing head", which acts also as a solid material spreader at the beginning of the printing process (see figure 14). The gantry holding the printing head is internally void and is cyclically filled with the granular material, which is then deposited for the next "layer". The "sand" is deposited in a thin layer by a shaving blade during the beam movement along its main *X* axis. A set of rolling cylinders provide an homogeneous sand pressure and smoothens it prior to the printing start on the newly deposited layer (Cesaretti et al., 2014). After finishing the production process, the residual sand is removed, and the object is infiltrated by an additional binder. Afterwards, the object is sanded and polished. The process has been used to create 1.6 m height architectural pieces called "Radiolaria" (Sanjayan & Nematollahi, 2018). Figure 15 shows some created objects with very complex geometrical shapes using D-shape technology.

The disadvantage of the D-shape is that requires more maintenance, cleaning and control, and the final structure must be cleaned from the remaining dust to form the post-treatment shape. Part of the post-processing process involves removing the unused dust and grinding and polishing the surface (Sahin & Tosun, 2019). The deposited sand that is not "activated" through the binder, which also serves as support material, may also contribute to the decrease of the sustainability footprint if not properly reused.

(a)   (b)

Figure 15 - Created objects using D-shape 3DCP technology. (a) Underwater Mona and (b) Radiolaria Pavilion for the city hall of Pontedera (Portfolio | D-shape).

2.3 3D printable materials

One of the advantages of using the 3D Concrete Printing (3DCP) technology is the possibility of creating / producing structural components without using any kind of formwork. Thus traditional concrete cannot be directly used, instead a "printable" material is required. Because the manufacture process requires a continuous, high degree of control of the material during the printing, high performance building materials

are preferred. For that purpose, the rheological properties of the cementitious materials are critical to the success of manufacture (Lim; et al., 2011; Lim et al., 2012).

In order to obtain a proper printable material, with good workability or to be more precise with good "printability", it must have the following key attributes (Soltan & Li, 2018): (1) extrudability, the capacity of the cementitious material in the fresh state to pass throughout the nozzle as a continuous filament, and be able to lay down accurately, and stay in the position correctly; (2) buildability, which is defined as the ability of the printed filament to hold its shape, for that the printed materials must have initial low viscosity, and increase immediately to ensure strength to stand under the weight of subsequently printed layers, from other words buildability can be based by the number of layers that could be built up, without the bottom layers exhibiting significant deformation; and (3) interlayer adhesion, the ability of the filaments to form a cohesive bond, generating a unified and structurally sound printed part with the capacity of maintain a "uniformly heterogenous" structure while being deposited. Moreover, another important characteristic is related to the material's open time, i.e. for how long the material can be printable without affecting the printing quality.

(Austin et al., 1999, 2002, 2005; Le et al., 2012a), showed that the dosage of superplasticizer, retarder and accelerator have significant effect on the workability. These results demonstrated the importance of superplasticizer for achieving the proper workability and high strength with a low water to binder ratio.

The same studies also concluded that increasing the dosage of the retarder and accelerator cause a decreasing of workability (i.e. increasing the shear strength). It should be stated that the accelerator is added at the nozzle, just before the extrusion process, in order to be able to control the setting time during the printing process.

Regarding the extrudability key attribute, (Malaeb et al., 2015) evaluated it based over the distance that the paste can be printed continuously without any separation or cracks. The studies made by (Chen et al., 2019; Le et al., 2012a) concluded that the combination of particle size distribution of the components, binder to aggregate ratio, amount of superplasticizer and fibers have a considerable effect on the extrudability of a printable material (see Figure 16).

<div align="center">(a)   (b)</div>
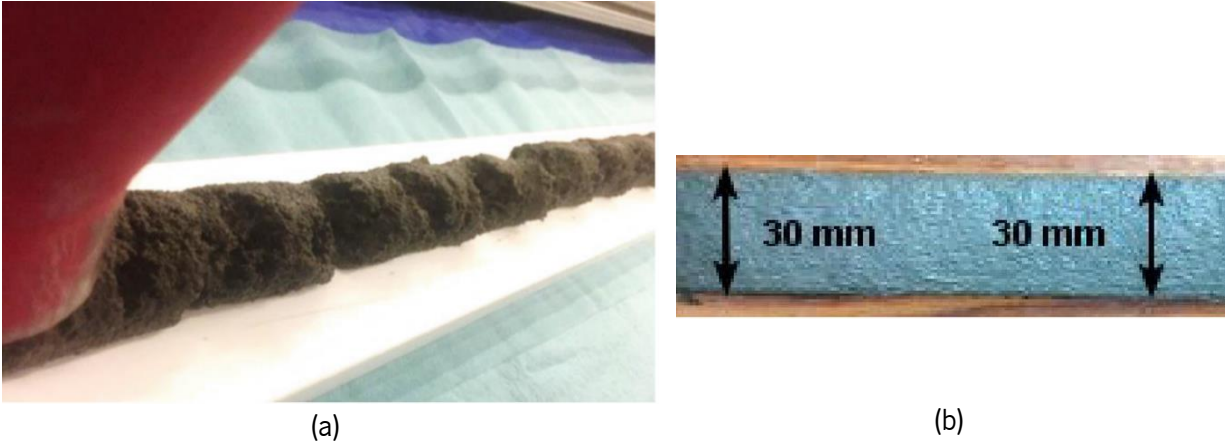
Figure 16 – Two examples of testing printability of material. (a) Low-quality and (b) high quality printed layers (Kazemian et al., 2019; Rahul et al., 2019).

In order to the deposited layers exhibit practically zero deformation, either low to zero slump concrete is required (see Figure 17). (Malaeb et al., 2015) concluded that increasing the amount of superplasticizer caused a reduction in the maximum number of printed layers, which can support the weight of upper layers and even themselves (i.e. reduction of buildability). Studies made by (Kazemian et al., 2019; Panda et al., 2019; X. Zhang et al., 2018), verified that the use of silica fume and highly purified Nano-attapulgite clay (NC) contributes positively to the shape stability of fresh mixture. On other hand, they concluded that adding polypropylene fibers didn't help increasing the stability. (Panda 2019) also reported that the yield stress could be improved without affecting the viscosity of the materials, by adding NC in the cementitious mixtures. Figure 18 shows two examples made by (Panda et al., 2019). It's possible to see that the mortar with NC on his composition have a better buildability (Figure 18a), something not reported by the normal cementitious mortar (Figure 18b), which started deforming after the extrusion of the 10th layer
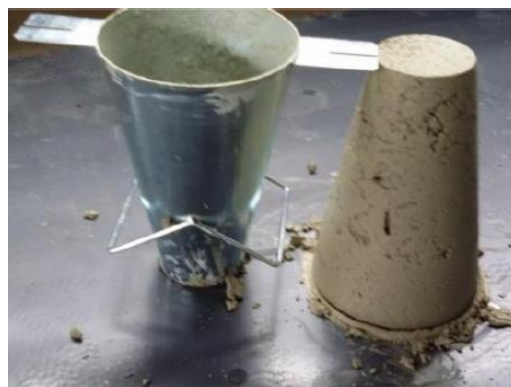
<div align="center">Figure 17 - No Slump 3D printable concrete (Paul et al., 2017)</div>

(a)	(b)

Figure 18 – Buildability evaluation. (a) normal cementitious mortar and (b) mortar with NC on his composition (Panda et al., 2019).

Extrudability and buildability are competing factors, since that a high workability is related with a good extrudability while a low workability promotes buildability. Furthermore, too much buildability can have a negative impact at the interlayer adhesion and high workability (high extrudability) can promote segregation of constituents. With that said, it is possible to conclude that these "key attributes", mentioned before, must be properly balanced to allow printability.

2.3.1 Material Composition

An appropriate balance of all the constituents must be achieved to ensure both proper rheological and mechanical properties of a printable cementitious mixture. For that reason, most of the researchers had to perform several experiments in order to determinate the right composition of the optimal mix. Table 1 presents some examples of material compositions for 3DCP available in literature. The most common constituents used in the mixes were sand (as fine aggregate) and cement. The majority of the authors did not resort to the use of coarse aggregates (maximum size of the aggregates was 2 mm), as the diameter of the nozzles are relatively small (Anell, 2015; Le et al., 2012b; Malaeb et al., 2015; Perrot et al., 2016). To be possible to have more control of the workability of the printed material (open time and setting period), superplasticizer (for example Viscocrete), accelerator and retarder were also used in the mixes (retarder to enhance the "open time", facilitating a constant flow during the printing process and the accelerator to

control the setting time of the printed part). Usually the retarder is either injected directly in the printing head in an automated fashion, or sprayed manually between printing of consecutive layers. Furthermore, in order to reduce shrinkage and deformation, polymeric polypropylene micro fibers were also used in some of the mixes, by e.g. (Anell, 2015; Le et al., 2012b).

Table 1 - Materials compositions of 3D printable concrete (Paul et al., 2017).

Materials compositions (kg/m³)							
Authors	cement	Fly-ash	Silica fume	sand	water	SP	Fiber
(Nerella et al., 2016)	430	170	180	1240	180	10	-
(Le et al., 2012a)	579	165	83	1241	232	16.5	1.2 (PP)
(Anell, 2015)	659	87	83	1140	228	11.6	1.2 (PP)
(Perrot et al., 2016)	Binder content expressed as a weight:						
	cement 50%, limestone filler 25%, Kaolin 25%, w/c = 0.41; SP/cement = 0.3%						
(Malaeb et al., 2015)	cement 125g, sand 80g, filler 160g, water/cement = 0.39; SP = 0.5-1 mL						

Notes: SP: superplasticizer; PP: polypropylene (12/0.18 mm length/diameter)

2.3.2 Mechanical properties of 3D printable materials

Despite the many advantages that AM approaches brings to the AEC sector, there are some disadvantages. One of the main drawbacks is related to the structural behavior of the printed specimens, as they have distinct properties in different directions, i.e. anisotropic or orthotropic behavior, something not applied to casted specimens, which is assumed (for the most times) to have an isotropic behavior. Also, the printing parameters such as, flow behavior of fresh materials, printing speed, printing time gap between the subsequent layers, etc. have significant influence on the final 3D printed parts strength (Paul et al., 2018). In case of a composite with fiber reinforcement, strength is also influenced by the fiber orientation.

Moreover, since in matrices reinforced with fibers there is not fiber bridging between two adjacent layers, printed FRC potentiate the appearance of cold-joints at layers interface. In the majority of the 3DCP approaches, since the printing process is done by the deposition "layer upon layer" of different filaments, is expected that the material mechanical properties have better behavior in the horizontal direction, i.e. in-plane printing direction, than in the vertical direction (Le et al., 2012b). Subsequently, it will be presented the some

mechanical properties of 3D printable materials available in literature, more specifically compressive, flexural, uniaxial tensile and interlayer bond strength behavior.

Regarding compressive strength, a study made by (Le et al., 2012a) concluded that using 1 to 2% of superplasticizer (SP) in printed specimens increased the compressive strength, compared to the samples with only 0.5% of SP, however the SP caused a delay in the hardening process of concrete at early ages. (Nerella, 2016; Sanjayan 2018) observed on their studies an 10% to 14% increase on the compressive strength of printed specimens loaded perpendicular and parallel to the layer's orientation (see Figure 19), respectively, when compared with mould cast specimens.

Contrary to those findings, (Le et al., 2012a) reported that in their study the values of compressive strength were higher on the mould cast specimens, which is the most common case for the compressive strength results of 3DCP specimens available in literature.
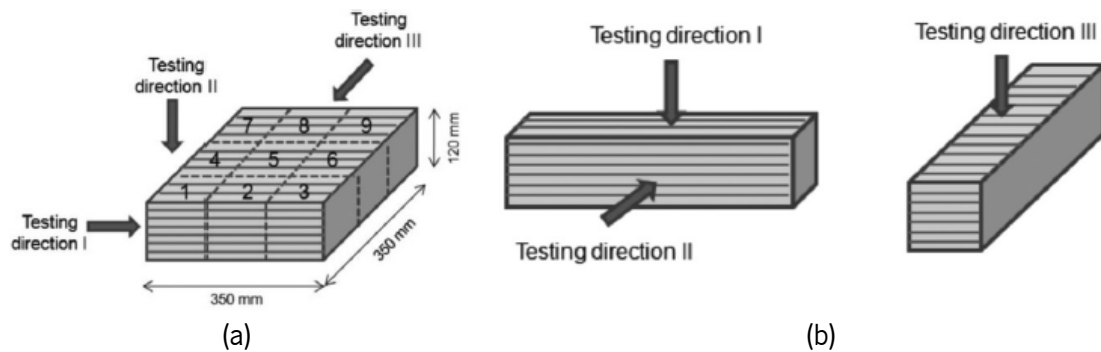
Figure 19 – Collection of 3DCP specimens for (a) compressive testing and (b) flexural testing (Le et al., 2012b)

In addition, (Le et al., 2012a) also reported that the average compressive strength, on the optimum mixture with a water to binder ratio of 0.26 and a Portland cement content of nearby 600 kg/m^3, was measured between 91 e 102 MPa depending on the load direction relative to the orientation of the printed layers.

Table 2 shows the values of compressive strength obtained in the studies mentioned before (Le et al., 2012a; Nerella, 2016).

Table 2 – Comparison of compressive strength of cast and printed objects (Paul et al., 2017)

Authors	Specimens retrieved from	Type of test	Testing direction	Printed specimens			Cast specimens	
				3 days	21 days	28 days	21 days	28 days
Nerella et al. (2016)	1000 x 300 x 35-mm wall	Compressive strength (MPa) (size: 35-mm cube)	I	45.9	83.5	–	73.4	–
			II	49.7	80.6			
Le et al. (2012b)	350 x 350 x 120-mm slab	Compressive strength (MPa) (size: 100-mm cube)	I	–	–	96	–	107
			II			93		
			III			93		
	500 x 350 x 120-mm slab		I	–	–	102		
			II			102		
			III			91		

Furthermore, (Sanjayan 2018; Van Der Putten et al., 2019), concluded that the increase of time gap between the printed layers, decreased the compressive strength. (Van Der Putten et al., 2019) also reported that the increase of printing speed also decreased the compressive strength.

Regarding flexural strength, (Le et al., 2012a) measured it by performing a four-point bending test on both mould cast and printed specimens for different loading directions. It was reported that the flexural strength in the loading direction I and II were higher than the strength of vibrated mould cast specimens.

On the other hand, along the direction III the flexural strength was significantly lower (see Figure 19 and Table 3). The main reason for that is due to the anisotropy associated with the printing process, since in the direction III the load is applied along the plane of the interface between filaments (see Figure 19b), which demonstrates the influence of the inter-layer adhesion strength on the overall materials properties.

A study done by (Nerella et al., 2016), in high-performance mortar showed around 16% and 14% increase on the flexural strength of printed specimens loaded perpendicular and parallel to the layers orientation, respectively, when compared with mould cast specimens (see Table 3).

Some studies regarding the influence of the time gap between printed layers have been done. (Sanjayan et al., 2018) concluded that the flexural strength increased with time gaps between 10 to 20 minutes, and decreased with time gaps around 30 minutes.

Table 3 - Comparison of flexural strength of cast and printed objects (Paul et al., 2017)

| Authors | Specimens retrieved from | Type of teste | Testing direction | Testing time | | | | |
| | | | | Printed specimens | | | Cast specimens | |
				3 days	21 days	28 days	21 days	28 days
Nerella et al. (2016)	1000 x 300 x 35-mm wall	Flexural strength (MPa) (size: 160 x 35 x 35 mm)	I	4.8	5.8		5.1	
			III	4.3	5.9			
Le et al. (2012b)	500 x 350 x 120-mm slab	Flexural strength (MPa) (size: 220 x 63 x 50 mm)	I	–	–	16.5	–	11
			II			13		
			III			6.5		

Concerning uniaxial tensile strength, (Ogura et al., 2018a) assessed it by doing a uniaxial tensile test in mold cast and printed specimens (see Figure 20). From the test results, it was reported that the printed specimens exhibited strain-hardening behavior under uniaxial tensile loading for fiber concentrations as low as 1%.

For a fiber content of 1.5%, strain capacity was considerably higher, and very uniformly distributed, fine multiple cracks were observed. Beyond that, is was also concluded that the printed specimens exhibited superior strain-hardening behavior and more a pronounced multiple cracking stage in comparison to mold cast specimens (Ogura et al., 2018a).

It should be stated that after cutting the specimens, their ends were strengthened by casting a self-reinforced strain-hardening cementitious composite (SHCC) mixture prepared with polyethylene microfibers (HDPE).

(Yu & Leung, 2019) studied the importance of the fiber orientation on the ultimate tensile strength of printed SHCC mixtures. One of the conclusions of the study was that the strength appeared to be higher when fibers were preferentially aligned parallel to the loading directions, i.e. for the uniaxial tensile behavior. Contrary to that, the specimens with fibers aligned perpendicular to the loading direction showed to worst performance.
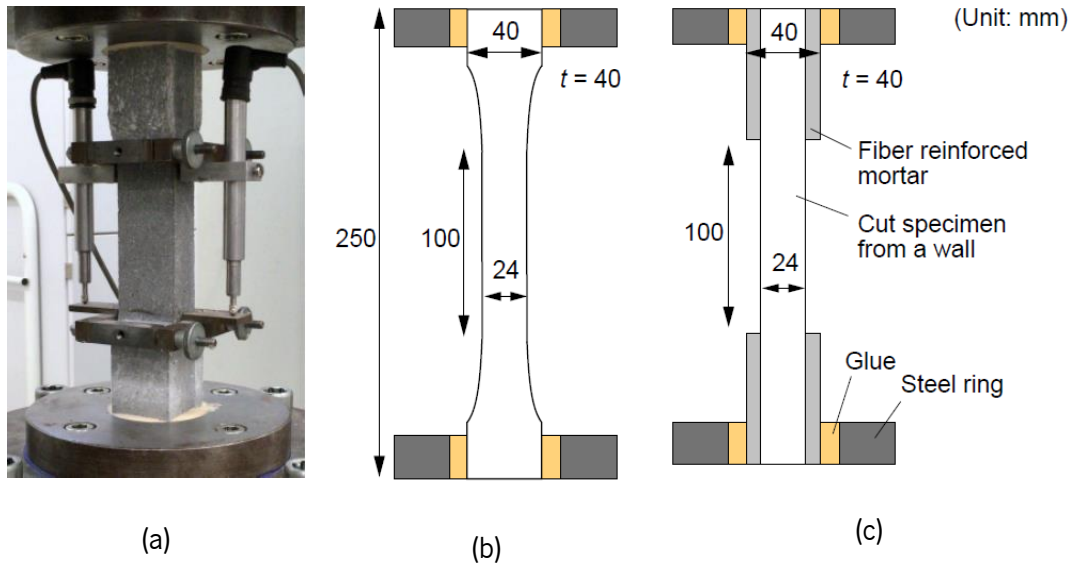
Figure 20 - (a) setup for uniaxial tension tests; (b) schematic view of uniaxial tension tests on mold cast specimen and (c) on printed specimen (Ogura et al., 2018a)

The interfacial behavior of 3D printed layers is considered a critical point of weakness in elements produced with this technique, due to either mechanical or chemical factors. Some tests have been done in order to evaluate the most important points of interlayer bond strength. (Le et al., 2012a) investigated the interlayer bond strength of a printed, high-performance, fiber-reinforced mortar using direct tension tests on cylindrical specimens, by varying the time gap between printing layers. The results shown in Figure 21, present a clear trend that the printing time gap has a significant influence on the bond strength, and that the same interlayer bond strength is reduced as the time-gap between printing consecutive layers is increased.
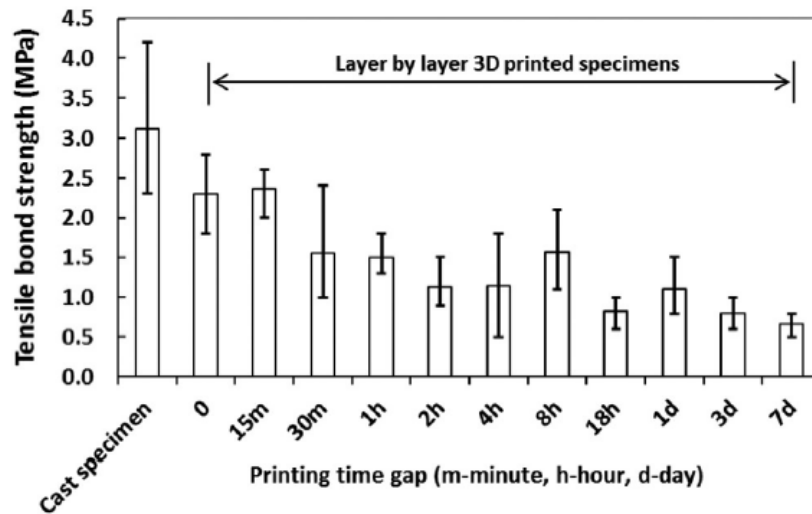
Figure 21 – Influence of printing time gap with tensile bond strength (Paul et al., 2017)

(Marchment & Sanjayan 2019) also assessed the interlayer bond strength for different time gaps. They reported that the interlayer strength of the specimens printed with 10 and 30 minutes time gaps were practically the same, but higher than that of the specimens printed with 20 minutes delay time (see Figure 22). The pattern observed in the latter study contrasts with the widely believed trend stated in the previous paragraph, which was reported by (Le et al., 2012a) and also observed by several researchers.
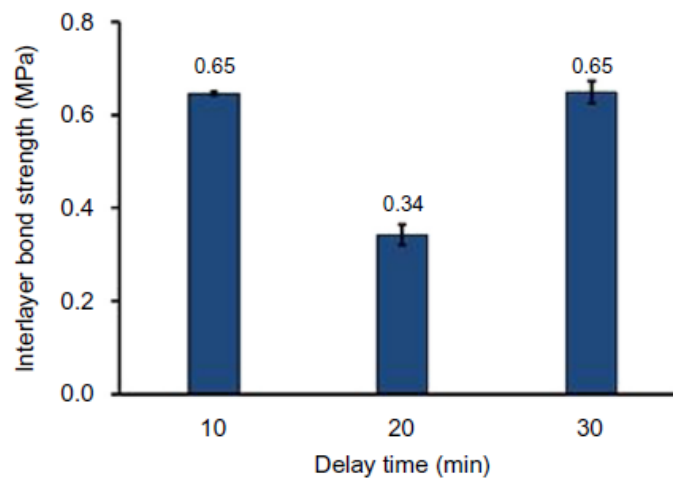
Figure 22 – Influence of printing time gap with tensile bond strength (Marchment & Sanjayan 2019).

In the same study (Marchment & Sanjayan 2019), also assessed the influence of using cement paste (Ordinary Portland cement - OPC) between printed layers on the bond strength of printed specimens through a uniaxial tensile test. The study has shown that the specimens using the cement paste between printed layers had higher bond strength (approximately an increase of 60%) than the conventional printed parts without interlayer paste (see Figure 23). They also concluded that pastes mixed with additives (paste 1, 2 and 3) such as retarder, viscosity modifying agent and slump retainer have shown a notably higher bond strength of approximately 120% to 180% higher than the samples in which was not employed paste in-between layers.
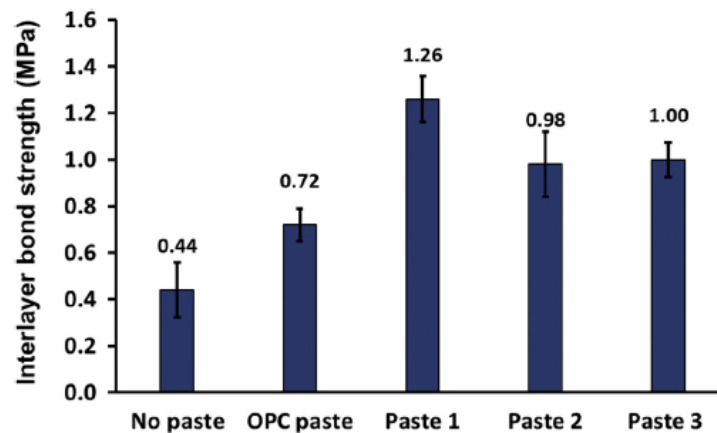
Figure 23 – Bond Strength test results of different types of mixture (Marchment & Sanjayan 2019).

A study made by (Zareiyan & Khoshnevis, 2017), where they assessed the influence of aggregate size, time gap and layer thickness with the interlayer bond strength, concluded that small sized aggregates and higher cement to aggregate ratios increased the compressive strength due to a better interlayer adhesion. In addition, they also noticed that the bond strength increased, and the compressive strength decreased with the increase of layers height and time gaps between layers.

2.4 Strengthening techniques for 3D concrete printing

2.4.1 Independent reinforcement methods for 3DCP

Independent reinforcement methods are regarded as methods that are not automatedly implemented along sided with the concrete printing process. A good example of an independent reinforcement method is the CC approach presented in the section 2.2.2, where first occurs the formation of a mold by using 3D printing technology, and then the filling process with concrete (Behrokh Khoshnevis, Yao, et al., 2006). In this approach, the reinforcement process happens among those previously mentioned where ties are put inside the printed formwork (see Figure 24a).

<div align="center">(a)   (b)</div>
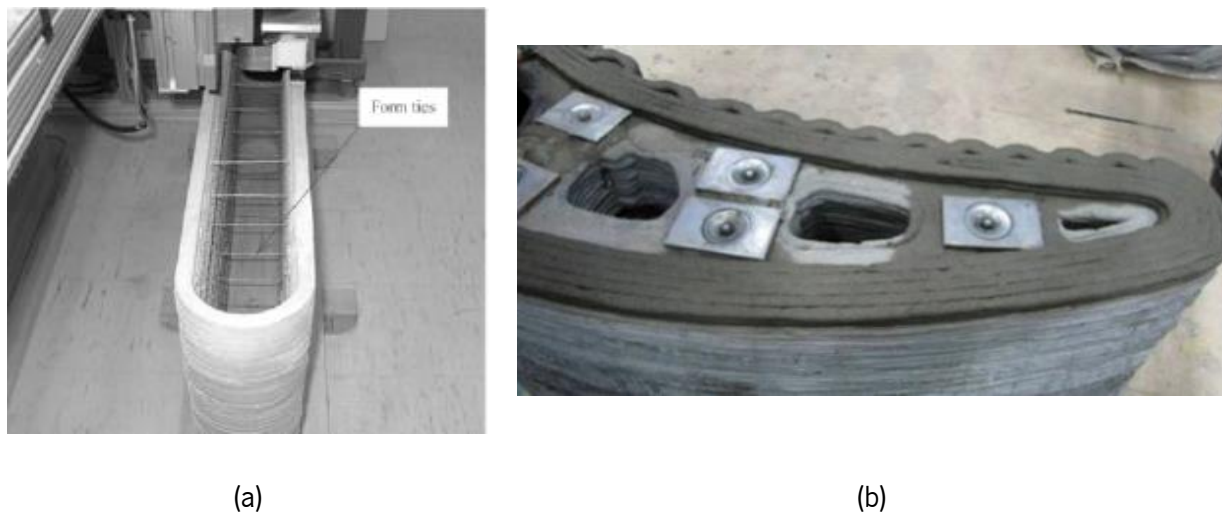
Figure 24 - Independent reinforcement techniques for 3DCP. (a) CC technology (Behrokh Khoshnevis et al., 2006) and (b) CP technology (Lim et al., 2012).

Other example that can be included in this category is the strategy used by Loughborough University, suitable for large components printed using AM (Lim et al., 2012). The printed elements were designed to form hollow conduits for the posterior placement of reinforcement (see Figure 24b). After printing, the post-tensioned rebars are inserted in the voids and then are filled with grouting materials. This reinforcement strategy is a good example of incorporating tensile capacity into large cement-based components showing the potential of AM techniques for produce large construction elements (Lim et al., 2012).

The Winsun company also uses a strategy similar to the reinforced method used in the CC approach. Basically, they first do the 3D printing process in order to do the formwork and then place the longitudinal rebars and stirrups in the desired position (see Figure 25a) (Lu et al., 2019). Finally, they cast the inner part with conventional vibrated concrete, in which the previously printed outer walls serve as mold. Other strategy could pass to invert those processes, like the one done by the Huashang Tengda company (2016), where they first placed the reinforcement rebars in the desired location and only then the material was printed around them (see Figure 25b) (Lu et al., 2019). For this purpose, a special designed forked-shape nozzle is required, in order to print both sides of the wall at the same time, while covering the existing reinforcement rebars.

<div align="center">(a)   (b)</div>

Figure 25 - Independent reinforcement techniques for 3DCP. (a) Method used by Winsun similar based on CC technology and (b) Method used by Huashang Tengda company (Mechtcherine et al., 2018).

2.4.2 Automated Reinforcement methods for 3DCP

The addition of steel fibers to concrete to replace conventional reinforcements bars or reduce it has been applied in concrete construction for several years. This process can be easily transposed for 3DCP as the reinforcement is added to the mixture during the mixing process and then the composite can be printed with the discrete reinforcement. It shows to be effective to some extent, as it increases post-cracking behavior, namely residual tensile strength, toughness as well decreasing the crack width and spacing. (Ogura et al.,

2018b) reported that the preferential alignment of fibers with the tensile loading direction in printed specimens lead to an enhancement of the ultimate tensile strain compared to mold cast specimens with a more random fiber orientation. However, it has some limitations regarding the length of the fibers, as they are short, they don't provide continuity, something important for robustness and ductility. Other limitation is associated with the reinforcement direction, which is directly related to the printing path, so the fibers can't be deposited vertically across the layers, something that would be very important to enhance layers strength and prevent cold joint between them (Mechtcherine et al., 2018). A way to solve the cold joints problem is to use a special 3D textile between the printed layers, a method proposed at University of TU Dresden (Mechtcherine et al., 2018).

Figure 26 - Alignment of fibers in the crack of specimen (after testing) (Readts, 2017).

Another method for automated reinforcement of cementitious printed materials is the one developed by (Bos et al., 2017). This methodology consists of a rotating spool feeding the reinforcement (metal cable / wire or chain) into the printing head where it is introduced in the concrete filament so that an integrated concrete-with-reinforcement filaments is extruded from the printing nozzle (see Figure 27). Pull-out tests done showed that the bond strength in printed concrete was considerably lower than in cast concrete.

Besides that, it was observed that the bond strength of steel cables is low compared to conventional ribbed bars, but somewhat higher than that of smooth bars (Bos et al., 2017). The four-point bending test showed

a good post-cracking behavior, however the failure of the specimen was controlled by the slippage of the cable, something that would not be expected based on the pull-out tests (Bos et al., 2017).

Furthermore, the bending tests confirmed the suitability of analytical methods to determinate the resistance of printed concrete with cable reinforcement, at least to obtain global estimate on the resistant moment capacity (Bos et al., 2017).

| (a) | (b) |

Figure 27 - Automated reinforcement with metal cable. (a) active reinforcement entrainment device (RED) for cable reinforcement of printed concrete and (b) Early version of RED, equipped with chain reinforcement (Bos et al., 2017).

To conclude, the use of this methodology has the advantage of decreasing the total time of manufacturing process due to the automated placement of the reinforcement during the extrusion process. Also, showed to be a feasible reinforcement method that has potential to achieve a similar performance to the one of conventional reinforced concrete.

2.5 Topology optimization algorithms

2.5.1 Introduction

The optimization of structural design is becoming more and more crucial due to the limited natural resources, environmental impact and technological competition among companies, being increasingly necessary the utilization of high-performance, low-cost and lightweight structures in the AEC industry. Recently, topological optimization gained a new interest with the advent of digitalized solutions such as digital fabrication of concrete, i.e. 3D printing.

The main objective of topology optimization aims to achieve the best material layout within a structure in order to maximize performance, for a given set of load cases and boundary conditions, while satisfying various constraints such as a given maximum amount of material. Succinctly, the process of optimization consists in:

- Defining the initial geometry of the structure;

- Defining the material and mesh properties;

- Defining the loads and boundary conditions;

- Defining the optimization variables, e.g. objective functions and constraints;

- Defining, if necessary, the geometry restrictions, such as, optimize and non-optimize regions, symmetry axes;

- Run the topology optimization algorithm;

In the following sections will be briefly summarized the most common numerical methods of topology optimization including the SIMP method which stands for Solid Isotropic Material with penalization for intermediate densities, and the ESO method that stands for Evolutionary Structural Optimization, which is a design method based on the practical concept of gradually removing inefficient material from a structure (Huang & Xie, 2010).

2.5.2 Evolutionary Structural Optimization method

Evolutionary Structural Optimization (ESO) is an optimization process that continuously remove inefficient material from a structure according to the stress or strain energy levels of the elements. Over this process, the structure will evolve until reaching the optimal shape and topology. Among others topology optimization processes, the ESO is one of the most popular and was first proposed by (Xie & Steven et al., 1996).

Although the ESO optimization process can provide useful results for architects and engineers who are interested in exploring structurally efficient forms and shapes during the conceptual design stage of a project, it cannot guarantee that the evolutionary process would always produce the best solution (Huang & Xie, 2010). Figure 28 depicts the stiffness optimization of a cantilever beam in order to comply with distinct displacement constraints (u*). As expected, the most significant part of the material is removed near the free end where the stresses and cross sectional bending moment are lower. Moreover, as the displacement constraint increases, the flexural stiffness requirement decreases therefore the amount of material removed increases, see from Figure 28b to Figure 28d.

Some of the advantages of this optimization process are (Huang & Xie, 2010):

- It's a very simple concept and can be easily understood by the user;

- Does not require sophisticated mathematical programming techniques;

- No access to the source code of the finite element analysis (FEA) software is necessary;

- It can be readily implemented and linked to commercially available FEA software packages;

- The resulting design provides a clear definition of the topology (with no "grey" area);

- The ESO algorithm applies equally to general 2D and 3D problems;

- Does not require regenerating new finite element meshes even when the final structure has departed substantially from the initial design.
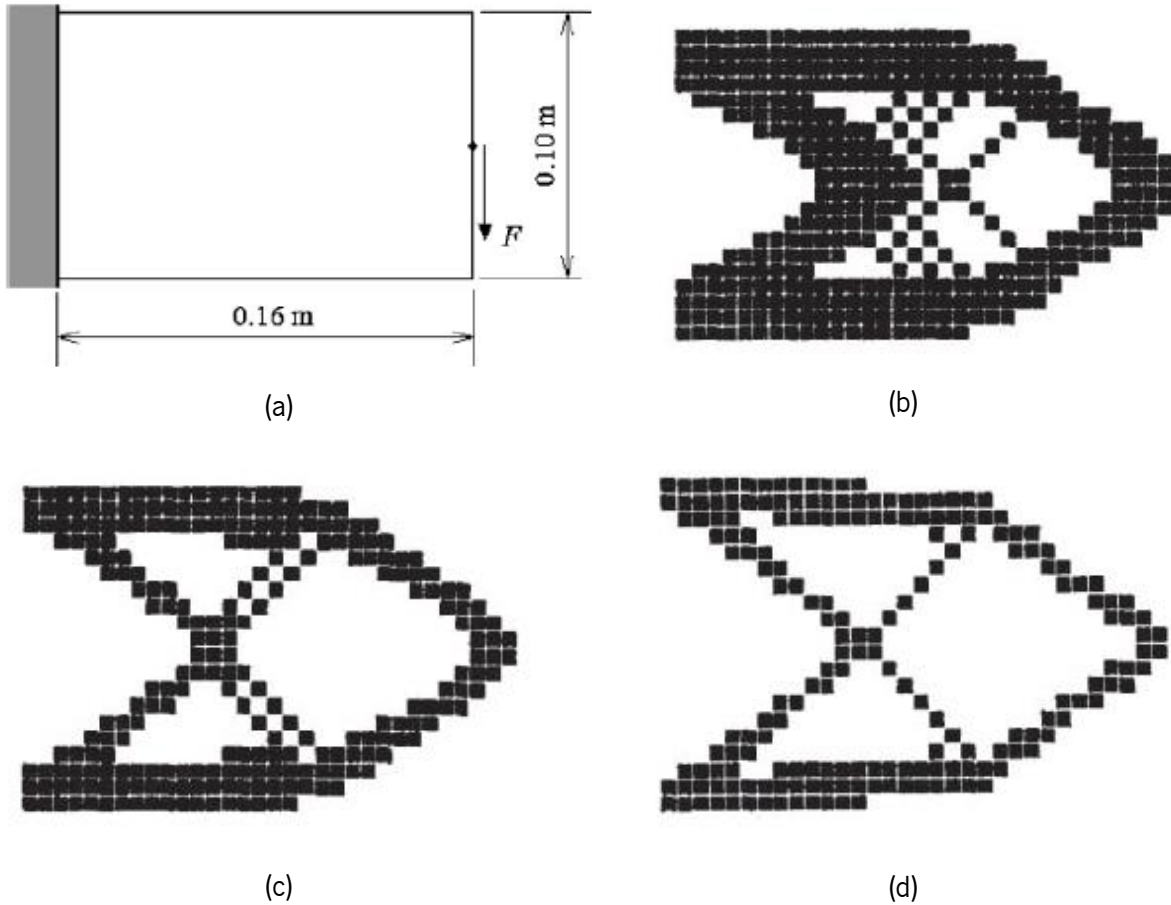
Figure 28 - Stiffness optimization with various displacement limits. (a) design domain of a short cantilever; (b) u* = 0.50 mm; (c) u* = 0.75 mm; (d) u* = 1.00 mm (Xie & Steven et al., 1996).

Figure 29 depicts an example regarding the stiffness optimization of a cantilever beam when using distinct mesh refinements. For a higher degree of refinement, the optimization surfaces were considerably smoother, as expected. Moreover, it is important to highlight that this refinement also affected the optimized topology by obtaining a distinct material disposition.

Figure 29 - Stiffness optimization of a short cantilever using different mesh sizes. (a) 48 x 30; (b) 64 x 40 (Chu et al., 1997).

2.5.3 Bi-directional evolutionary structural optimization method

The bi-directional evolutionary structural optimization (BESO) method like the ESO method also removes inefficient material from a structure, but beyond that it also adds material, simultaneously. (Yang et al., 1999) carried out one of the first known research on BESO method. The study was centered on the stiffness optimization, where the sensitivity number of the potential elements to be removed / or added were calculated through a linear extrapolation of the displacement field after the finite element analysis. After that, the algorithm removes the solid elements with the lowest sensitivity numbers and change into solid structure the void elements with the highest sensitivity numbers. The total number of removed and added elements in each iteration are determined by two unrelated parameters: the rejection ratio (RR) and the inclusion ratio (IR) respectively (Huang & Xie, 2010).

(Querin et al., 2000) also study the BESO method, applying it to "full stress design" by using the von Mises stress criterion. In their study, the elements with the lowest von Mises stresses are removed and it turns to solid those elements near the highest von Mises stress regions. Similarly, the number of elements to be removed and added are treated separately with a rejection ratio and an inclusion ratio, respectively. Figure 30 depicts a stiffness optimization of a short cantilever for a given volume constraint with BESO methodology. When comparing to the ESO method (see Figure 29), the BESO enables a higher quality of the optimized solution.

In brief, some advantages of the BESO method are (Huang & Xie, 2010).

- High quality topology solutions;

- Excellent computational efficiency;

- Algorithms easy to understand and simples to implement.

Figure 31 depicts the stiffness optimization of a centrally loaded beam for a given volume constraint with BESO methodology throughout the distinct iterations.

(a)

(b)

(c)

(d)

(e)

(f)
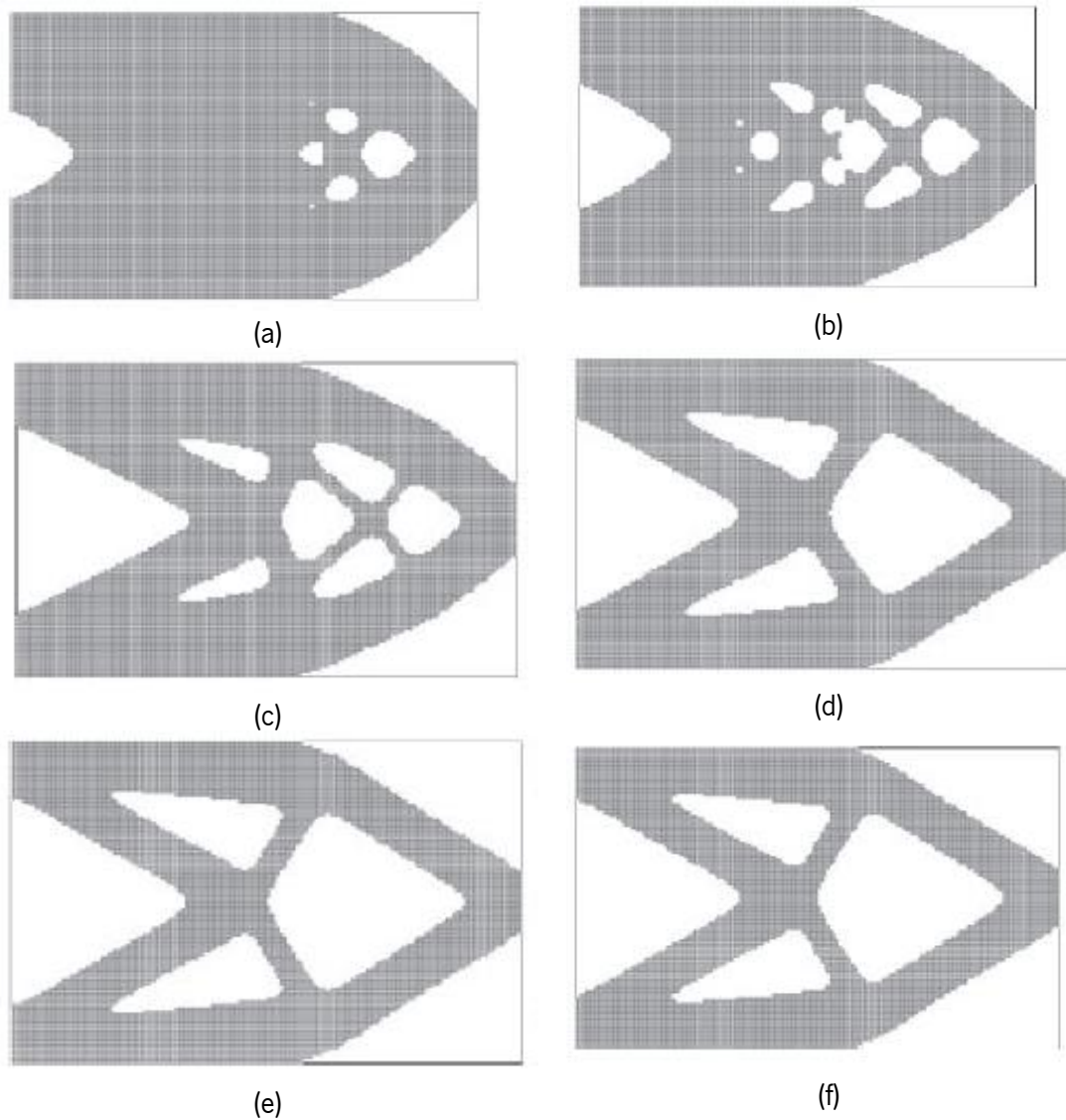
Figure 30 - Stiffness optimization of a short cantilever for a given volume constraint: (a) iteration 15; (b) iteration 30; (c) iteration 45; (d) iteration 60; (e) iteration 69; (f) final solution (iteration 79) (Huang & Xie, 2010).
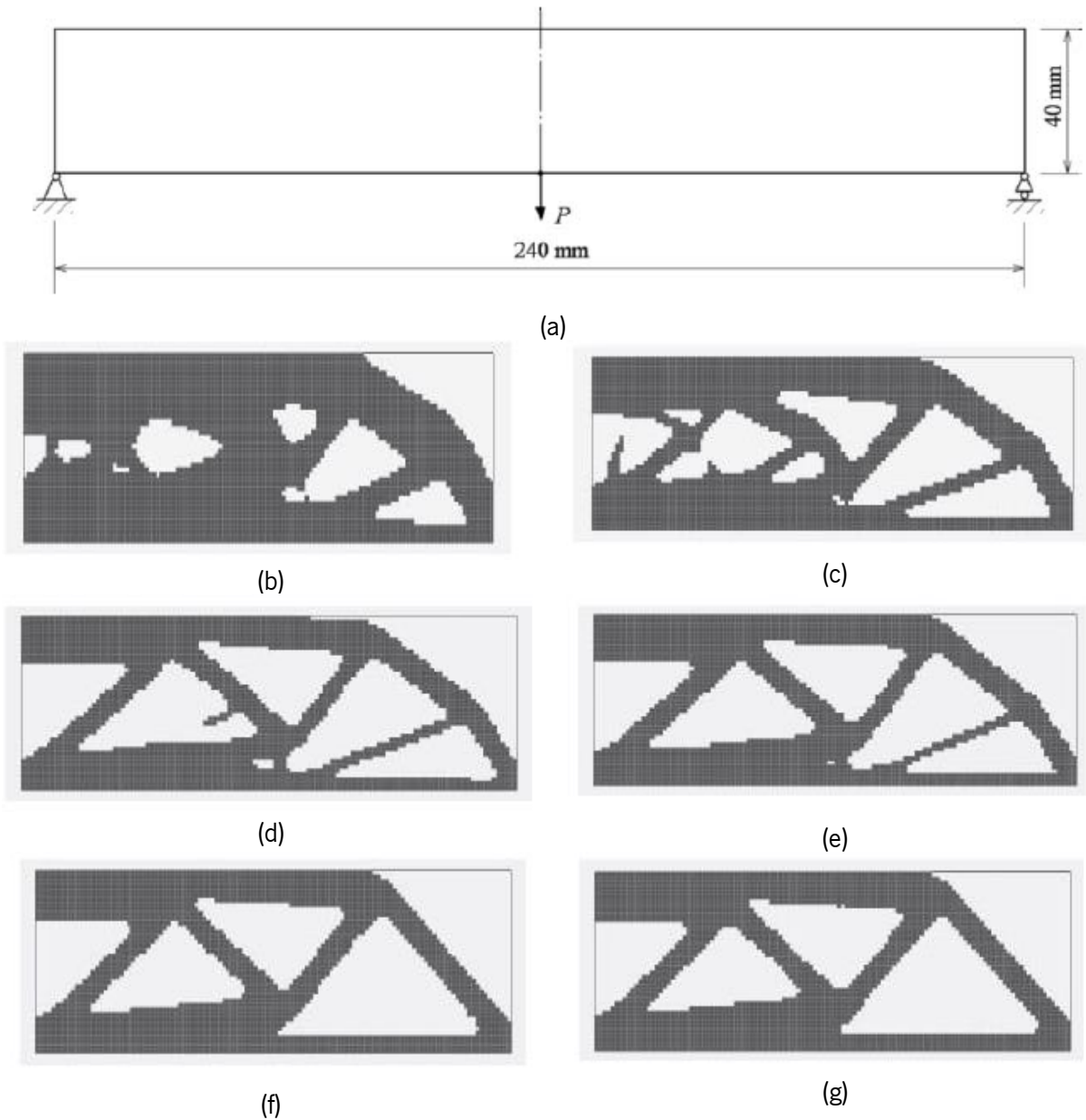
Figure 31 - Stiffness optimization of a centrally loaded beam for a given volume constraint: (a) design domain, boundary and loading conditions; (b) iteration 5; (c) iteration 10; (d) iteration 15; (e) iteration 25; (f) iteration 40; (g) final solution (iteration 53) (Huang & Xie, 2010).

2.5.4 Solid Isotropic Material with Penalization method

A topological optimization process has at least an objective function and a constraint. One example could be the minimization of the strain energy of the whole structure as objective function and a percentage of the initial volume as constraint. However, the design variables that are the relative densities of the elements will vary between 0 and 1 ($0 < p < 1$). With this variation in density, it will be created a variable density gradient that will exist in a new build domain. How it's not possible to manufacture components that have a density variation across their domain, the gradient will need to be corrected.

The Solid Isotropic Material with Penalization (SIMP) method is a common solution to this kind of problems. The method assumes that each element contains an isotropic material with variable density. The young's modulus of the intermediate density material is interpolated as a function of the element density, represented by $E_{xi} = E_1 * x_i^p$, where the original Young's modulus of the material E_1 is penalized by an external factor x_i^p, which will force a solution with nearly 0 or 1 material distribution, so the final solution will consist of either solid or void elements (Huang & Xie, 2010; Sigmund & Petersson, 1998). Figure 32 shows a beam topology optimization using the SIMP method for distinct penalization factors.

(a)

(b)
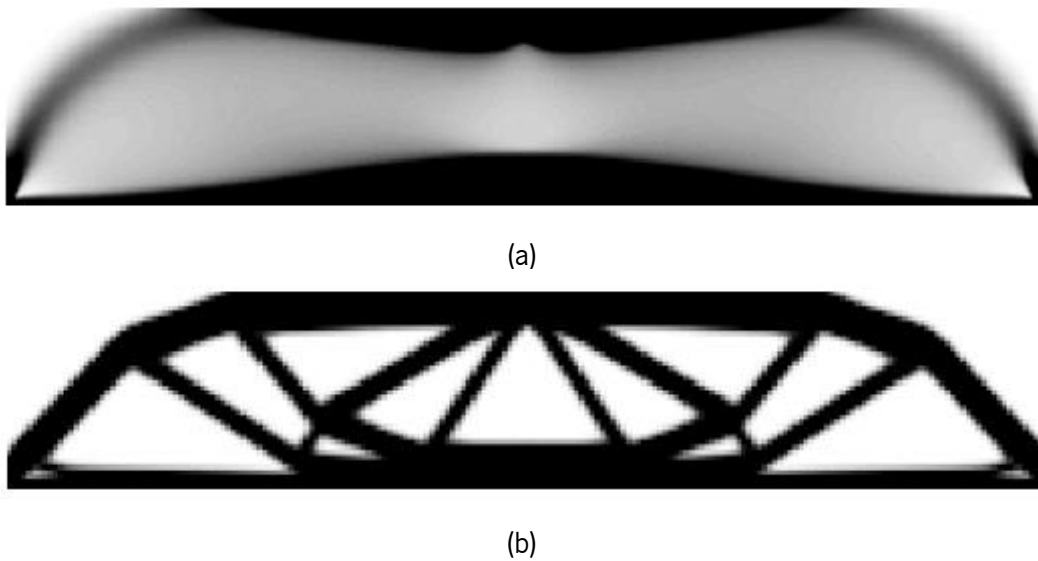
Figure 32 - Beam topology optimization using the SIMP method written in MATLAB. (a) optimized beam with penalization factor $p = 1$; (b) optimized beam with penalization factor $p = 3$ (Sigmund et al., 2001)

3. STUDY OF TOPOLOGY OPTIMIZATION SOFTWARE'S

3.1 Introduction

In this chapter it will be explained the steps that were made during the assessment of distinct commercial software for topology optimization. In an initial phase, it was done a brief research on different commercial programs that allow not only 2D and 3D modelling through the finite element method, but also topology optimization processes. With that said, in an early stage, it was tested a set of available programs for the purpose presented above. From the tested software, below are enunciated the ones that seemed having more potential to be further studied:

- Karamba3D for Grasshopper;
- Fusion 360 from Autodesk;
- SIMULIA Abaqus;

3.2 Advantages/disadvantages & conclusion

3.2.1 Karamba3D for Grasshopper

Grasshopper is a visual scripting platform that runs within Rhinoceros 3D computer-aid design (CAD). The program was designed and developed by David Rutten at Robert McNeel & Associates. The program allows the users to build precise and customizable Rhino objects by simply dragging components / boxes onto a canvas. Those components connect with each other throughout virtual wires. Many of Grasshopper's components enable in straightway fashion the creation of 3D parametric geometries, but also contain other types of algorithms, including numeric, textual, audio-visual and haptic applications. One of the great advantages of using visual programming language as a way of making 3D drawing is that allows to build a widely range of 3D geometries with very complex parametric relationships (Bachman et al., 2017).

Regarding AEC industry, Grasshopper software has very advanced functionalities, such as:

- Parametric modelling for structural engineering;

- Parametric modelling for architecture and fabrication;

- Lighting performance analysis for eco-friendly architecture;

- Building energy consumption.

Karamba3D is a parametric structural engineering tool, which provides accurate analysis of spatial trusses, frames and shells. It is fully embedded in Grasshopper, which makes it easy to combine parameterized geometries with finite element calculations and optimization algorithms like Galapagos, a Grasshopper native optimization algorithm (Rutten, 2013). It provides different type of analysis & algorithms such as (Preisinger et al., 2013):

- Linear analysis;

- Large deformation analysis;

- Buckling mode;

- Natural vibration;

- Optimization of cross section;

- Optimization for beam components;

- Optimization for shell components;

Karamba3D is a great tool that provides many different features & algorithms regarding structural analysis. After some research on the manual and forum from Karamba3D, unfortunately it was concluded that, at the present moment the calculation in Karamba3D is physically linear being not possible to assign nonlinear properties material to the structures (Karamba McNeel Forum), something that is crucial in the development of the present dissertation. So, in order to use Karamba3D in the current work, would be probably necessary to connect it with some external FEA program via a MATLAB script, or other (Wonoto & Blouin, 2018), something that would require more time than the available. With that said it was concluded that using Karamba3D for Grasshopper wouldn´t be the best solution.

3.2.2 Fusion 360

Fusion 360 is a product introduced by Autodesk and is a 3D computer-aided design (CAD), computer aided manufacturing (CAM), and computer-aided engineering (CAE) tool, that connects all the entire product development process in a single cloud-based platform that works on Macs and Pcs (Pradhan et al., 2019). Fusion 360 is a fully featured parametric cadet program that offers many of the features that other programs have, but with a more affordable price, and additionally offering a completed fully featured free student license.

When it comes to modeling, aside from the standard tools the program also includes capabilities such as environments for creating surfaces, free-form modeling and sculping, powerful direct modelling, mesh modeling, parametric modeling and it also offers an application programming interface (API) to enable third-party extensibilities (Pradhan et al., 2019). Besides that, the software also comes with a suite of tools for rendering and creating animations, ensuring that nearly every detail of the model is included.

Fusion 360 offers different simulation features such as (Autodesk):

- Static stress analysis;

- Nonlinear static stress analysis;

- Model frequencies analysis;

- Thermal stress analysis;

- Structural Buckling analysis;

- Event simulation;

- Topology optimization;

Lastly the software includes some manufacture features allowing additive and subtractive 3D printing with a widely range of plastic and metal materials. Figure 33 depicts a topology optimization process of a pinned supported beam, for a volume constraint of 40% of the initial volume of the flushed beam. This optimization was carried out under the scope of the preliminary analysis to assess Fusion 360 capabilities to optimize concrete structures.

Figure 33 – Topology optimization process of a pinned supported beam using Fusion 360 (for 40% of the initial volume).

Fusion 360 is a great all-in-one 3D modelling software offering many tools and features, starting with the 2D drawing, up to the final stage of 3D printing. It also supports collaboration and sharing via the cloud allowing the users the see real time changes in the model.

After testing the program and some research on the manual and forum from Autodesk, it becomes clear that this software is more suitable for mechanical engineering purposes, only allowing to assign to the structure materials with the same tensile and compressive behavior such as plastics and metals, which is a huge disadvantage because, in the scope of this dissertation it will be used fiber reinforced concrete material with completely different tensile and compressive behavior. So, it's possible to conclude that, unfortunately Fusion 360 does not meet all the necessary stipulated requirements.

3.2.3 SIMULIA Abaqus

Abaqus is a widely known finite element analysis (FEA) software with very advanced capabilities commercialized by SIMULIA from Dassault Systems S.A. The software includes (Dassault Systemes, Abaqus):

- Abaqus/Standard which is a general-purpose finite element program;
- Abaqus/Explicit, an explicit dynamics finite element program;
- Abaqus/CFD, a general-purpose computational fluid dynamics program;
- Abaqus/CAE, an interactive environment used to create finite element models, submit Abaqus analyses, monitor and diagnose jobs, and evaluate results;
- Abaqus/Viewer, a subset of Abaqus/CAE that contains only the postprocessing capabilities of the Visualization module;

Abaqus/CAE supports familiar interactive computer-aided engineering (CAE) concepts, such as feature-based, parametric modelling, interactive and scripted operation, and graphical user interface (GUI) customization (D.Systemes, Abaqus/CAE). The software offers a widely range of simulation and analysis, such as linear and non-linear material and/or geometric analysis, fluid simulation, event simulation, thermal stress analysis and many others, becoming a very advanced software with great calculating capabilities.

When it comes to 3D and parametric modelling the interface it is not that intuitive when compared with other 3D modelling software's (e.g. Fusion 360), but that isn't really a problem because it allows models/parts/drawings with other formats to be imported, such as .STL and DXF , which are commonly used in the 3D modelling & 3D printing industry (D.Systemes, Abaqus/CAE).

Relating to topology optimization Abaqus/CAE offers a widely range of optimization variables / design responses, such as (SIMULIA Abaqus manual 6.14):

- Strain energy;

- Volume;

- Displacement and rotation;

- Modal eigenfrequency

- Internal forces and moments

- Stress (scaled centroidal von Mises stress);

Figure 34 shows an example of topology optimization process using Abaqus/CAE for 40% of the initial volume, when considering distinct support conditions. These optimization processes were carried out under the scope of the preliminary analysis using Abaqus/CAE.
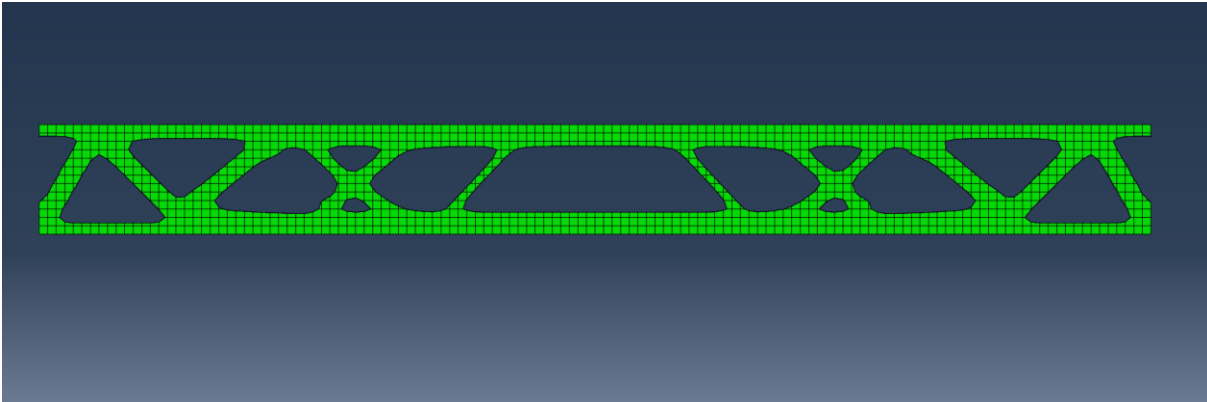
(a)
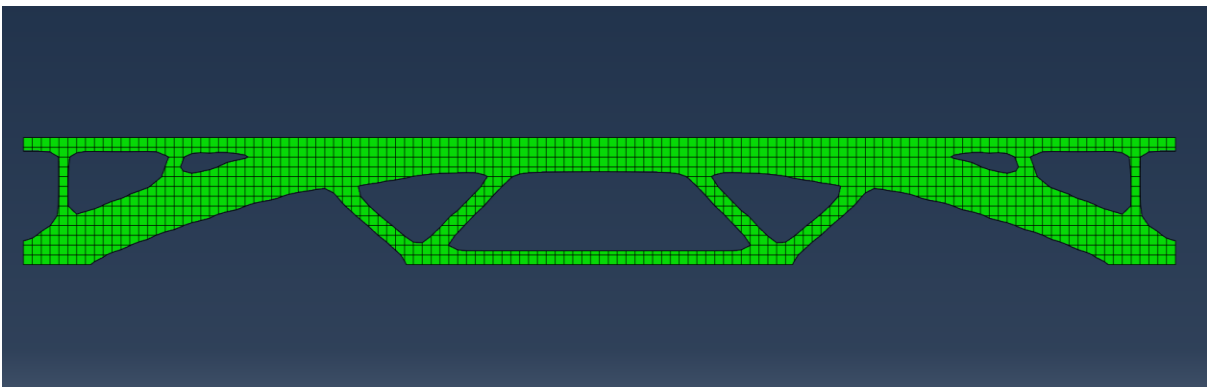
(b)

Figure 34 - Topology optimization process using Abaqus/CAE for 30% of the initial volume: (a) simply supported beam; (b) pinned supported beam.

Regarding to the nonlinear analysis, this software offers much more capabilities when compared to Fusion 360 and Karamba3D. The software supports a widely range of non-linear material models with different compressive and tensile behavior such as, concrete damaged plasticity, concrete smeared cracking and many others, becoming then possible to correctly model a fiber reinforced concrete material. With that said, it becomes clear that Abaqus/CAE is the most suitable software to be used throughout the present work (SIMULIA Abaqus manual 6.14). Nonetheless, as it will be discussed in Chapter 5, the adoption of non-linear material behavior during topological optimization procedure is limited to plasticity models for cast irons. Thus, more suitable models for quasi-fragile material, i.e. concrete, such as smeared crack model and concrete damage plasticity models are not possible to use during the optimization process.

4. Topology optimization - Parametric study

4.1 Introduction

In the present chapter, it will be carried out a parametric analysis regarding the influence of the variation of distinct variables on the topological optimization of a concrete beam, namely the height to span ratio (H/L), the support conditions, mesh refinement and optimization variables. This parametric analysis will be conducted on the software Abaqus/CAE. The selected case study is a beam with 6 meters long and 20 centimeters wide. The height will vary between a H / L ratio of 1/10, 1/5 and 1/3 corresponding to a height of 0.6 meters, 1.2 meters and 2 meters, respectively. Distinct support conditions will also be selected, varying between a simply supported beam a two pinned supported beam. Table 4 presents in summary the different geometrical dimensions and support conditions adopted during the parametric study.

During the optimization processes, it was assumed a concrete material with a strength class C60 (accordingly to Model Code 2010), i.e. a density, modulus of elasticity and Poisson ratio of 2500 kg/m^3, 39100 GPa and 0.2 respectively. Furthermore, it is important to state that only the linear elastic behavior was considered for all topology optimization processes.

Table 4 - H/L ratio and boundary conditions considered

Span (m)	Width (m)	Height / span ratio (H/L)	Support conditions
6	0.2	1/10 1/5 1/3	Simply supported Two pinned supported

Concerning the load case (LC) to be used in the parametric analyses of the optimization study, is was taken into consideration both the weight of the beam (SW) plus an overload (OL). The overload value will vary according to the area of the cross sections, as explained in 4.5.2. Since it was adopted three different heights for the parametric analysis, three different overloads were selected in order to take into account the distinct initial flexural stiffness. In the Abaqus software, the self-weight and the overload are applied through a gravitational load and a pressure load, respectively. The value of the overloads will be further detailed and explained in section 4.5.

As the load considered for all optimization processes will always be applied evenly distributed across the upper face of the beam, it can be assumed that it is equally positioned along the symmetry plane comprising the longitudinal axis of the beam and the resultant of the applied load, as shown in Figure 35. Due to symmetry, support and load conditions, it can be assumed a plane stress behavior, for the topology optimization study.
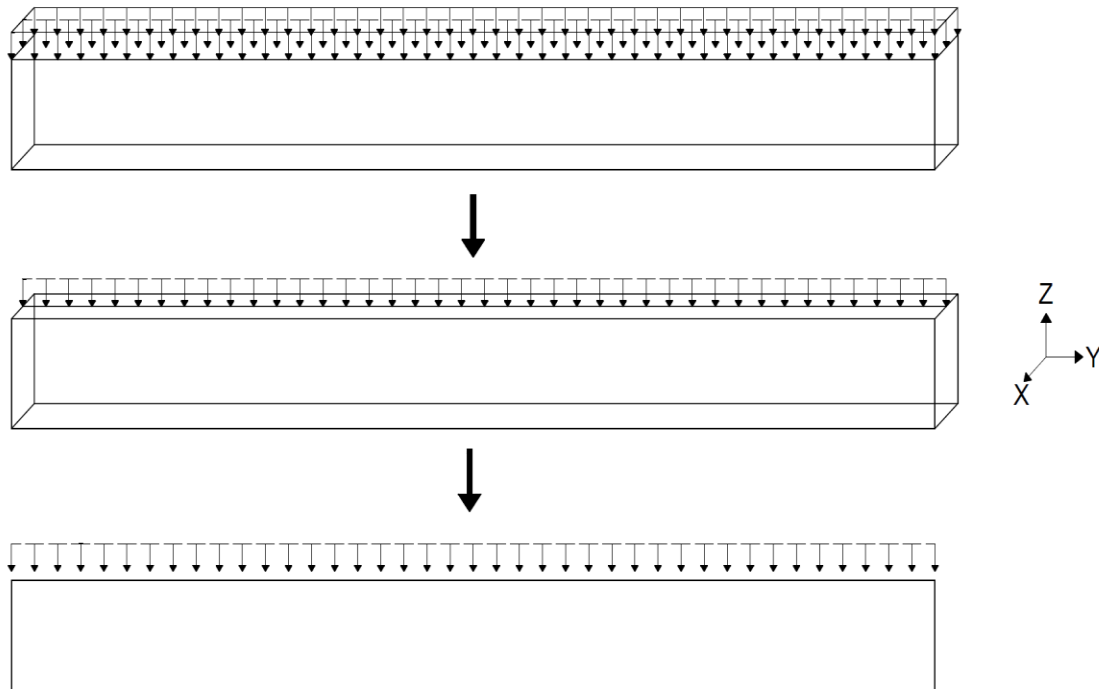
Figure 35 - Plane stress assumption

In Figure 36 is depicted an example of mesh used during the present study. In all finite element analysis, it was used 4 node linear plane stress elements. A full integration point scheme, i.e. 2 x 2 was adopted.

- CPS4, a 4 node Linear mesh element;
- Normal integration.
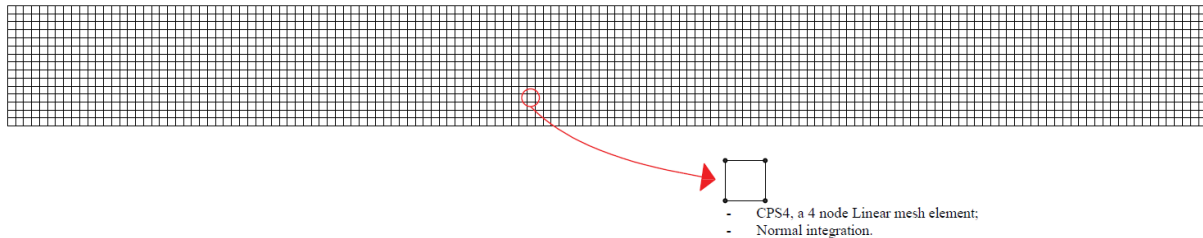
Figure 36 - Mesh element properties considered in the topology optimization processes.

For the topology optimization Abaqus/CAE supports two distinct algorithms, namely, the general sensitivity-based and the condition-based (SIMULIA Abaqus manual 6.14). The first one uses an algorithm that adjusts the density and the stiffness of the design variables, while trying to satisfy the objective function and the constraints, being partly described in (Bendsøe & Sigmund, 2003). The condition-based uses the strain energy and the stresses as input and was developed at the University of Karlsruhe, Germany and is described in (Bakhtiari, 1996). After exploring these two algorithms, it was notable that the sensitivity-based was more efficient, needing much less time to complete the optimizations and for this reason it was the chosen algorithm to be used in the present work.

It is important to mention that the algorithm allows to change multiple parameters. Regarding the present study, the material interpolation technique and the maximum change per design cycle that basically corresponds to the maximum amount of material that the algorithms can remove per cycle were adjusted for the present case study. For the material interpolation technique, it was chosen the SIMP method (described in a previous section) with a penalty factor of 3. On the other hand, for the maximum change per design cycle, the default value is 25%. It was perceived with the multiple analyses that the lower this value the more detailed the optimization is. However, lowering this parameter can rapidly increase the computational cost. After doing some experimental optimization processes, it was concluded that a value of 5% was the most suitable regarding balancing both the optimization time and quality. For more detailed information regarding these parameters care to consult the Abaqus Manual (SIMULIA Abaqus manual 6.14).

In order to undertake a topology optimization process, it is necessary beforehand to know which topology optimization's parameters lead to the best results. Additionally, it is also needed to know if the mesh

refinement can affect the topology optimization procedure. After some research the following optimization variables were selected to be further studied:

- Strain energy;

- Stress (scaled centroidal von Mises stress);

- Volume.

On the other hand, three type of mesh refinement were used in the parametric analysis:

- Coarse mesh refinement (CM);

- Medium mesh refinement (MM);

- Refined mesh (RM).

Table 5 summarizes the different parameters that will be assessed in the present chapter. Firstly, it will be studied which are the most suitable optimization variables and mesh refinement to be used. Afterwards, it will be analyzed the influence of height / span ratio (H/L) and support conditions in the optimization process.

Table 5 – Initial parameters adopted in the topology optimization

height / span ratio (H/L)	Optimization variables		Mesh refinement	Boundary conditions
	Objective function	Constraint		
1/10	Minimize strain energy	Volume constraint	CM	Simply supported
1/5			MM	
1/3	Minimize stress		RM	Two pinned supported

CM* - Coarse mesh refinement; MM* - Medium mesh refinement; RM* - Refined mesh

4.2 Abaqus/CAE optimization methodology

As stated and highlighted in section 3.2.3, Abaqus is an excellent software with very advanced algorithms regarding nonlinear analysis as well as topology optimization. Overall, the program is user friendly since it has a very intuitive graphic interface. Nonetheless, as many other advanced commercial finite element programs, Abaqus has an extensive finite element and material models library. The present chapter will be more focused in the topology optimization capabilities. Figure 37 shows a brief explanation of how a topology

optimization process works in Abaqus, from the geometry construction phase to the results visualization. For more details about the Abaqus/CAE optimization workflow consult (SIMULIA Abaqus manual 6.14).
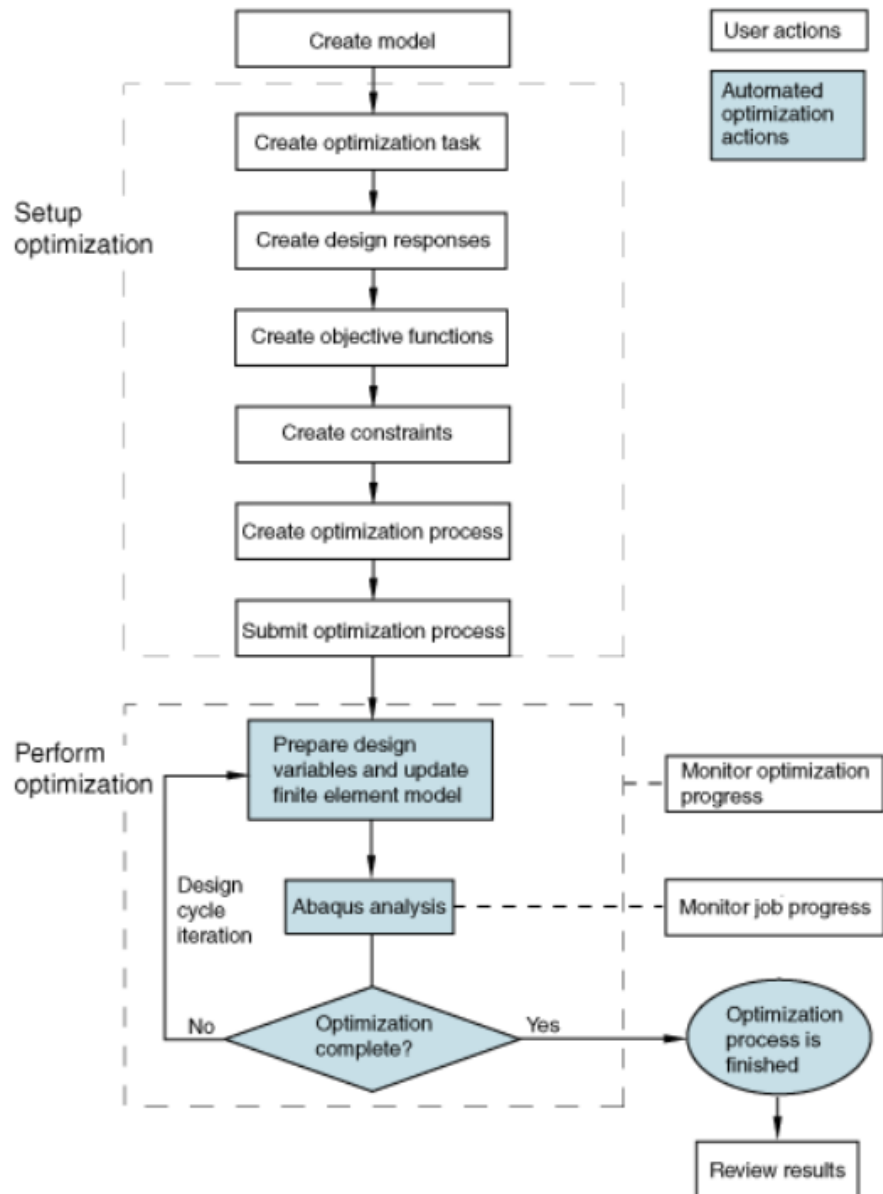
Figure 37 - User actions and automated Abaqus/CAE actions in the optimization process (SIMULIA Abaqus manual 6.14).

4.3 Influence of the optimization algorithm's variables

A topology optimization process must always have at least two optimization variables, one that will be the objective function of the problem and another that will work as a constraint. Abaqus/CAE provides a wide range of optimization variables (see section 3.2.3) and as stated in the last section the most appropriate ones to be used within the scope of the present dissertation would be the strain energy, stress and volume. Having that in mind, it was defined that the volume will always be the constraint, whereas the stress or strain energy will work as objective functions.

As the load case is driven by only external loads and no thermal field or prescribed displacements (SIMULIA Abaqus manual 6.14) the goal will be always to minimize the objective selected objective function. Table 6 shows the two sets of optimization variables selected for this study.

Table 6 - Optimization equations to be further study

Optimization variables	
Objective function (goal)	Constraint
Minimize strain energy	Volume constraint
Minimize Stress	Volume constraint

4.3.1 Optimization process considering strain energy as objective function

The objective here is to minimize de strain energy of the structure for a given volume constraint. As stated in Abaqus manual (SIMULIA Abaqus manual 6.14): *"The compliance of a structure is a measure of its overall flexibility or stiffness and is defined as the sum of the strain energy of all the elements, $\sum u^t k u$ for linear models, where u is the displacement vector and k is the global stiffness matrix. Compliance is the reciprocal of stiffness, and minimizing the compliance is equivalent to maximizing the global stiffness"*. Therefore, having in mind the aforementioned, minimizing the strain energy would be the same that maximizing the global stiffness of the structure, which is a goal commonly used in other academic works and it seems to be the approach that gives the best results (Grinde, 2018 & Rodrigues, 2014). Figure 38 depicts an example of a topology optimization procedure for a two-pinned supported beam by minimizing the strain energy.
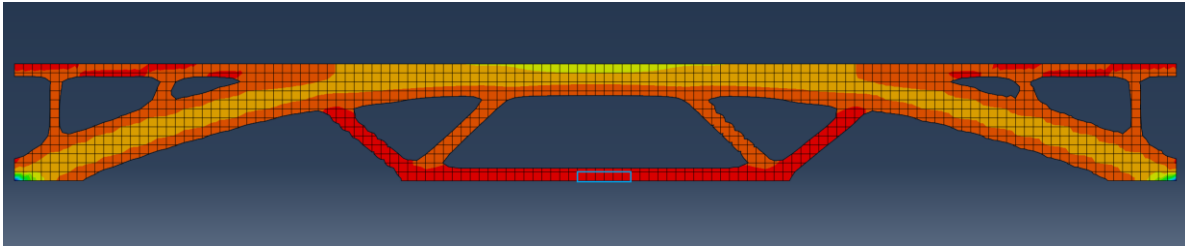
Figure 38 - Topology optimization using strain energy as objective function for a two-pinned supported beam with tensile max stress values around 1.11 MPa (blue signed area).

4.3.2 Optimization process considering stress as objective function

In this section, the stress is selected as an objective function by minimizing the maximum absolute stress value observed in a given volume, that is, the algorithm will optimize the structure's topology in order to obtain the minimum stress value in the bulk of the structure.

After analyzing the program's results, by using the stress as an objective function, it was found two disadvantages when compared to the strain energy method. The first one is that usually the optimization process is more time consuming and, the second is that the stress variable takes into account all the regions of the model including stress singularities caused by external loads or boundary conditions which results in shapes not that are not correctly optimized, with higher in-plane stress values in crucial regions of the structure, e.g. section at mid-span, when compared to the ones obtained with strain energy as objective function (see Figure 39a). When the support regions were disregarded in the optimization process, the results improved, but continued be worse than the ones obtained in 4.3.1 (compare Figure 39b and Figure 38). In the latter situation, although the maximum stress is reduced to levels more near the ones observed for the strain energy method (still they are nearby 76% higher for the stress approach), the quality of the optimization significantly lower when adopting the stress criterion.

(a)

(b)
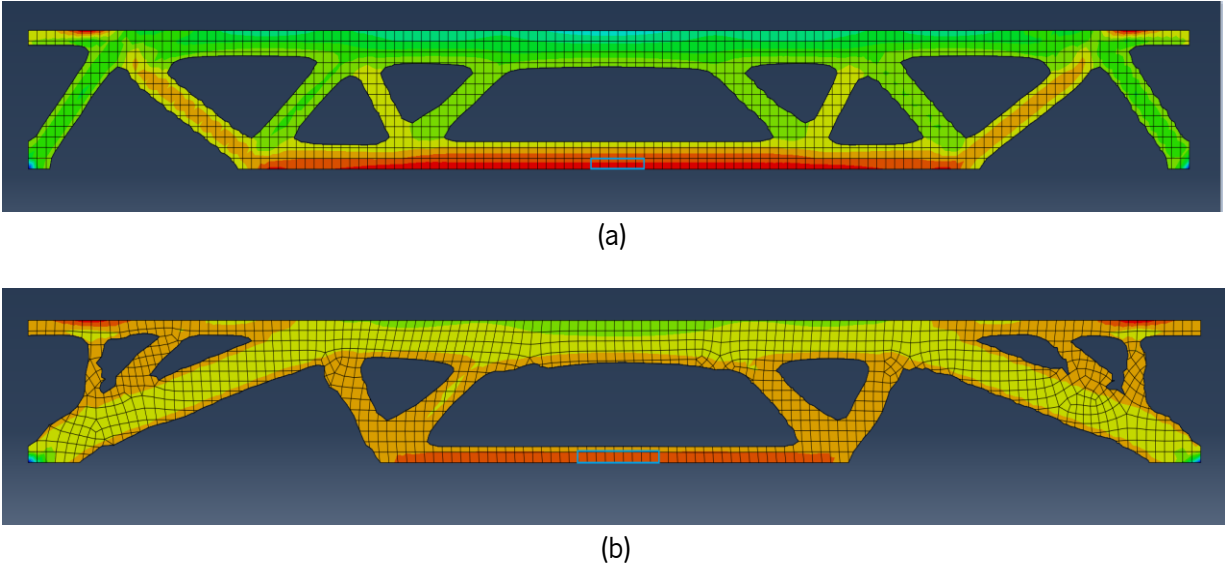
Figure 39 – Topology optimization using minimize stress as objective function. (a) Considering the whole structure in the optimization process, with max tensile stress values around 3.10 MPa; (b) Disregard of the support regions in the optimization process, with max tensile stress values around 1.96 MPa.

4.3.3 Conclusion

After an in-depth review of the two variables, it is possible to conclude that the "minimize strain energy" variable gives best results, being also the most used in other scientific works, strengthening the idea that should be the chosen one. Moreover, according to the Abaqus Manual, the variable stress as an objective function can only be used in static linear analysis and doesn't work when nonlinear materials are considered, "*Static linear analysis is supported. Static nonlinear analysis supports only contact nonlinearities. Nonlinear materials and geometrical nonlinearities, such as large deformations, are not supported*" (SIMULIA Abaqus manual 6.14).

Having that in mind, as well the optimization outcome when using the strain energy variable as an objective function, it was concluded that this approach would be more suitable for conducting the parametric study. Table 7 shows the final optimization parameters used in the parametric analysis, which were updated from the initially presented in Table 5.

Table 7 – Final parameters adopted in the topology optimization

height / span ratio (H/L)	Optimization variables		Mesh refinement	Boundary conditions
	Objective function	Constraint		
1/10			CM	
1/5	Minimize strain energy	Volume constraint	MM	Simply supported Two pinned supported
1/3			RM	

CM* - Coarse mesh refinement; MM* - Medium mesh refinement; RM* - Refined mesh

4.4 Influence of the mesh refinement

It is acknowledged that the higher the the mesh refinement the better the results from topology optimization will be. The main disadvantage is that certainly will be need more processing capacity and consequently will take more time to complete de optimization process. This section has the goal to ascertain which is the most suitable mesh refinement to be used that leads to detailed results without requiring too much computational time.

For this parametric study, as stated in section 4.1, three different mesh refinements were chosen. The coarse mesh (CM), the medium mesh (MM) and the refined mesh (RM). Figure 40 shows the three mesh refinements for the beam with 6 m long and a height of 0.6 m. On the other hand, Figure 41 shows the results after a topology optimization process considering the same support and load conditions, as well as the same volume constraint, which were 40% of the initial volume, for all processes.

(a)

(b)

(c)
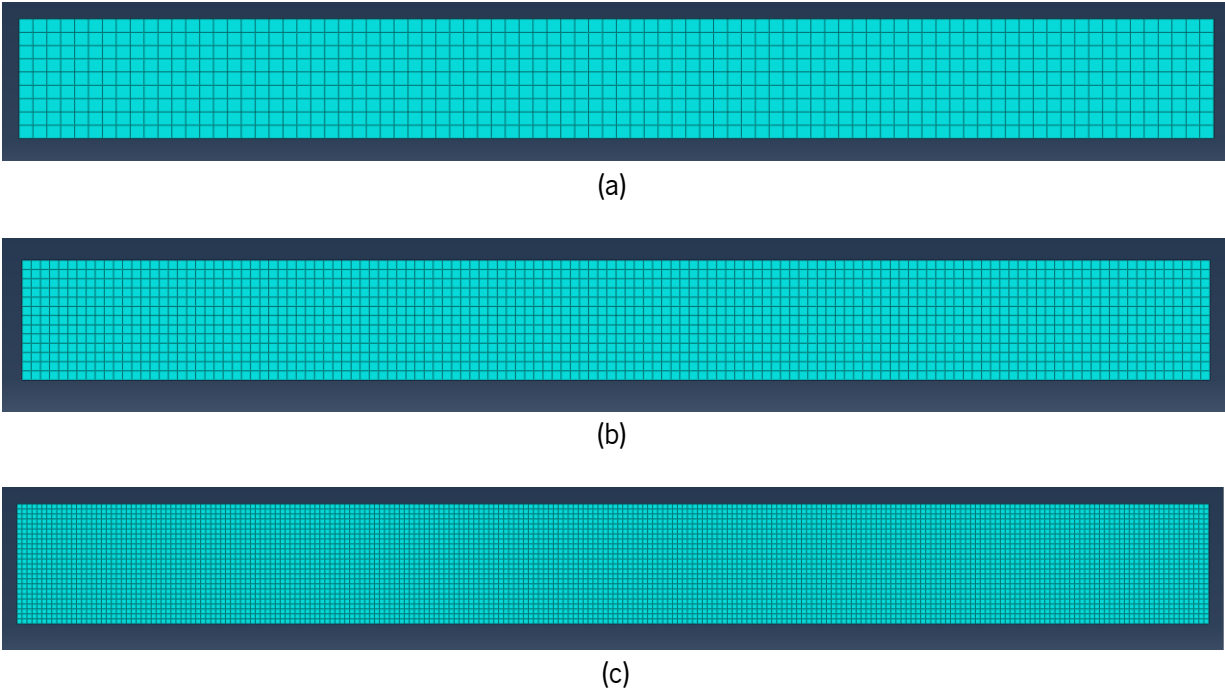
Figure 40 - Three types of mesh refinement. (a) CM - A 870 nodes mesh with approximately 70 mm squares; (b) MM – A 1834 nodes mesh with approximately 40 mm squares; (c) RM – A 6025 nodes mesh with approximately 25 mm squares.

(a)

(b)

(c)
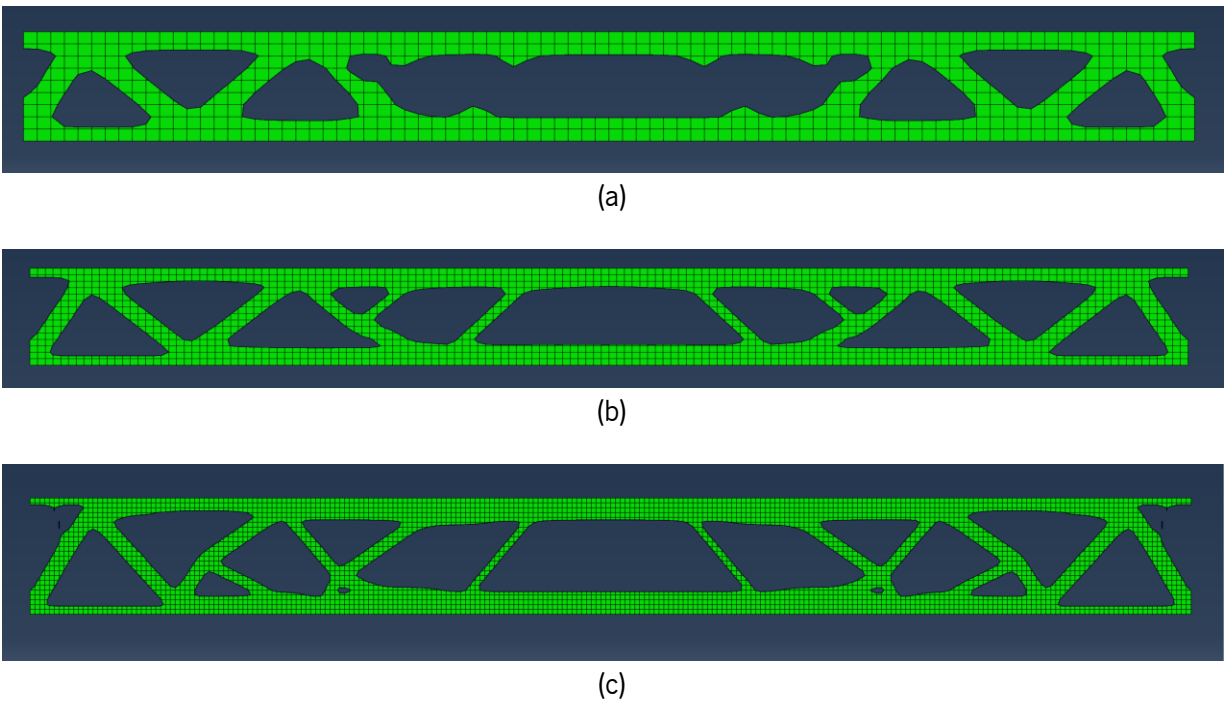
Figure 41 - Topology optimization results. (a) Coarse mesh; (b) Medium mesh; (c) Refined mesh.

Before comparing the optimization outcomes, is important to state that the Abaqus algorithm reached for all the three optimization processes with the distinct mesh refinements, the target of 40% of the initial volume.

After observing the figure above, it can be concluded that when using the coarse mesh, the topology optimization results in some areas, mainly at the mid-span region, was not so adequate. The refined mesh lead to higher definition and smoother geometries outcomes, but in some regions, mainly at the left and right top corners, the algorithm removed a lot of material, with max tensile stress values in that regions of around 2.25 MPa.

On the other hand, for the same regions, the result from using the medium refinement mesh lead to lower max tensile stress values of approximately 1.65 MPa. Furthermore, the results have a good geometry definition and overall seems to be the one that have the best material distribution. When it comes to computational cost, the optimization processes using CM and MM took approximately the same time, however the one using the RM took approximately three time more. With that said, it is possible to conclude that the medium mesh refinement (MM) seems to be to most suitable one to be used in the parametric analysis for the remaining defined variables.

4.5 Influence of the height to span ratio (H/L) and support conditions

4.5.1 Introduction

With the optimization variables and mesh refinement defined through the preliminary analysis, it is possible now to proceed the parametric study. In this section, it will be analysed the influence of the height to span (H / L) ratio, as well the support conditions in the optimization process.

The H /L ratio will vary between 1/10, 1/5, 1/3 and the support conditions will vary between a simply supported beam and a pinned supported beam as shown in Table 8. As stated before, the goal will be to minimize the strain energy for a volume constraint of 40% of the initial value.

Table 8 - Parameters that will be study in the experiment

height / span ratio (H/L)	Optimization variables		Mesh refinement	Boundary conditions
	Objective function	Constraint		
1/10 (H=0.6 m)	Minimize strain energy	Volume constraint	MM	Simply supported
1/5 (H=1.2m)				
1/3 (H=2m)				Two pinned supported

MM* - Medium mesh refinement

Firstly, will be defined the load case to be applied in the three beams. Thereafter a comparative analysis between the before and after optimization for the three beam's heights will be made, first for the simply supported conditions and then for the pinned supported conditions. To finish, some observations / conclusions regarding the influence of the H/L ratio and support conditions in the optimization process will be described.

4.5.2 Definition of the load cases

For the load cases (LC) as explained before the overload will vary according to the cross-section height, for the shortest height it was stipulated two LC corresponding to the self-weight (SW) plus a 5 kN/m overload (OL). Since the other two cross sections are much deeper, in order to apply an adequate OL, its value will be estimated in compliance with the relation of the moment of inertia of the cross sections, as calculated below):

- $I_{0.6} = \frac{0.2 \times 0.6^3}{12} = 0.0036$ m^4

- $I_{1.2} = \frac{0.2 \times 1.2^3}{12} = 0.0288$ m^4

- $I_2 = \frac{0.2 \times 2^3}{12} = 0.1333$ m^4

where $I_{0.6}$, $I_{1.2}$ and I_2 corresponds to the moment of inertia for the beam with a H / L ratio of 1/10, 1/5 and 1/3, respectively. Looking at the calculations previously performed, it's possible to conclude that the inertias for the sections with a H / L ratio of 1/5 and 1/3 are, respectively, eight and thirty seven times higher than the one corresponding to a 1/10 ratio. In order to standardize the applied overload, it will be adopted an OL of 40 kN/m and 185 kN/m for the beams with an H / L ratio of 1/5 and 1/3, respectively.

Note that, for the lower H / L ratios, the failure pattern will be dominated by inclined compression and shear-compression, in opposition to the higher 1 / 10 ratio in which the failure occurs by bending moment. Therefore, this procedure may be somewhat arguable, since it is standardizing the load regarding the flexural inertia, a possibility could be the utilization also of the shear area to standardize the applied load in a more rational fashion. The three adopted LC combinations are as follows (for the purpose, no load partial factors have been used):

- LC1 (H/10) = SW + 5 kN/m
- LC2 (H/5) = SW + 40 kN/m
- LC3 (H/3) = SW + 185 kN/m

With the load cases' combinations defined, it is possible to calculate the expected vertical reaction forces for the three geometries, before and after the optimization, respectively:

- $RF1 = \frac{((0.2 \times 0.6 \times 6 \times 2500 \times 10) + (5000 \times 6))}{2} = 24000 \text{ N} = 24.0 \text{ kN}$

- $RF2 = \frac{((0.2 \times 1.2 \times 6 \times 2500 \times 10) + (40000 \times 6))}{2} = 138000 \text{ N} = 138.0 \text{ kN}$

- $RF3 = \frac{((0.2 \times 2.0 \times 6 \times 2500 \times 10) + (185000 \times 6))}{2} = 585000 \text{ N} = 585.0 \text{ kN}$

- $RF1, \text{opt} = \frac{((0.4 \times 0.2 \times 0.6 \times 6 \times 2500 \times 10) + (5000 \times 6))}{2} = 18600 \text{ N} = 18.6 \text{ kN}$

- $RF2, \text{opt} = \frac{((0.4 \times 0.2 \times 1.2 \times 6 \times 2500 \times 10) + (40000 \times 6))}{2} = 127200 \text{ N} = 127.2 \text{ kN}$

- $RF3, \text{opt} = \frac{((0.4 \times 0.2 \times 2.0 \times 6 \times 2500 \times 10) + (185000 \times 6))}{2} = 567000 \text{ N} = 567.0 \text{ kN}$

Where RF1, RF2, RF3 are the expected vertical reaction forces before the optimization process for the LC1, LC2 and LC3, respectively, whereas RF1,opt, RF2,opt and RF3,opt are the vertical reactions after the optimization process for the LC1, LC2 and LC3, respectively. These reaction's values will be used to compare with the ones obtained through the static analysis in Abaqus/CAE in order to conclude if the loads were correctly applied as well as to quickly check if the optimization was performed to a certain target volume.

4.5.3 Influence of the H / L ratio for a simply supported beam

Figure 42 shows a schematic of the front view of the beam's geometry with distinct H / L ratios, support and load conditions for the three beams that will be optimized.

Beyond the visual assessment, before and after the optimization processes, some parameters related to the structure will be measured in order to evaluate the overall performance of the optimization. Those parameters were the:

- Strain energy of the whole structure;

- Tensile stress value at mid span;

- Displacement at mid span.

Firstly, after applying all the required settings related to parametric modelling such as, geometry, material and mesh properties, load and boundary conditions, it was performed an initial static analysis on the flushed beams, in order to measure the initial parameters values (i.e. strain energy, deflection at mid-span and maximum tensile stress at mid span) to be analyzed on the optimized structures, as shown in Figure 43. The values of those parameters are displayed in Table 9.

LC1

H = 0.6m

(a)

LC2

H = 1.2m

(b)

LC3

H = 2m

6 m

(c)
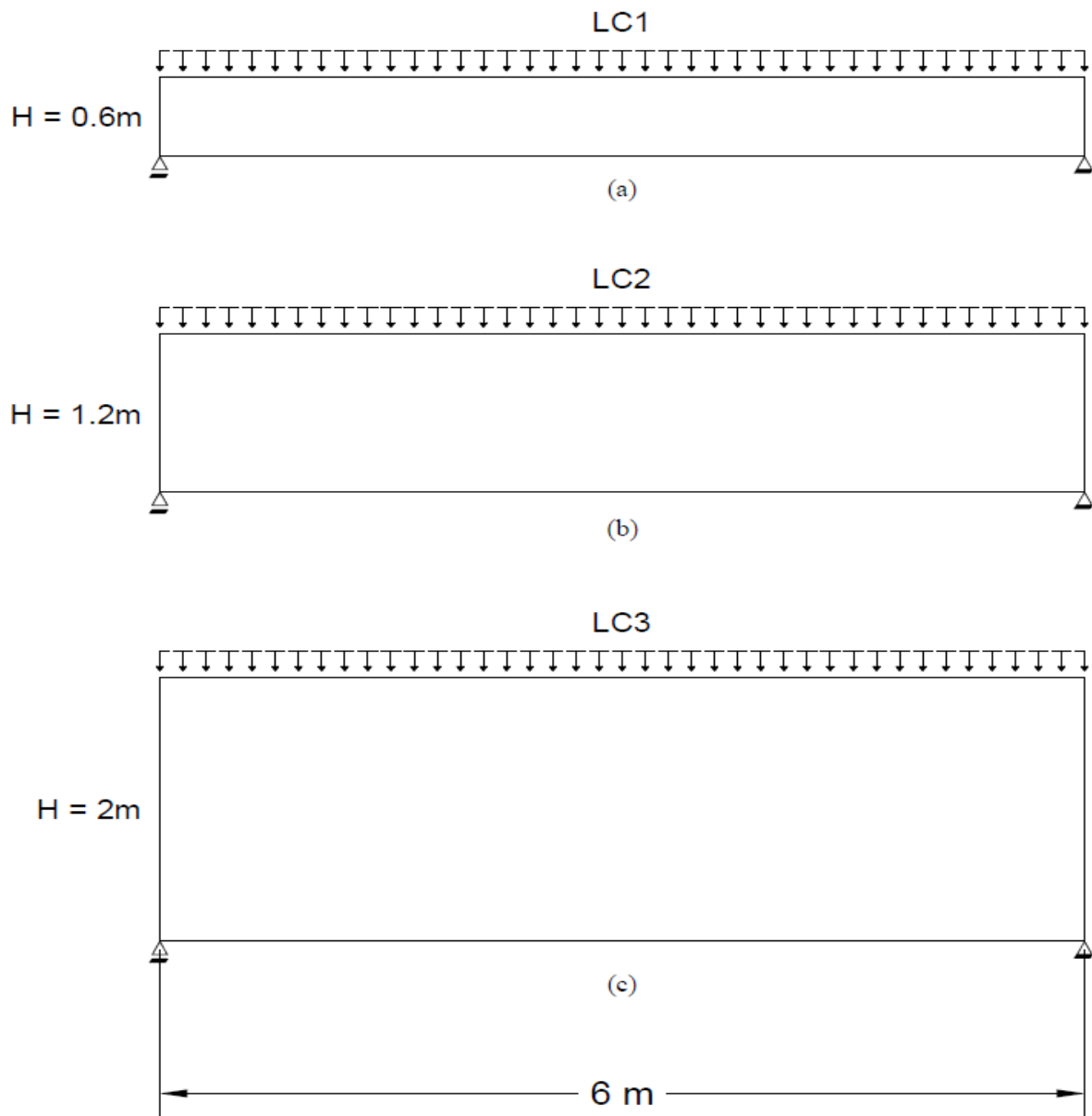
Figure 42 – Geometries that will be study in the section. (a) H/L = 1/10; (b) H/L = 1/5; (c) H/L = 1/3.

Figure 43 – Initial static analysis for the simply supported beam. The stress values are represented in the left column (MPa). (a) H/L = 1/10; (b) H/L = 1/5; (c) H/L = 1/3.

Table 9 – Parameters values before the optimization process for the simply supported beam

Height / span ratio (H/L)	Strain energy	Vertical reaction Force (kN)	Max. Tensile stress at mid span (MPa)	Displacement at mid span (mm)
1/10	15444	24.00	3.01	1.00
1/5	84035	138.00	4.36	0.88
1/3	671940	585.00	6.76	0.81

With the vertical reaction values being the same to the ones calculated before, it is possible to affirm that the loads were correctly applied. Before doing the optimization is important to state that the strain energy is obtained as the sum of the deformation energy of every single finite element.

The selected objective function for the optimization procedure was the minimization of the strain energy, which in summary is the same as increasing the structure's overall stiffness (SIMULIA Abaqus manual 6.14). Thus, the lower the strain energy value is, the higher the structure's stiffness will be.

After setting the variables and applying all the necessary requirements in the optimization module in Abaqus/CAE, the results obtained from the optimization with a target of 40% of the initial volume are shown in Figure 44. Table 10 shows the obtained output values of the parameters in order to evaluate the performance of the optimization.

Table 10 – Parameters values after the optimization process for the simply supported beam

Height / span ratio (H/L)	Strain energy	Vertical reaction Force (kN)	Tensile stress value at mid span (MPa)	Displacement at mid span (mm)
1/10	16784	18.59	3.82	1.48
1/5	129163	127.20	5.79	1.61
1/3	1011131	567.00	11.94	2.16

Looking to the vertical reactions, it´s possible to conclude that all the optimizations accomplished the goal of reducing the volume to approximately 40% of the initial value, with a maximum error of 0.05%.
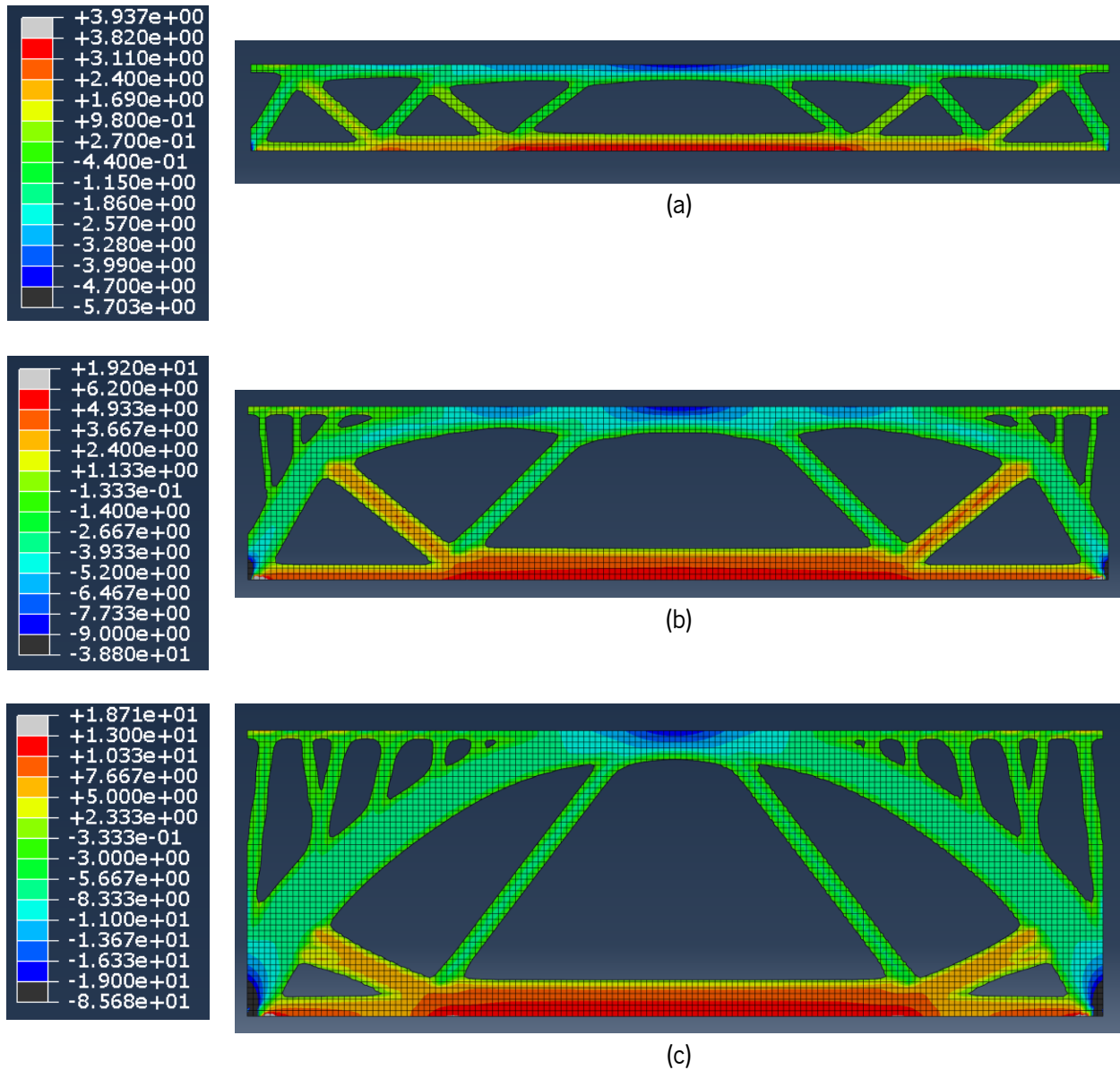
Figure 44 – Topology optimization outcomes, for a simply supported beam. The stress values are represented in the left column (MPa). (a) H/L = 1/10; (b) H/L = 1/5; (c) H/L = 1/3.

The optimization cycles for the three geometries can be seen in video format, in attachment A.

After a close look to Table 9 and Table 10, it is possible to state that the tensile stress and displacement values increased after the optimization, which was already expectable since that the overload value is superior than the self-weight for all the three beams. The strain energy column shows that the difference between the

before and after optimization increases accordingly to the H / L ratio growth, due to the pre-established exponential increase of the overload, where for the H / L ratio of 1/5 and 1/3, the self-weight basically has no influence when compared to the overload value.

Something that comes in sight is the arc-effect present in the highest beam. In the beam with an height of 0.6 m, as it still has a relatively low height, the optimization is more orientated to a trussed beam. In the beam with 1.2 m height, a mixed optimization was observed, between a trussed beam and the arc-effect, even though the beam functions as a truss.

On the other hand, on the deepest beam, it is clearly predominant the arc-effect, which is a great optimization solution, hence that the behavior of the structure will be predominantly under compressive stresses. In the present optimization solution, it was obtained a lower flange connecting the two support regions that is mostly subjected to tensile stresses and acts in certain way as an elastic horizontal support enabling the formation of the arch.

4.5.4 Influence of the H / L ratio for a pinned supported beam

In this section, it will be executed the same procedure done in section 4.5.3, but for a pinned supported beam, i.e. with two supports restraining the translation degrees of freedom along both the horizontal and vertical directions. The geometries and consequently the relation between the beam's height and span will be the same as the ones presented in the previous section. Figure 45 shows the initial static linear analysis for the three beams. The initial parameters values that will be monitored in the optimization process are included in Table 11.

Comparing these initial values to the ones obtained from the analyses carried out with simple support conditions (see Table 10), i.e. without restraining the horizontal displacement in the left support, it is noteworthy to mention that the maximum deflection and total strain energy were significantly lower than for the support conditions presented in section 4.5.3.
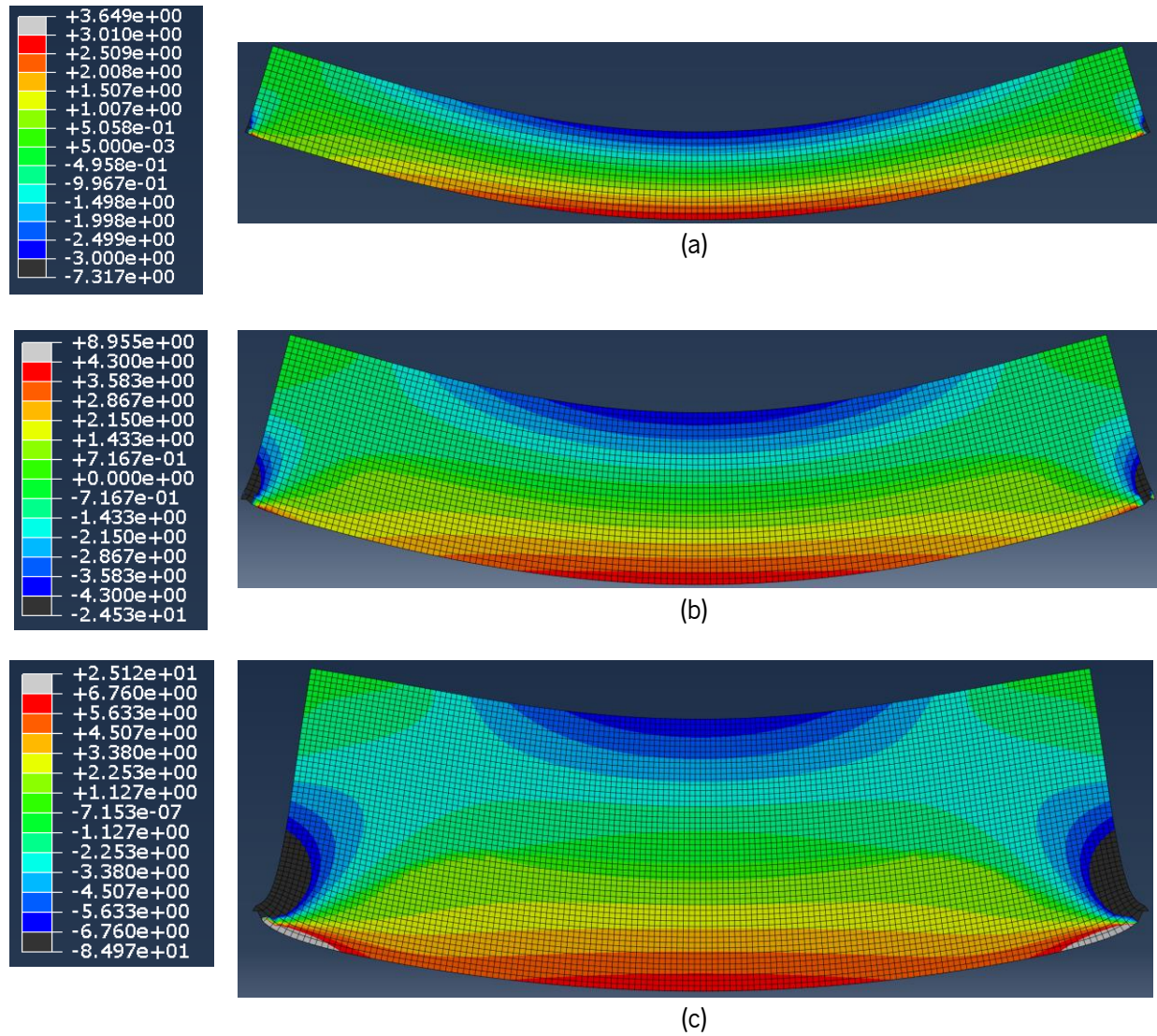
(a)

(b)

(c)
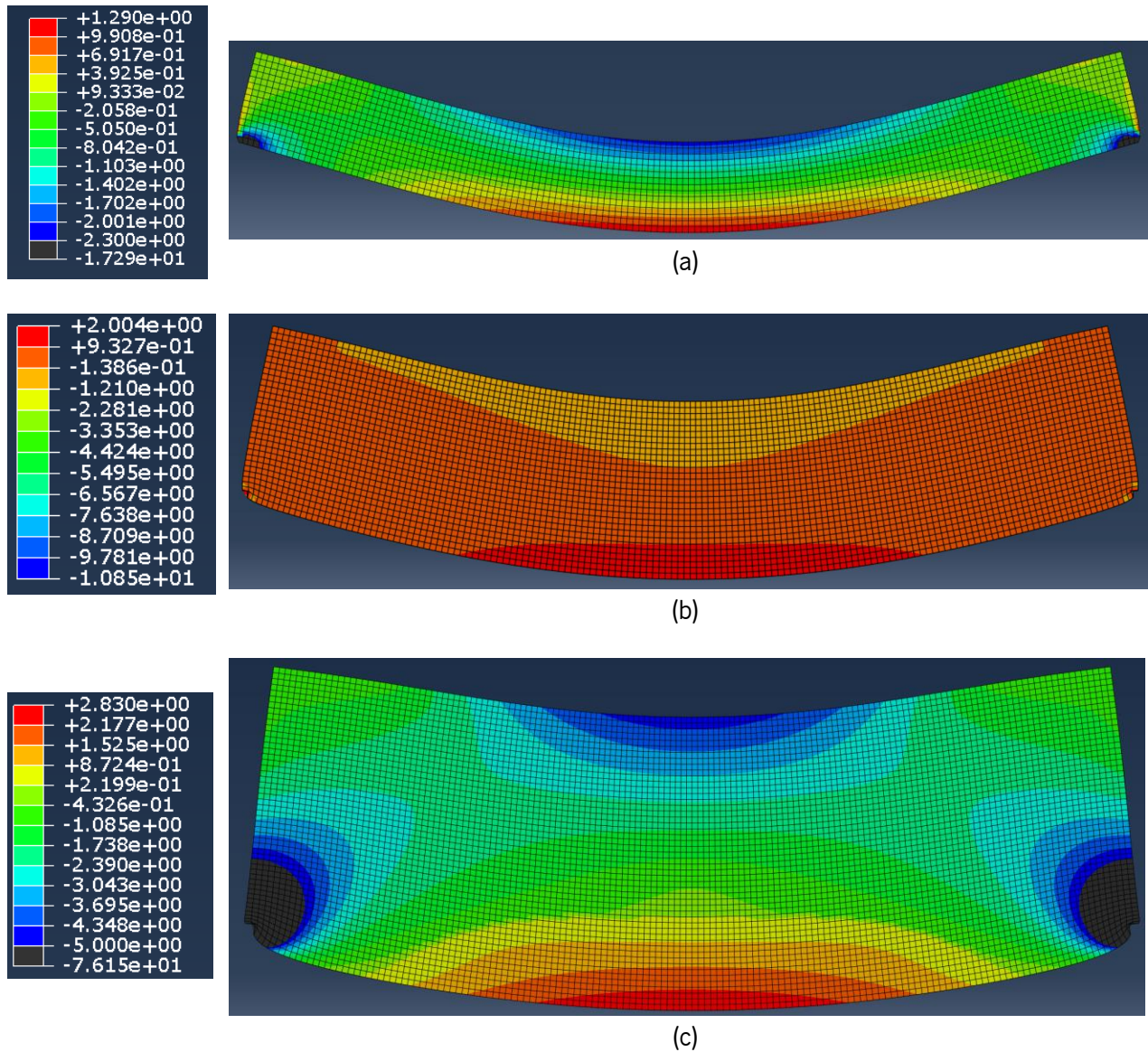
Figure 45 – Initial static analysis for the pinned supported beam. The stress values are represented in the left column (MPa). (a) H/L = 1/10; (b) H/L = 1/5; (c) H/L = 1/3.

Table 11 – Parameters values before the optimization process for the pinned supported beam

Span/beam height ratio (H/L)	Strain energy	Vertical reaction Force (kN)	Tensile stress value at mid span (MPa)	Displacement at mid span (mm)
1/10	7042	24.00	1.29	0.48
1/5	42793	138.00	2.00	0.47
1/3	390741	585.00	2.71	0.45

After the initial static linear analysis with flushed section, the topology optimization was performed. Figure 46 depicts the final beam's geometry after optimization for a target of 40% of the initial volume.

Table 12 shows the values of the parameters selected to evaluate the performance of the optimization.
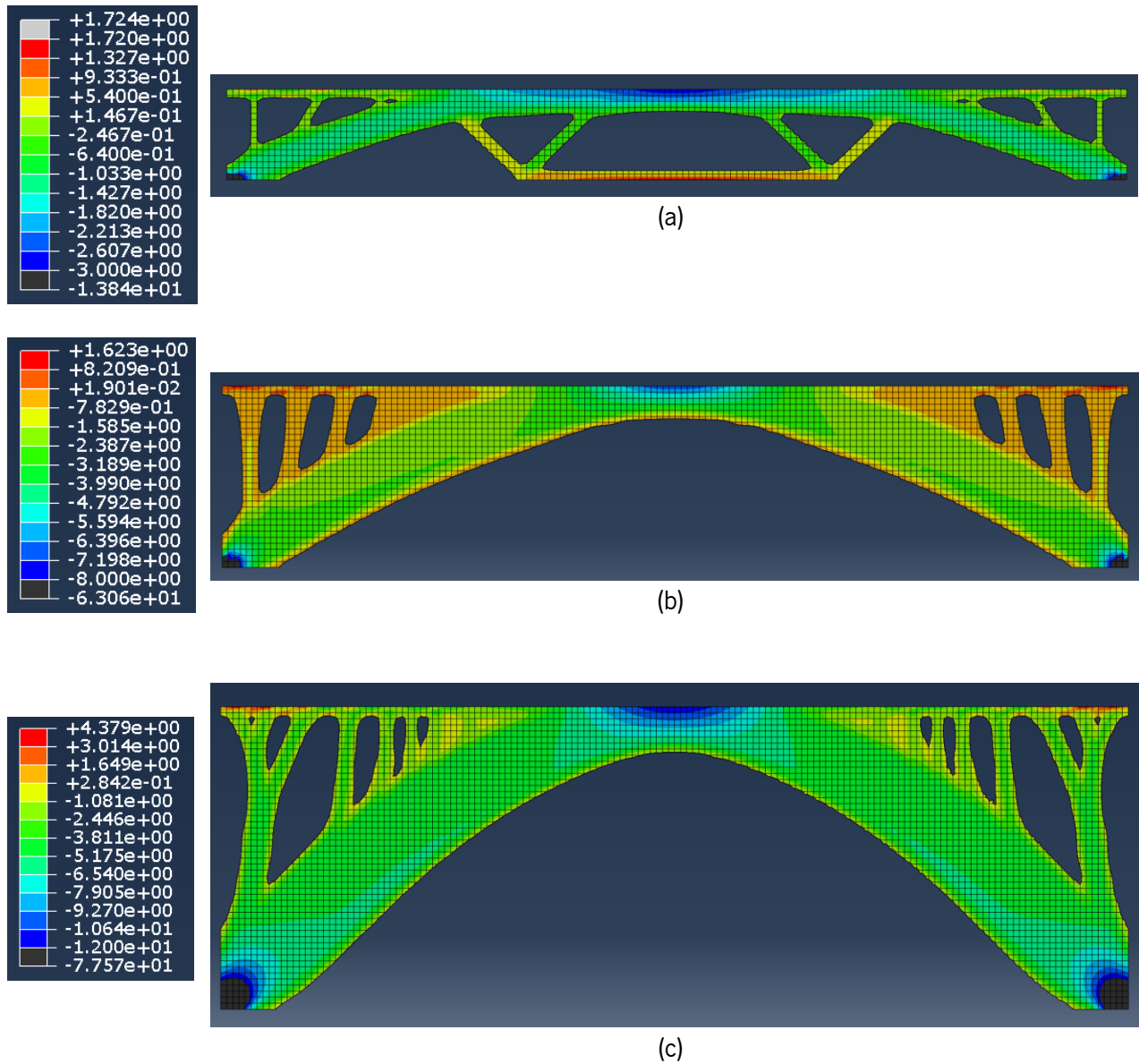
Figure 46 – Topology optimization outcomes, for a pinned supported beam. The stress values are represented in the left column (MPa) (a) H/L = 1/10; (b) H/L = 1/5; (c) H/L = 1/3.

The optimization cycles for the three geometries can be seen in video format, in attachment B.

Table 12 – Parameters values after the optimization process for the pinned supported beam

Span/beam height ratio (H/L)	Strain energy	Vertical reaction Force (kN)	Stress value at mid span (MPa)	Displacement at mid span (mm)
1/10	6590	18.60	1.72	0.69
1/5	57593	127.72	-7.03*	0.82
1/3	500480	567.00	-11.60*	1.26

* Maximum compressive stress observed at mid-span

As the displacements are restrained in the two directions by the two pinned supports, the algorithm automatically recognizes that the formation of an arch would be more efficient in terms of minimizing the strain energy and transferring the applied loads to the bearings, turning the structural behavior predominantly under compressive stresses. The latter is particularly evident for the beams with a height of 1.2 and 2 m. By looking at Table 12 and Figure 46, it is possible to see that at mid-span, there is no fibers subjected to tensile stresses, making the behavior of them purely at compression, simulating an arch bridge. Moreover, the level of compressive stresses is relatively low for current concrete strength classes, which indicates that in the case of this support conditions the structural topology can be further optimized by using less material. Even the 0.6 m height beam, which has a very low height, has shown the formation of the arch effect during the optimization process. Nonetheless, because it is a very open arch the central part of the beam is governed predominantly by flexure, for this reason it is logical that a mixed truss / arch solution was obtained during the optimization process. Note that the formation of the truss in the beam's central part ends at when the arch curvature starts to be more pronounced, i.e. where it starts being more effective as an arch. In contrast, the two deepest beams allow for a more pronounced arch curvature, i.e. resulting in a more closed arch, then requiring no lower material.

4.5.5 Conclusions

After an analysis of the results, it was possible to state the all the outcomes were well refined, and the overall shape optimizations were successfully carried out in order to make the structures as stiff as possible, which leads to conclude that the study of both the mesh refinement and the optimization variables were important to obtain adequate results. The study of the most suitable algorithm settings, such as the material interpolation technique (MIT) and the maximum change per design cycle (MCDC), also played a key role in the optimization process, and although the minimizing of the MCDC parameter value lead to increasing of the optimization cycles and consequently an increase of the computational costs, it certainly had a great impact in the overall quality of the optimization outcomes.

Looking to the strain energy values between the two cases it becomes noticeable that the analyzed parameters (i.e. strain energy, maximum stress and displacement) for the pinned supported beam do not increase as much as in the simply supported case. For the beam with a height of 0.6 meters with pinned supported conditions, a decrease on total strain energy was observed. Overall, the increase of the deflection and strain energy on the optimized solution when compared to the flushed section is in part due to the high relation between the overload and self-weight load, which leads to reduction of the displacement' component due to the self-weight load not being as preponderant as the one due the overload.

Focusing on the appearance of the results and on the maximum stress values displayed in the present tables, it is possible to conclude that the as deeper the beam and as more horizontal constraints, the more prevalent the arch effect and having a structural behavior predominantly under compression.

4.6 Study of the reinforcement amount in the optimization process

In this section, it will be done a study regarding the influence of the reinforcement amount in the topology optimization process. For the present case study, the beam with an H / L ratio of 1/10 and with simple support conditions was selected. In order to proceed to this study, it was calculated the reinforcement area (As) considering the self-weight plus an overload of 50 kN/m, as shown in Figure 47.

LC = SW + 50 kN/m
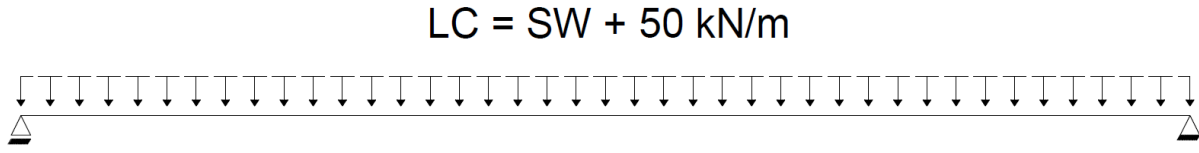
Figure 47 – Load case and support conditions

For this study it will be carried out five optimization processes, one considering the necessary reinforcement (*As*) for the load case displayed above, three others considering half, one quarter and an eighth of *As* and a last one considering one and a half of the initial reinforcement.

It was considered the utilization of an C60/75 concrete and S500-B rebars as reinforcement. The calculation of *As* was done using the simple bending tables and assuming that there is only tensile reinforcement usage. The ratio a / h is equal to 0.0667, where it represents the beam's utile depth, as shown in Figure 48.

h = 0.6m

a = 0.04m
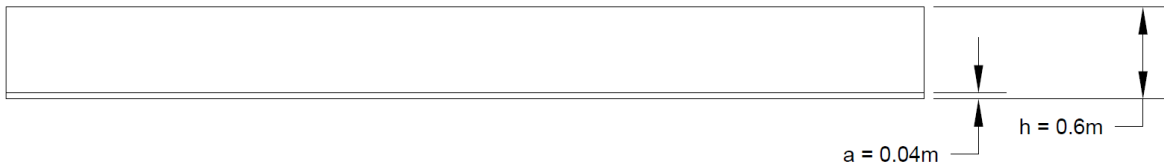
Figure 48 – Scheme showing the relation a/h

For a 50 kN/m load the maximum moment at mid-span is approximately $\frac{p \times l^2}{8} \cong 225 \ kN.\,m$. With that said, $u = \frac{M_{rd}}{b \times d^2 \times f_{cd}}$, where M_{rd} is the maximum moment at mid span, b and d are the width and height of the beam and, u is the reduced moment, being approximately 0.078. Consulting the simple bending tables, the mechanical percentage of reinforcement (*w*) was estimated at 0.088.

Thereafter, knowing that $w = \frac{As}{b \times h} \times \frac{f_{yd}}{f_{cd}}$, where, f_{yd} and f_{cd} are the design stress for reinforcement and concrete respectively, it's possible to calculate the value of the reinforcement area (As), being approximately 972 mm^2.

Table 13 shows the other values of the reinforcement amount that will be use through the optimization processes.

Table 13 - Reinforcement amount for the five optimization processes

Optimization process	Reinforcement Amount (As)	Cross sectional area (mm^2)
1	1.5 As	1458.0
2	As	972.0
3	0.5 As	486.0
4	0.25 As	243.0
5	0.125 As	121.5

Figure 49 shows the results of the topology optimization for the five processes with distinct reinforcements.

(a)

(b)

(c)

(d)

(e)
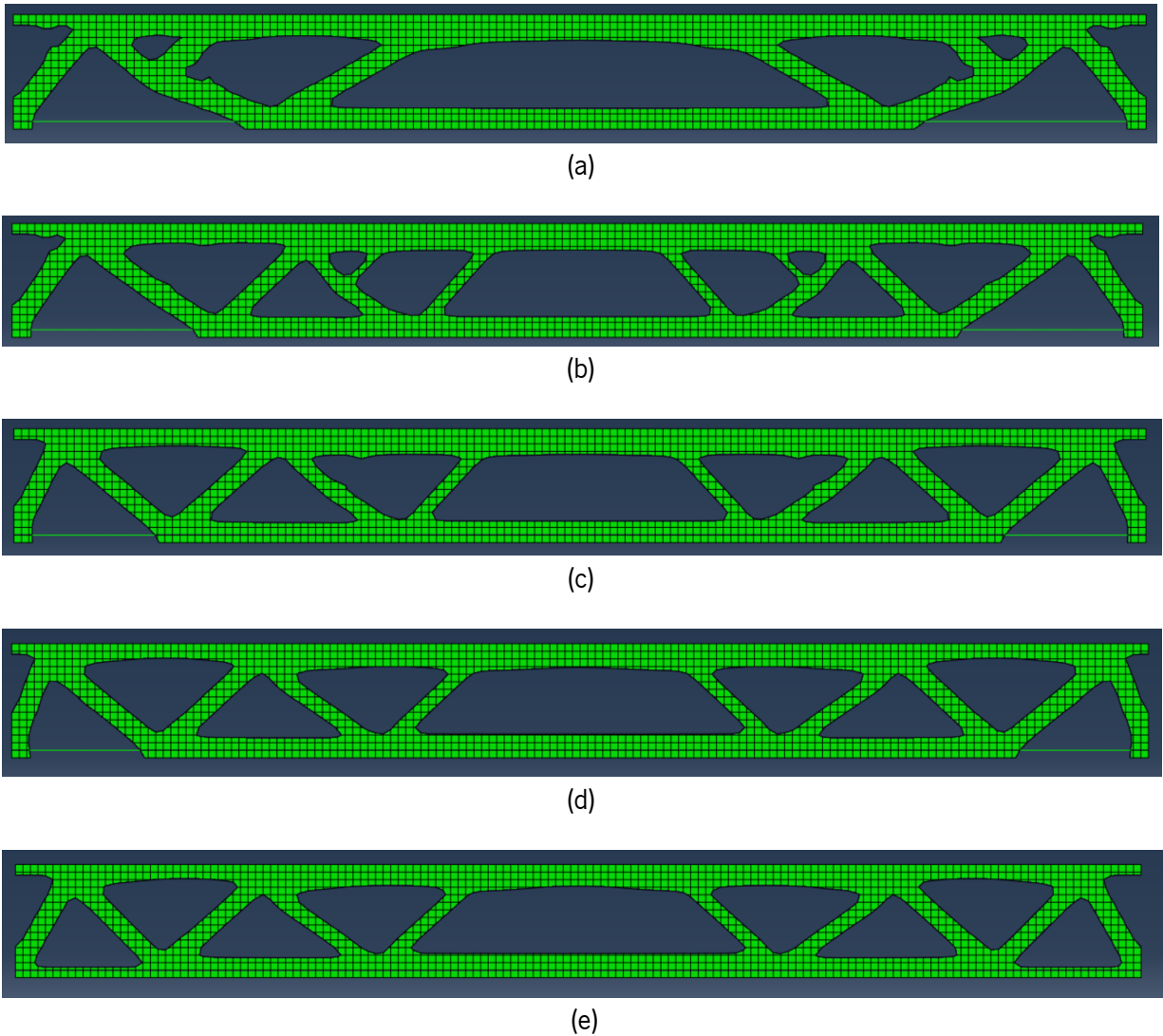
Figure 49 – Outcomes of the five optimization processes. (a) 1.5 As; (b) As; (c) 0.5 As; (d) 0.25 As; (e) 0.125 As

It's important to state that all the topology optimization processes reached the goal of reducing the volume in 60% and that all the mesh properties and optimization settings remained the same that were used in 4.5.

After a close look to the results, it becomes noticeable that the main difference between the five outcomes is the amount of materials in the inferior flange of the beam. By comparing all five optimization processes, but especially the beam with higher reinforcement area (Figure 49a) with the beam with lower *As* (Figure 49e) it becomes clear that, with a higher reinforcement area, a higher horizontal load can be transferred to the supports. This allows distributing a higher level of tensile stresses in the lower flange of the beam to the

supports, hence less material will be added to the regions near the supports where the bending moment is very reduced and consequently the tensile stresses in the beam's bottom part. The algorithm uses that leftover material to reinforce other important regions of the beam e.g., the connecting rods and superior flange.

4.7 Influence of the mesh refinement in 3D optimization

In this section, it will be assessed the influence of the mesh refinement in a three-dimensional optimization. The geometry to be optimized will be the one corresponding to the deepest beam, i.e with a height of 2 m, considering the supports conditions as simply supported. For the load will be applied the LC3, the same explained in section 4.5. The geometry, supports conditions and load case are shown in Figure 42c.

In order to assess the influence of the mesh refinement, four different meshes will be used, one considering a 90 mm maximum edge dimension of the finite element , and the other ones considering 70, 40, and 25 mm for the edge dimension of the finite element. Thereafter will be also compared the values of strain energy, displacement and stress, for the 40 mm mesh size, with the ones obtained in Table 10, in order to evaluate the plane stress assumption.

Figure 50 and Figure 51 present the outcome of the four optimization processes for the distinct adopted mesh refinements. The optimization cycles for the beam with 40 mm of mesh size can be seen in video format, in attachment C.

Table 14 comprises the values of the strain energy, displacement and stress for the 40 mm mesh size.
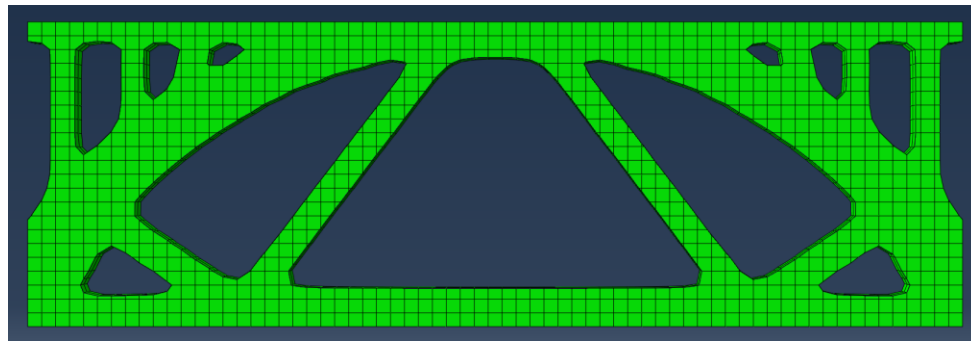
(a)
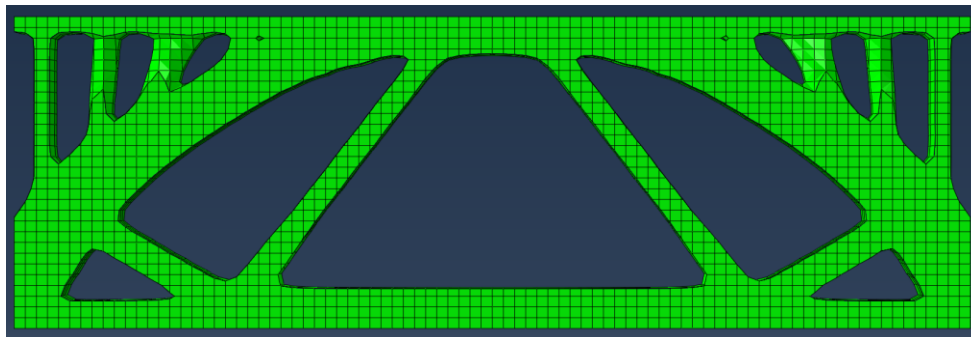
(b)
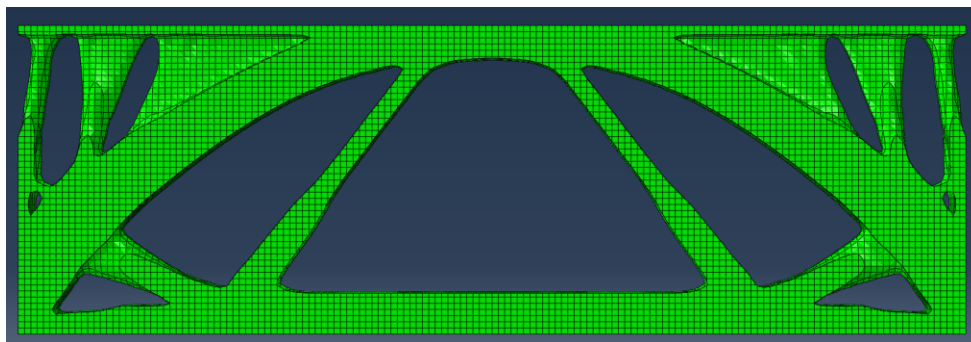
(c)
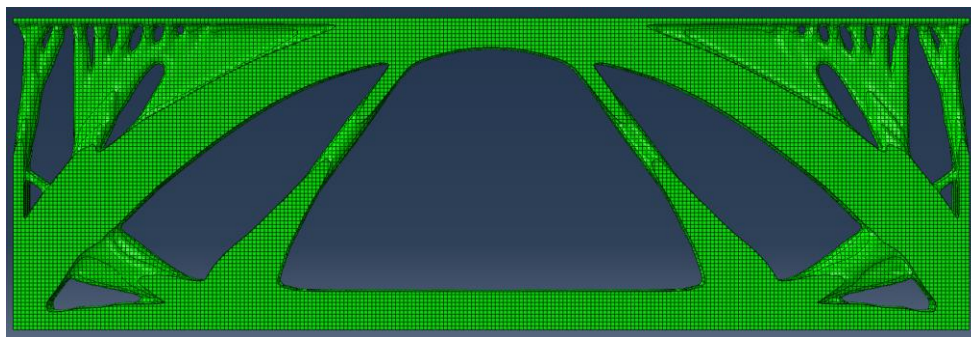
(d)

Figure 50 – Optimization outcomes in Y-Z plane. (a) 90 mm mesh size; (b) 70 mm mesh size; (c) 40 mm mesh size; (d) 25 mm mesh size

The optimization cycles for the beam with 40 mm of mesh size can be seen in video format, in attachment C.

Table 14 – Parameters values after the optimization, for the 40 mm mesh size

Span/beam height ratio (H/L)	Strain energy	Vertical reaction Force (kN)	Tensile stress value at mid span (MPa)	Displacement at mid span (mm)
1/3	1007142	567.00	11.45	2.14

(a)   (b)
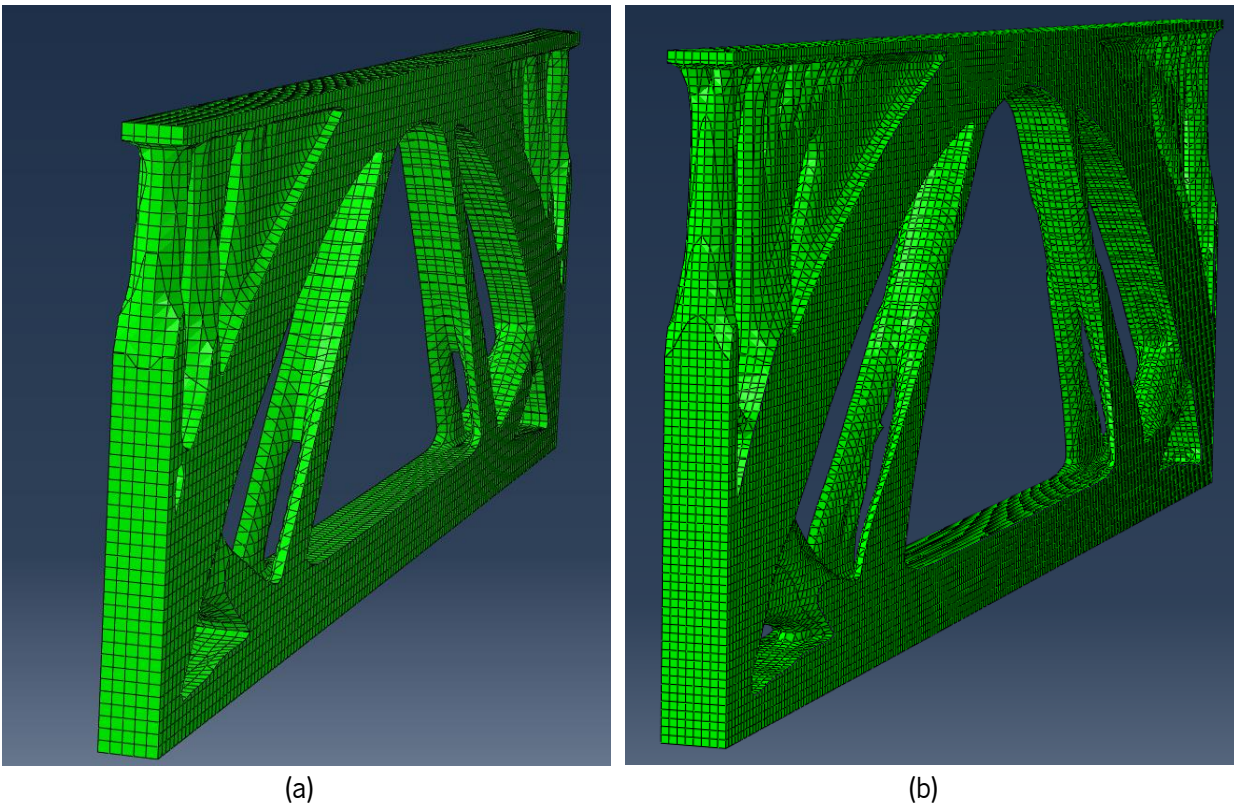
Figure 51 – Perspective of the topology optimization along the beam's width: (a) for 40 mm mesh size; (b) for 25 mm (mesh size)

As expected, for the more refined the meshes a higher computational time was required, with the mesh having the finite elements with 25 mm taking almost ten times more time to complete the same optimization process, when compared with the other refinements. When comparing the results from the 3D optimization with the ones obtained assuming a plane stress state, the optimization time also increased significantly. With that said, in terms of finding the right balance between the quality of the optimization and the computational cost, it's possible to conclude that the 70 and 40 mm meshes are the most suitable ones.

After a close look to Figure 50 and Figure 51 it can be noted that, for the more refined meshes (i.e. 40 and 25 mm), the algorithm, in addition to optimizing in the main plane (Y-Z), also performs an optimization of the cross section in depth (in the X-Y plane). The latter is an advantage, when compared to the plane stress optimizations, since for 2D modelling the algorithm only optimizes in the main plane (Y-Z). Therefore, in 3D optimization processes, it is possible to achieve a higher degree of optimization

The optimization cycles for the beam with 40 mm of mesh size can be seen in video format, in attachment C.

Table 14 shows the strain energy, stress and displacement values for the 40 mm mesh size and, comparing to Table 10, where the counterpart results for a plane stress analysis are presented, it is observed that the values are very close to each other, becoming possible to conclude that the plane stress assumption were correctly applied. Moreover, there was a reduction on the strain energy and maximum deflection at the mid-span, however it was marginal, i.e. lower than 1%. This reduction is ascribed to the optimization along the beam's X axis that can allow the allocation of material in regions that have a higher contribution longitudinal stiffness of the beam.

5. NONLINEAR BEHAVIOR OF FIBER REINFORCED CONCRETE OPTIMIZED STRUCTURES

5.1 Introduction

In the present chapter will be carried out non-linear simulations for one of the structures that was topological optimized in section 4.5. The selected beam was the one with a 0.6 m height. The geometry supports and loading conditions are shown in Figure 52.
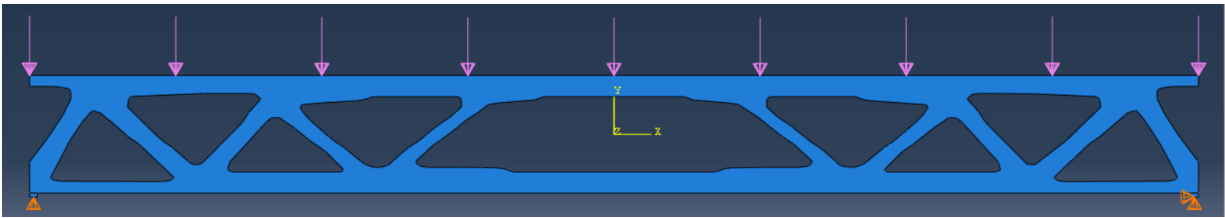
Figure 52– Geometry, support and load conditions to be applied

The objective is to compare structural behavior of the beam for different strength classes of fiber-reinforced concrete (FRC) materials. The goal is to assess the influence of distinct material properties that represent three types of behavior, namely softening, hardening and hardening-softening behavior (i.e. corresponding to the usage of low to high fiber contents). The characterization of the tensile – strain relationship for the selected FRC materials will be done according to the proposal of the fib Model Code 2010 (FIB, 2010).

For non-linear Finite Element analysis, the material constitutive model can play an essential role in predicting the strength of the concrete, so in order to conduct an appropriated analysis, the concrete damage plasticity (CDP), available in Abaqus/CAE, will be used, because it accordingly to the available literature can correctly predict the tensile and compressive behavior of concrete structures (Abrishambaf et al., 2015; Hafezolghorani et al., 2017; Shobeiri & Ahmadi-Nedushan, 2019). The material constitutive model and the characterization of the FRC materials will be further explained in sections 5.2 and 5.3, respectively.

5.2 Concrete constitutive model

For the concrete constitutive model it was used the damage plasticity (CDP) model in Abaqus. This model uses concepts of isotropic damaged elasticity in association with isotropic tensile and compressive plasticity to simulate the inelastic behavior of concrete. Both tensile and compressive crushing are included in this model. Beyond the failure stress in tension, the formation of micro-cracks is represented macroscopically with a softening stress-strain response. The post-failure behavior is modeled by using the tension stiffening diagram (SIMULIA Abaqus manual 6.14).

In general, the flow potential surface and the yield surface make use of the principal stresses (S_1, S_2, S_3) or the stress invariants (J_1, J_2, J_3). The yield function defines a surface in the effective stress space in order to represent the states of failure or damage and is represented in Figure 53.
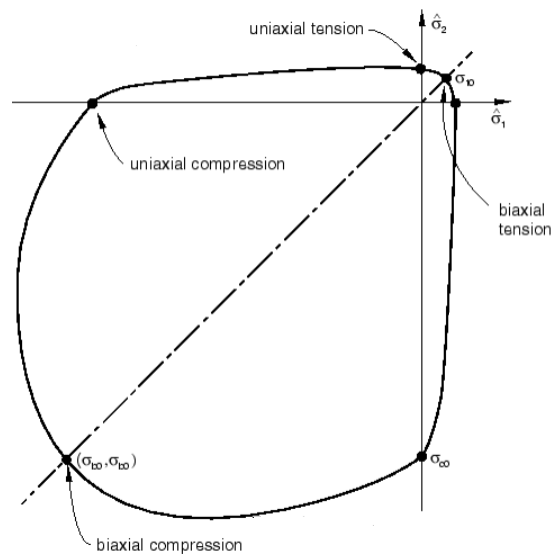
Figure 53 – Yield surface in plane stress (SIMULIA Abaqus manual 6.14).

Briefly, the potential flow and yield function are defined with four parameters:

- The dilation angle (ψ) which is simulated as concrete's internal friction angles and usually varies between 34 and 43°;

- The eccentricity (e), which represents the eccentricity of the potential plastic surface and can be determined by the ratio between the uniaxial tensile strength (σ_{t0}) and compressive strength (σ_{c0});

- The ratio between the initial biaxial compressive strength and the initial uniaxial compressive strength (σ_{b0}/σ_{c0});

- (k_c) parameter, that defines the initial yield surface and is physically assumed as a ratio of the distances between, respectively, the compressive meridian and the tensile meridian with hydrostatic axis in the deviatoric cross section.

Figure 54 shows the model tab in the graphical interface of the Abaqus software to input the aforementioned parameters

Figure 54 – Definition of the yield surface in Abaqus/CAE

Table 15 includes the constitutive parameters values for defining the yield surface of the CDP Abaqus model, which will be adopted in the present work, in order to simulate the concrete behavior during the nonlinear analysis. The parameters included in Table 15 were obtained from the literature and have proven to provide accurate simulation of the concrete behavior for both plain and fiber reinforced concrete (Abrishambaf et al., 2015; Hafezolghorani et al., 2017; Shobeiri & Ahmadi-Nedushan, 2019).

Table 15 – The Constitutive parameters values of CDP model

dilation angle (ψ)	eccentricity (e)	σ_{b0}/σ_{c0}	k_c
40	0.1	1.16	0.667

For a more detailed explanation of the potential flow and yield function, care to consult section 26.6.3 in (SIMULIA Abaqus manual 6.14).

The CDP model describes the uniaxial tensile and compressive response by characterizing the damaged plasticity behavior as shown in Figure 55.

$$\text{(a)} \qquad\qquad\qquad\qquad \text{(b)}$$
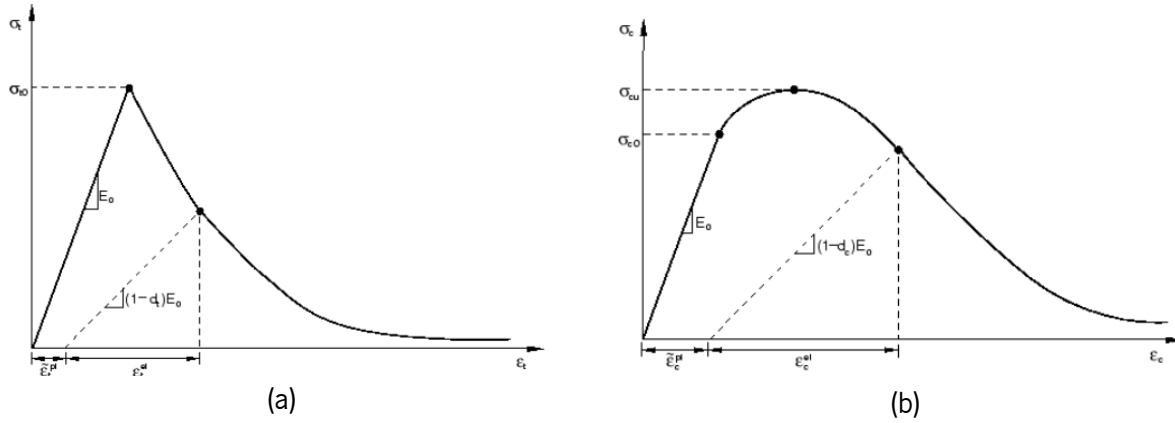
Figure 55 – Material law under uniaxial loading in: (a) tension; (b) compression.

After a close look of Figure 55, under uniaxial tension (Figure 55a) the stress-strain response follows a linear elastic relationship until the value of the failure stress, σ_{t0}, is reached. The failure stress corresponds to the onset of micro-cracking in the concrete. Beyond this failure stress, it is observed the formation of a macro-crack, which is represented macroscopically with a softening stress-strain response that induces strain localization in in the concrete structure. Under uniaxial, compression (Figure 55b), the response is linear until the value of the initial yield, σ_{c0}. After reaching that value the response enters in a plastic domain, where is typically characterized by stress hardening followed by strain softening beyond the ultimate stress, σ_{cu}.

It can also be concluded from Figure 55, that when the concrete is unloaded from any point of strain softening regime of the stress-strain curve, the unloading response is weakened, the elastic stiffness of the material is damaged. This reduced elastic stiffness is computed through applying a reduction factor to the undamaged stiffness. In this case, the strain after unloading, does not return to zero, but some residual stresses remain present which is similar to the real behavior of concrete (SIMULIA Abaqus manual 6.14).

In the CDP model, the elastic stiffness is characterized by two damage variables, d_t and d_c, which are functions of plastic strains (ε_c^{pl} and ε_t^{pl}: equivalent plastic strain, $\dot{\varepsilon}_c^{pl}$ and $\dot{\varepsilon}_t^{pl}$: equivalent plastic strain rate). These two damage variables can take values from zero to one, where zero represents the undamaged material and one represents the total damaged material (total loss of the strength). Therefore, when E_0 is

the initial undamaged elastic stiffness, the stress-strain relations under uniaxial tension and compression loading are respectively calculated as:

$$\sigma_t = (1 - d_t)E_0(\varepsilon_t - \varepsilon_t^{pl})$$

$$\sigma_c = (1 - d_c)E_0(\varepsilon_c - \varepsilon_c^{pl})$$

5.3 Characterization of the fibre-reinforced concrete (FRC) materials

Fiber-reinforced concrete (FRC) is a composite material characterized by a cementitious matrix and discrete fibres (discontinuous). The matrix is made of either concrete or mortar. Fibers can be made of distinct materials, such as steel, polymers, carbon, glass or natural materials. Structural design of FRC elements is based on the post-cracking behavior and the residual strength provided by fiber reinforcement. Fibers can be used to improve the behavior at Serviceability Limit States (SLS) enhancing the durability, by reducing the crack spacing and width. Moreover, they can be used, to substitute partially or totally conventional reinforcement depending on the application and the FRC mechanical properties, hence improving the behavior at ULS.

By adding fibres to the cementitious matrix, the mechanical properties regarding the post-cracking behavior are significantly affected, however, elastic properties and compressive strength are not significantly affected by fibers, unless a very high volumetric ratio is used (FIB, 2010). Having the latter in mind, the compressive behavior for the all the FRC will be assumed as perfectly plastic in and initial stage, with a compressive strength of 60 MPa, as shown in Figure 56. During preliminary analyses, the compressive stresses level and eventual plastic strains will be checked, in order to check if the material is in the elastic or in a plastic stage.
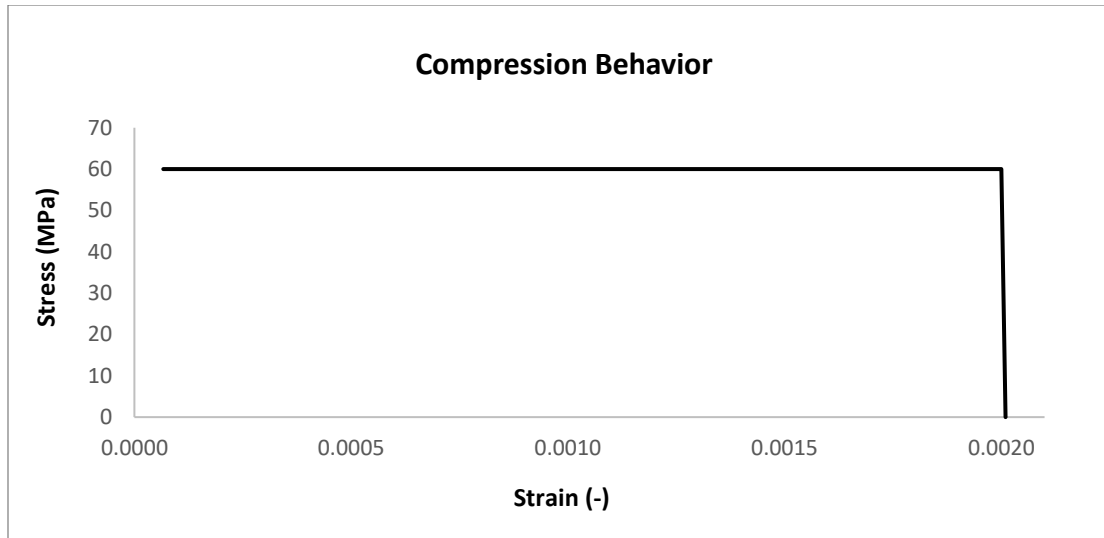
Figure 56 – Compressive behavior of the three materials

Depending on their composition, FRC materials can mainly show two types of behavior under uniaxial tension: softening and hardening (FIB, 2010). As stated in section 5.1 the goal of this chapter is to simulate, in Abaqus/CAE, distinct types of behaviors corresponding to FRC with distinct strength classes. Initially, it will be done the characterization of the material law under tension adopting the simplified models proposed by Model Code 2010 for the Ultimate Limit State (ULS). Afterwards, the tensile law proposed for Serviceability Limit State (SLS), which comprises more branches for modeling the initial cracking stage will be adopted.

5.3.1 Classification of the FRC materials

According to section 5.6.3 section of Model Code 2010, the classification of the materials is done according with two parameters: f_{R1k} (representing the strength interval) and a letter (representing the f_{R1k}/f_{R3k} ratio), where f_{R1k} and f_{R3k} are the characteristic flexural residual strength for serviceability and ultimate conditions, respectively. Table 16 shows the classification that was assigned to the different FRC materials after definition of the f_{R1k} and f_{R3k} values.

Table 16 – Strength class and residual strength parameters of the adopted FRC

Strength Class	Behavior	f_{R1k} (MPa)	f_{R1k}/f_{R3k} ratio	f_{R3k} (MPa)
3a	Softening	3	0.5	1.5
3c	Softening /Rigid plastic	3	1.0	3
3e	Softening / Hardening	3	1.5	4.5
12a	Hardening / Softening	12	0.5	6
12c	Softening / Rigid plastic	12	1.0	12
12e	Hardening / Hardening	12	1.5	18

5.3.2 Stress-crack width diagram according simplified laws for ULS

The nonlinear analysis performed with the laws derived on the simplified model for the ULS will be based on with a FRC with relatively low residual strength (f_{R1k} = 3 MPa). According to sections 5.6.5 of Model Code 2010, for the ULS the simplified constitutive laws presented in Figure 57 may be applied. However, the same recommendation states that in the case of using numerical analysis for designing FRC structures, more complex and detailed constitutive laws should be used.

As explained in 5.6.4 in FIB Model Code 2010, for the Rigid-plastic model, $f_{Ftu} = f_{R3k}/3$. For the softening and hardening models $f_{Fts} = 0.45f_{R1k}$ and $f_{Ftu} = f_{Fts} - \frac{w_u}{CMOD_3}(f_{Fts} - 0.5f_{R3k} + 0.2f_{R1k}) \geq 0$ (see Figure 58). Where f_{Fts} represents the serviceability residual strength, defined as the post-cracking strength for serviceability crack openings, and f_{Ftu} represents the ultimate residual strength. w_u is the maximum crack opening accepted in structural design and it's given by $l_{cs} * \varepsilon_{Fu}$, where l_{cs} is the corresponding structural characteristic length (will be assumed the mesh refinement value) and, ε_{Fu} is the ultimate crack strain, being recommended to use the value of 2% in the case where the crack opening / strain varies along the cross section, such is the case of a beam under flexure.
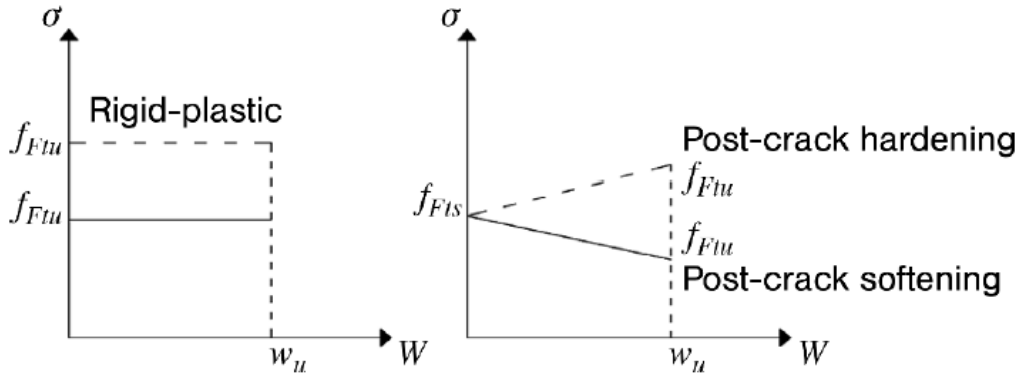
Figure 57 – Simplified post-cracking constitutive laws: stress-crack opening (continuous and dashed line refer to softening and hardening post-cracking behavior, respectively) (FIB, 2010).

After defining the constitutive law type and residual strengths, it is possible now to calculate all the necessary parameters in order to fully characterize the constitutive laws, see (FIB, 2010). Figure 58 shows the tensile - strain relationship of the three materials.

Table 17 – Mechanical Properties of the three materials

Classification	Behavior	E (MPa)	f_{ck} (MPa)	f_{Fts} (MPa)	f_{Ftu} (MPa)	l_{cs} (mm)	ε_{Fu} (-)	w_u (mm)
3a	Softening	39100	60	1.35	0.966	40	0.02	0.8
3c	Softening/ Rigid plastic	39100	60	-	1.00	40	0.02	0.8
3e	Softening / Hardening	39100	60	1.35	1.446	40	0.02	0.8

f_{ck}* Compressive strength
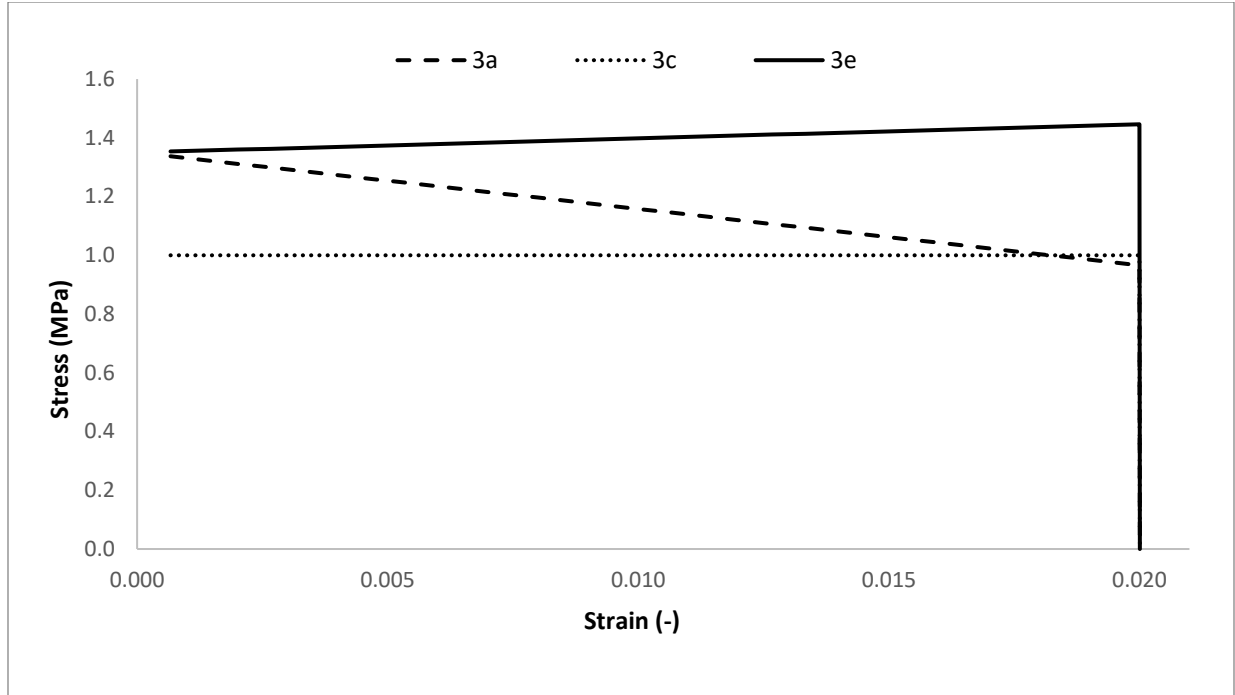
Figure 58 – Tensile -strain relationship for the three FRCs.

5.3.3 Stress-crack width diagram according laws proposed for SLS

Additionally, stress – strain relationships were also defined based on the recommendations of Model Code 2010 for SLS. In this case FRCs with distinct class strengths were adopted, corresponding to low and high volumetric fiber contents (i. e. f_{R1k} = 3 MPa and f_{R1k} = 12 MPa). According to Model Code 2010 for SLS the laws shown in Figure 59 should be used.
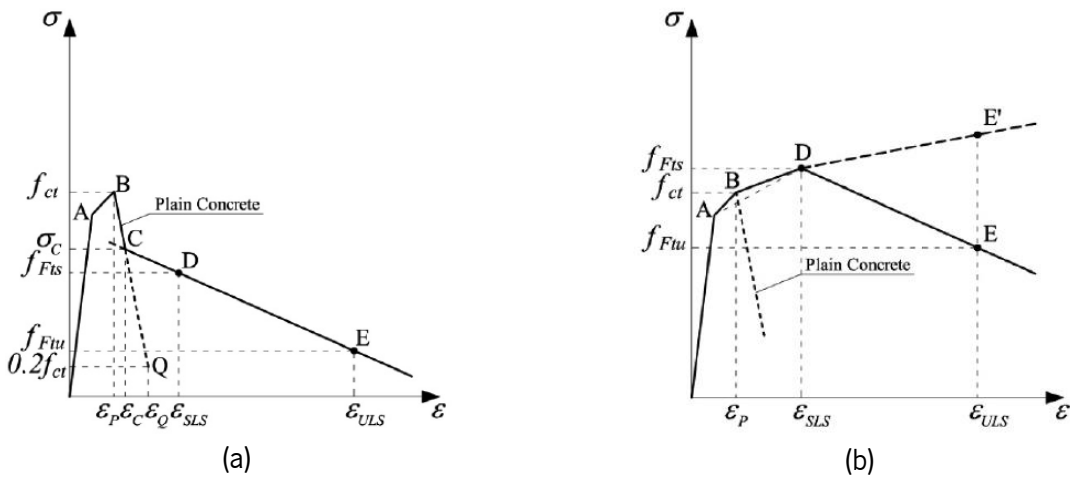
Figure 59 – Constitutive laws at SLS. (a) for $f_{Fts} < f_{ct}$ and (b) for $f_{Fts} \geq f_{ct}$

For the materials with f_{R1k} = 3 MPa the law shown in Figure 59a will be used, on the other hand for the FRCs with f_{R1k} = 12 MPa it will be used the law shown in Figure 59b. The branches OA and AB are the same for both laws. The concrete was assumed as C60, therefore f_{ct}, which is the tensile strength is equal to 4.4 MPa. Point A and ε_p are described in section 5.1.8.2 of Model Code 2010 (FIB, 2010). The calculation of branch DE for both laws is done according to the explanation presented in section 5.3.2.

Point C presented in figure Figure 59a corresponds to the intersection of BQ with DE, where BQ is given by:

$\frac{\sigma - f_{ct}}{0.2f_{ct} - f_{ct}} = \frac{\varepsilon - \varepsilon_p}{\varepsilon_Q - \varepsilon_p}$ with $\varepsilon_Q = \frac{G_F}{f_{ct}*l_{cs}} + \left(\varepsilon_p - \frac{0.8f_{ct}}{E_c}\right)$, where G_F represents the fracture energy of plain concrete and is described in section 5.1.5.2 of Model Code 2010 (FIB, 2010).

With that said is possible to calculate all the necessary parameters in order to characterize the constitutive laws, displayed in Table 18. Figure 60 shows the tensile - strain relationships for the six FRC class strengths.

Table 18 - Materials mechanical properties

Strength class	Tensile behavior in branch: (BD – DE)	E (MPa)	f_{ck} (MPa)	f_A (MPa)	f_{ct} (MPa)	σ_c (MPa)	f_{Fts} (MPa)	f_{Ftu} (MPa)
3a	Softening - Softening	39100	60	3.96	4.4	1.96	1.35	0.966
3c	Softening - Rigid plastic	39100	60	3.96	4.4	1.00	1.00	1.00
3e	Softening - Hardening	39100	60	3.96	4.4	1.20	1.35	1.446
12a	Hardening – Softening	39100	60	3.96	4.4	-	5.40	3.864
12c	Softening – Rigid plastic	39100	60	3.96	4.4	-	4.00	4.00
12e	Hardening - Hardening	39100	60	3.96	4.4	-	5.40	5.784

f_{ck}* Compressive strength
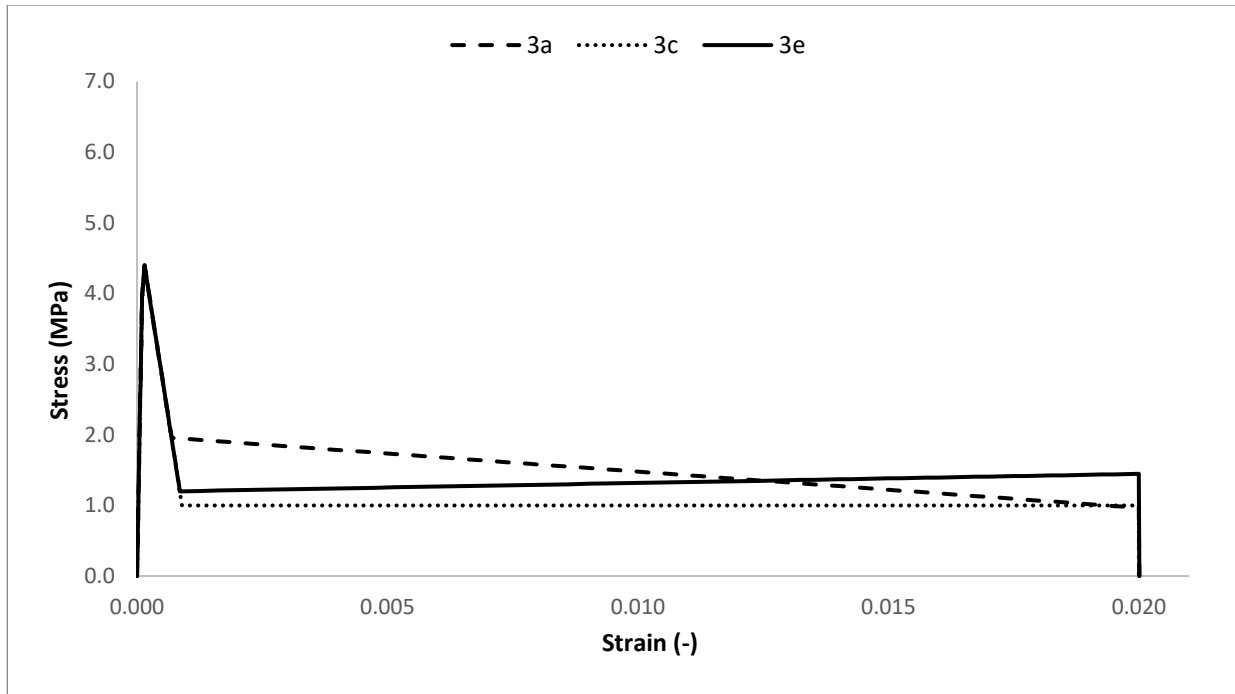
(a)
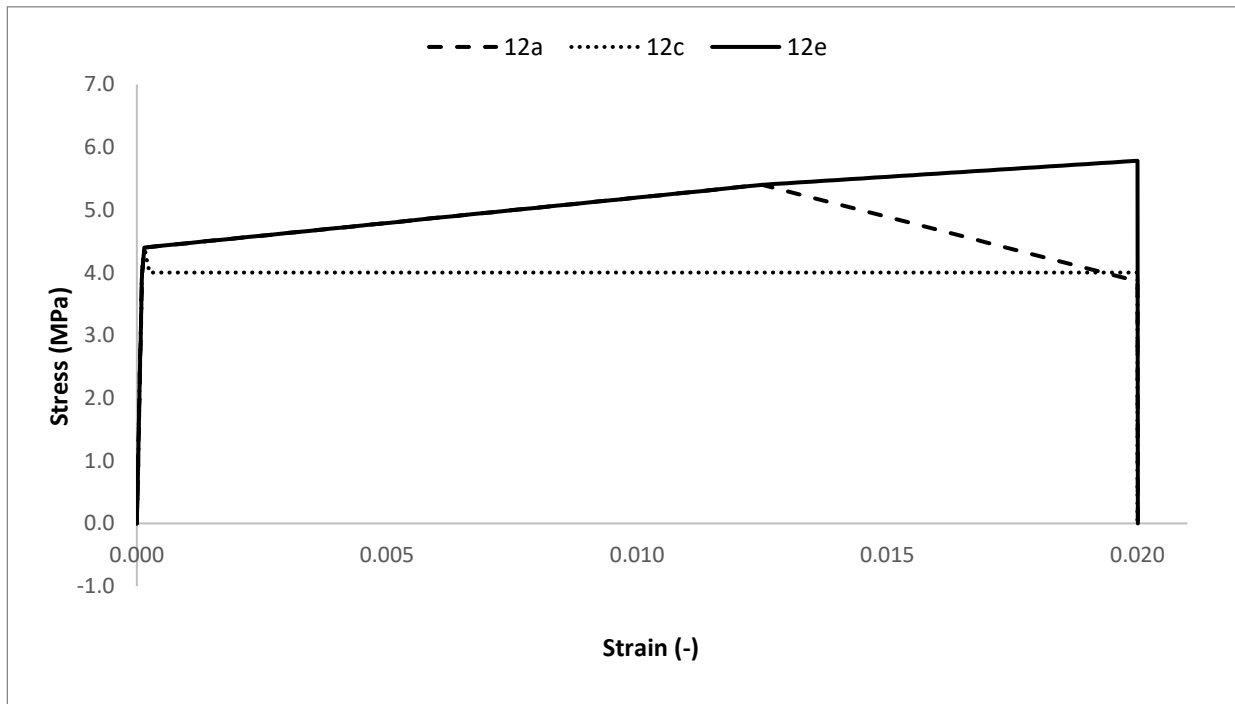
(b)

Figure 60 – Stress / strain behavior for the materials presented in Table 18. (a) 3a, 3c, 3e and (b) 12a, 12c, 12e.

5.4 Structural response of the optimized FRC beam

In this section the nonlinear simulations will be carried out using the constitutive laws defined in the previous sections. As stated before, the mesh refinement will be the same used before (CPS4 elements with 4 nodes and 40 mm of length), as shown in Figure 36. The results obtaining the laws proposed by Model Code 2010 for both ULS and SLS are displayed in the following sections.

5.4.1 Results with the constitutive laws for ULS

In this section, the results regarding the FRC beam's mechanical behavior with the constitutive laws obtained in section 5.3.2 will be presented. The deformed geometries for the three constitutive laws are displayed in Figure 61.

(a)

(b)

(c)
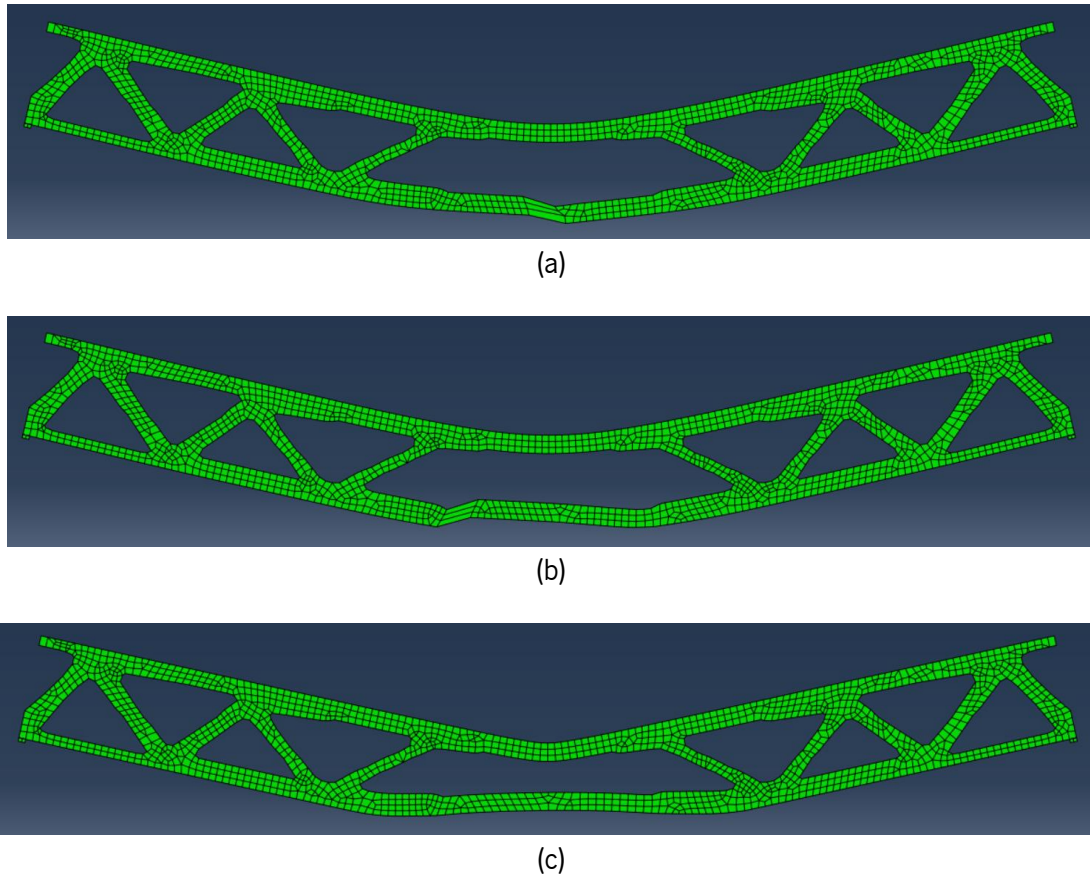
Figure 61 – Deformed geometries for the three behaviors. (a) softening (3a); (b) softening / rigid plastic (3c); (c) hardening (3e)

Through the analysis of Figure 62, it is possible to conclude that both softening and softening / rigid plastic behaviors had similar rupture modes as it will discussed in more detail further ahead. The stress / plastic strain and force / deflection curves obtained in Abaqus/CAE are displayed Figure 62 and Figure 63, respectively. Note that the stress – strain diagram was obtained at the integration point that exhibited the highest strain value, on the other hand, the force was computed has the vertical resultant of the supports and the deflection at the point that showed the highest vertical displacement. Therefore, the deflection was assessed at distinct locations depending on the localization of the inelastic deformations, i.e. cracks.

After a close look to the results displayed in Figure 62, regarding the stress – strain relationship assessed at the integration point, it is possible to state that they are very similar to the ones displayed in Figure 58, which leads to the conclusion that and the constitutive laws were correctly implemented in the Abaqus/CAE software.

Figure 62 - Stress / strain relationships for the three FRCs

(a)

(b)

Figure 63 – Stress / strain and force / deflection curves. (a) stress / strain relationships for the three FRCs; (b) force/deflection behavior for the softening and rigid plastic materials; (c) force/deflection behavior for the hardening material.
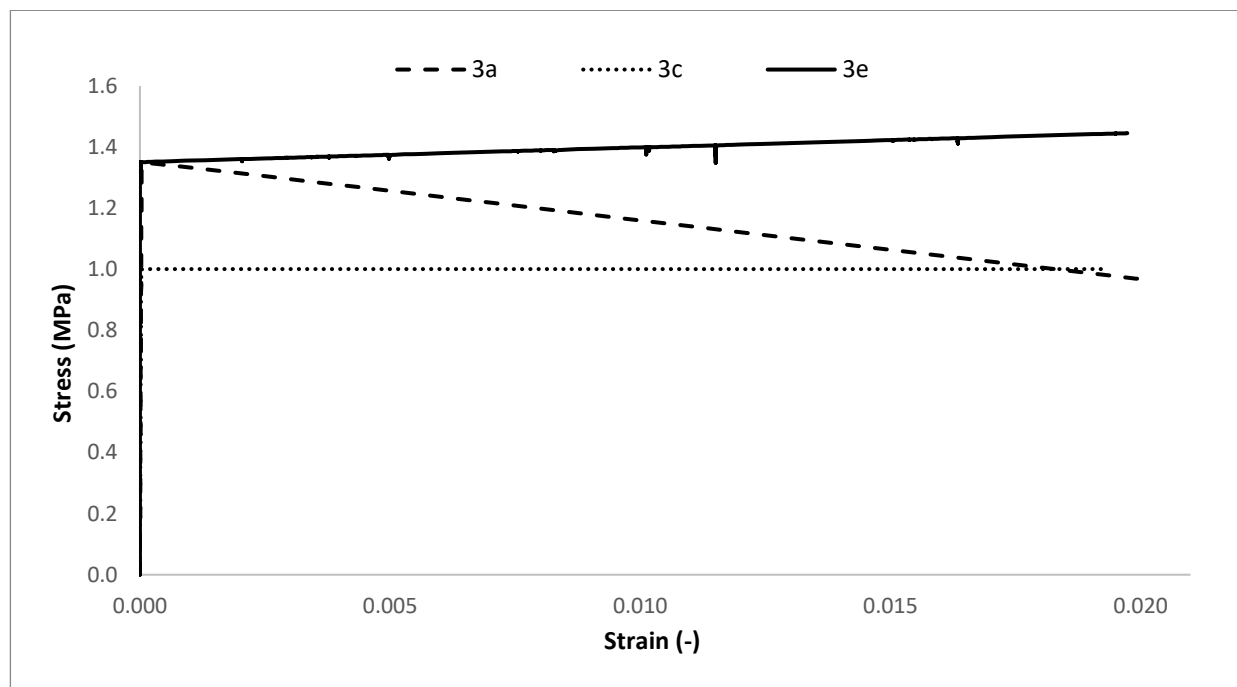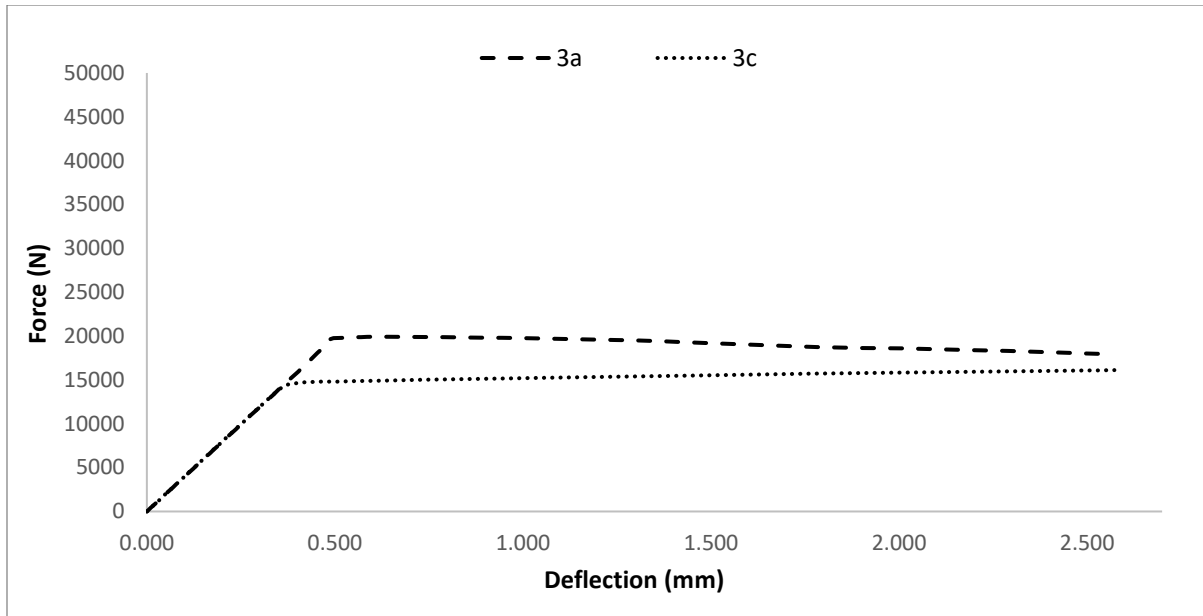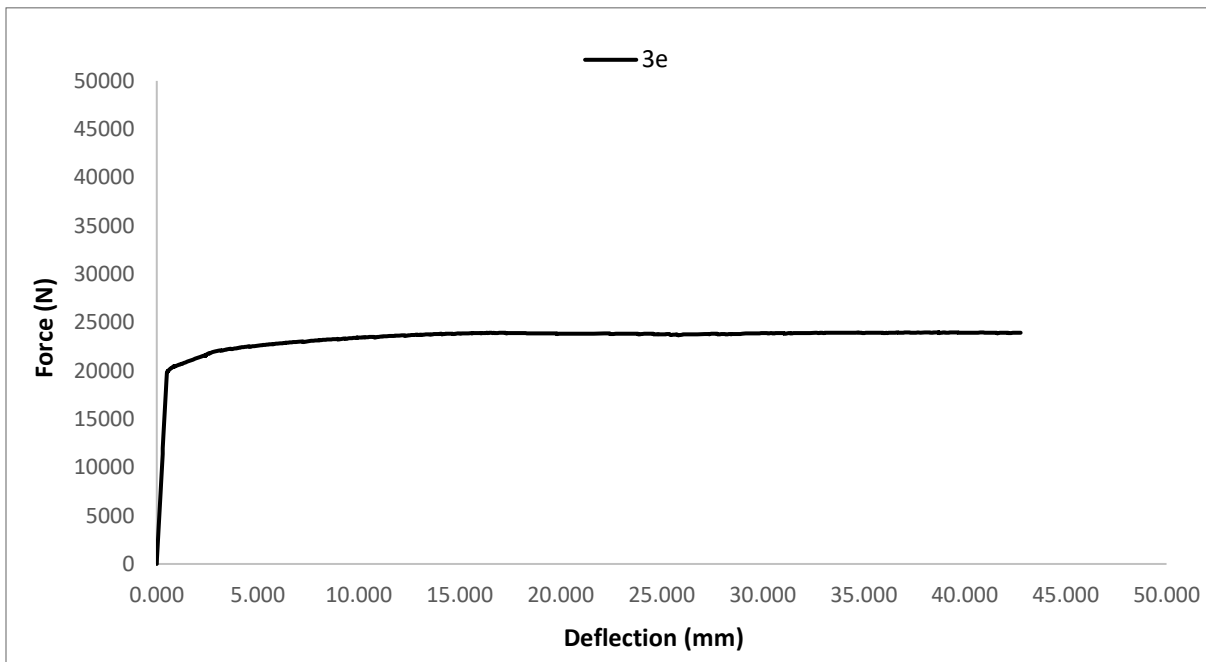
Figure 63a shows the force / deflection, for both softening and softening / rigid plastic materials, where it is possible to see that the structure with the rigid plastic material assign, after reaching the 0.35 mm of deflection for a load of 15 kN enters in the plastic domain, reaching the maximum strain (2%) for a 16.7 kN load. On the other hand, the structure with the class strength 3a, since it has an initial yield strength superior than the rigid plastic law, enters in the plastic domain for a load superior, of approximately 20 kN with a deflection of 0.5 mm. Afterwards due to its softening behavior reaches the maximum strain (2%) for a lower load of 17.2 kN, being very close to the 16.7 kN load characterized by the rigid plastic behavior. Figure 63b shows the force / deflection at mid span for the hardening material, where the structure reaches the plastic domain at the same point of the softening material, hardening branch in the constitutive law, the structure keeps holding the load up to an maximum of approximately 24.5 kN with a deflection considerably higher, i.e. of 40 mm. Therefore, in this case hardening in the post-peak stage enabled a considerable stress redistribution capacity contributing to the increase of the ultimate load capacity and toughness.

 Figure 64 and Figure 65 shows the appearance of the principal plastic strains according to the load level, respectively on the onset of cracking and at the last converged iteration, where it is possible to see that, for both softening and softening / rigid plastic relationships only the element that first reached the yield stress was plasticized, in other words there is the localization of the macro-crack in one specific location. On the contrary, in the structure which was assigned the hardening material relationship, since it has a higher capability of redistributing the stresses, practically all the center part of the lower flange was plasticized.

(a)

(b)
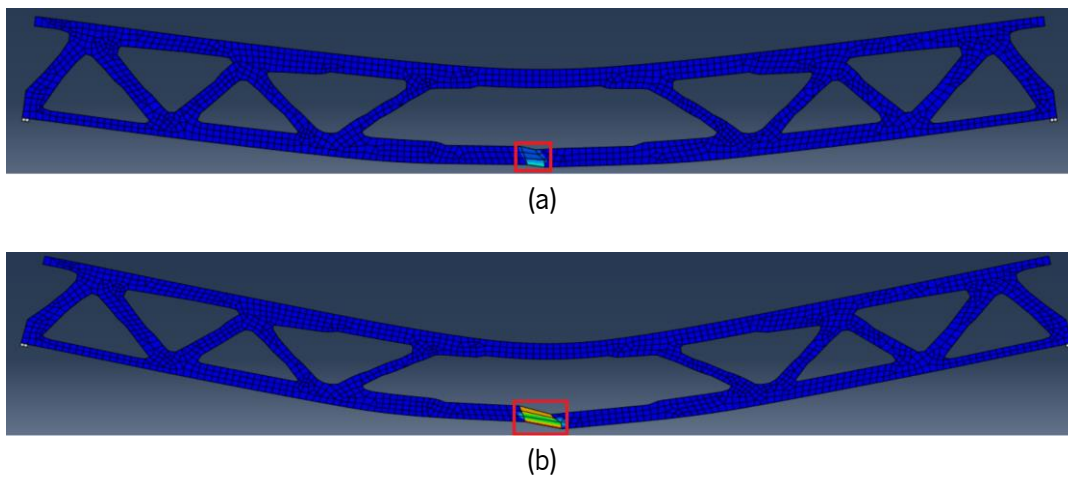
Figure 64 – Plastic strain according to the load level: (a) and (b) principal plastic strains at the onset of cracking and for the last converged iteration, respectively, strength class 3a

(a)

(b)

(c)

(d)

(e)

(f)
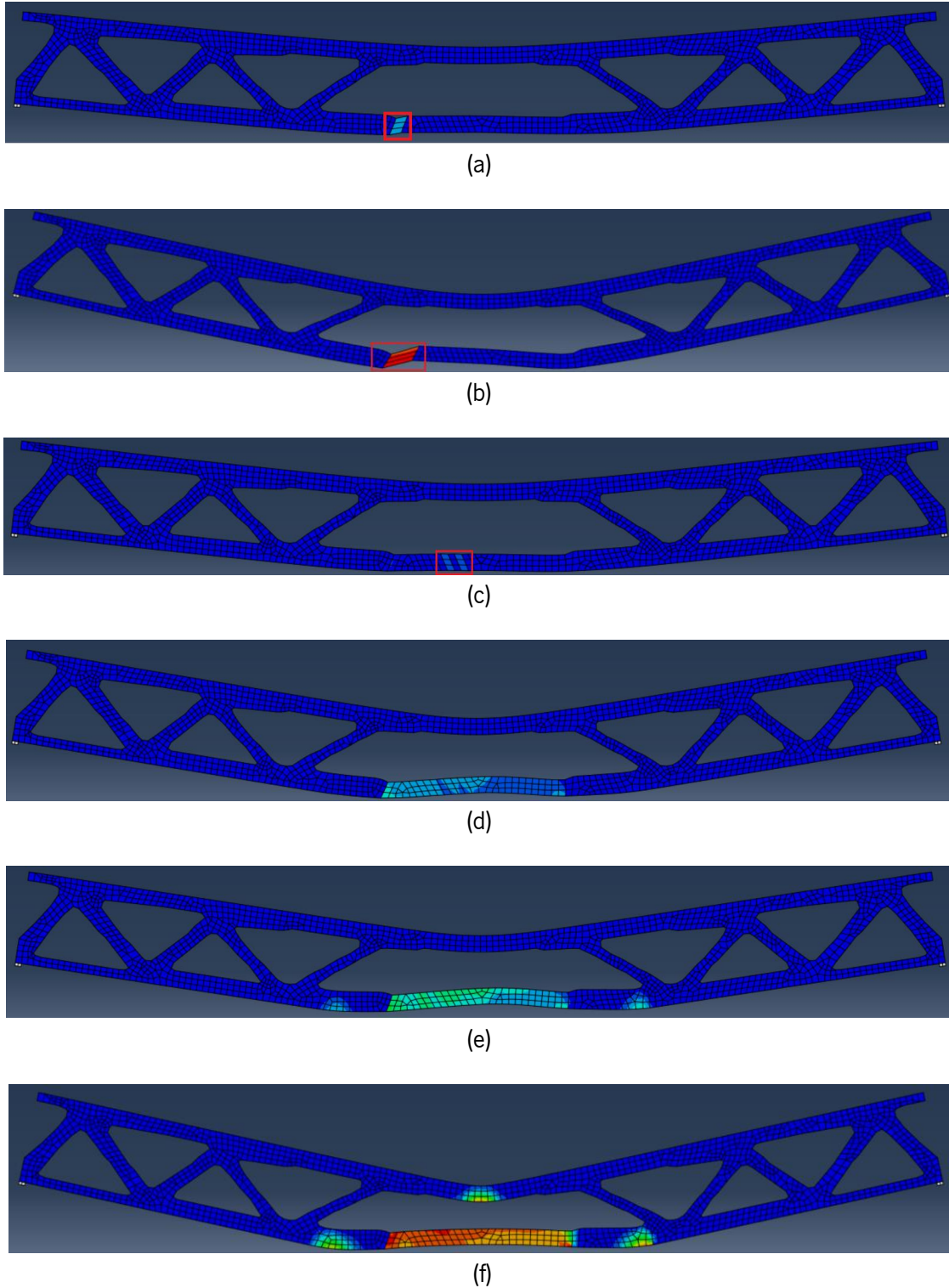
Figure 65 – (a) and (b) principal plastic strains at the onset of cracking and for the last converged iteration, respectively, strength class 3c; (c), (d), (e) and (f) principal plastic strains at the onset of cracking up to the last converged iteration, respectively, strength class 3e.

5.4.2 Results with the constitutive laws for SLS

In this section, the nonlinear analyses will be performed using the FRC constitutive laws defined in section 5.3.3. The stress / strain and force / deflection curves obtained in Abaqus/CAE. The stress – strain relationships at the integration point with the highest strain in the last converged iteration are displayed in Figure 66 and Figure 67 for the materials with low and high strength (f_{R1k} = 3 MPa and f_{R1k} = 12 MPa), respectively.
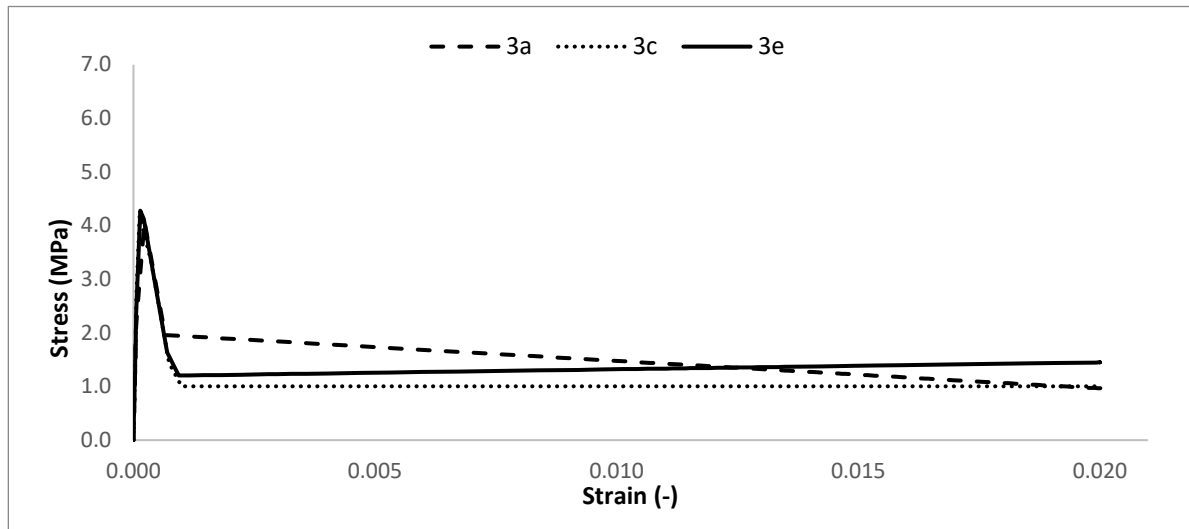
(a)
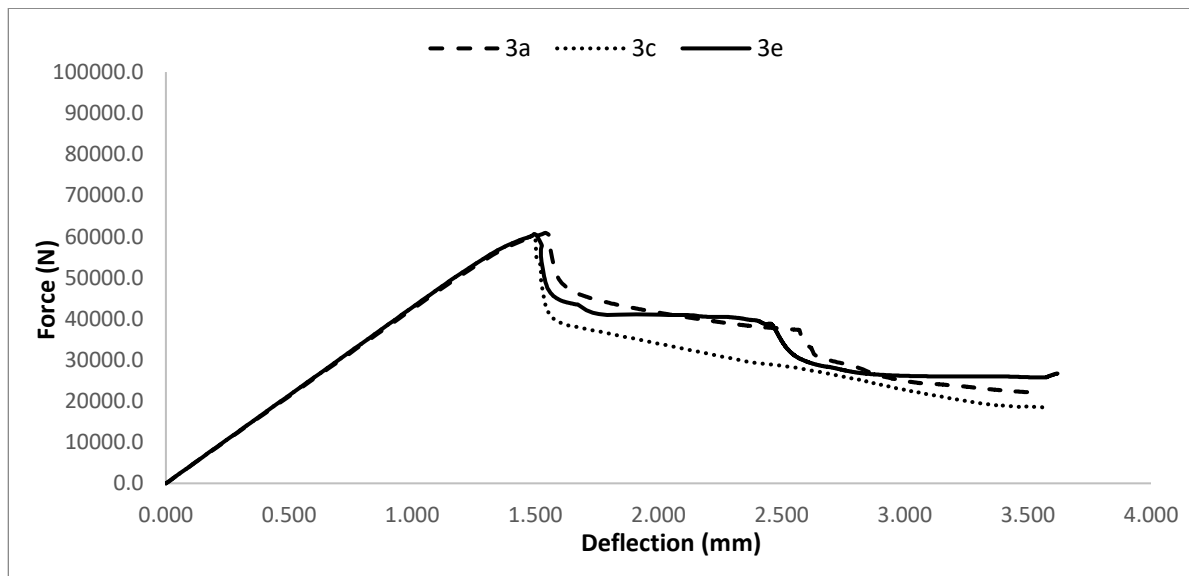
(b)

Figure 66 - Stress/strain (a) and force/deflection (b) curves for the materials with f_{R1k} = 3 MPa.
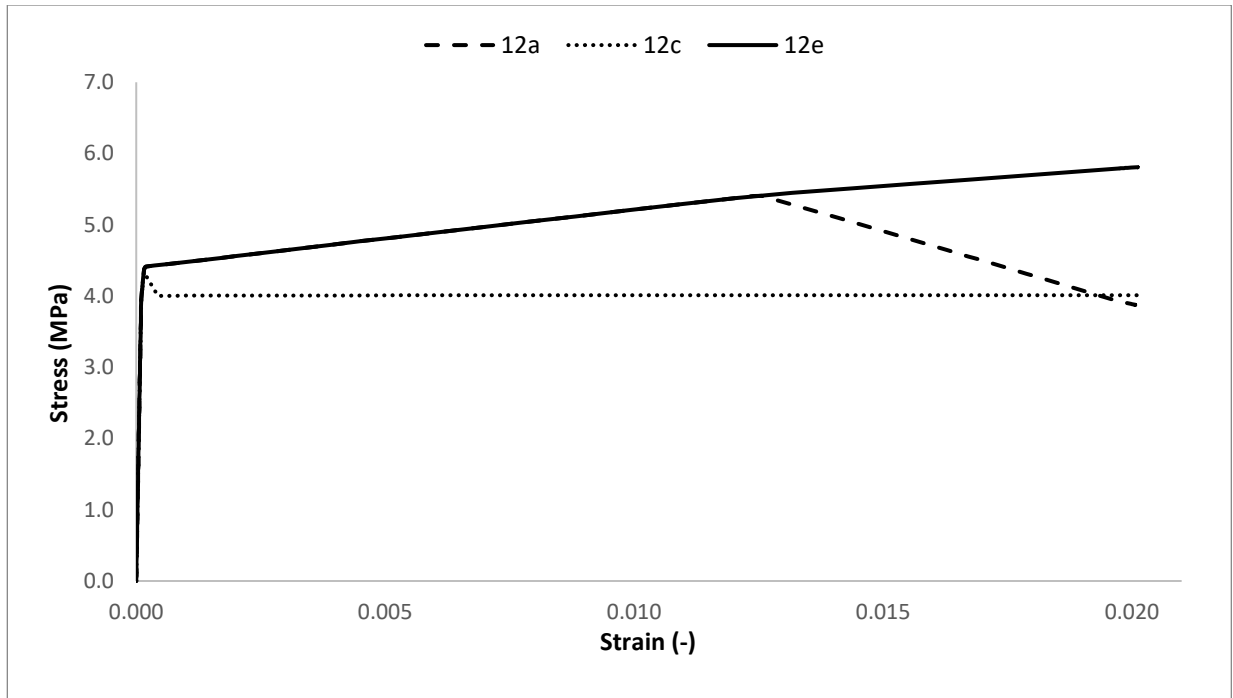
(a)
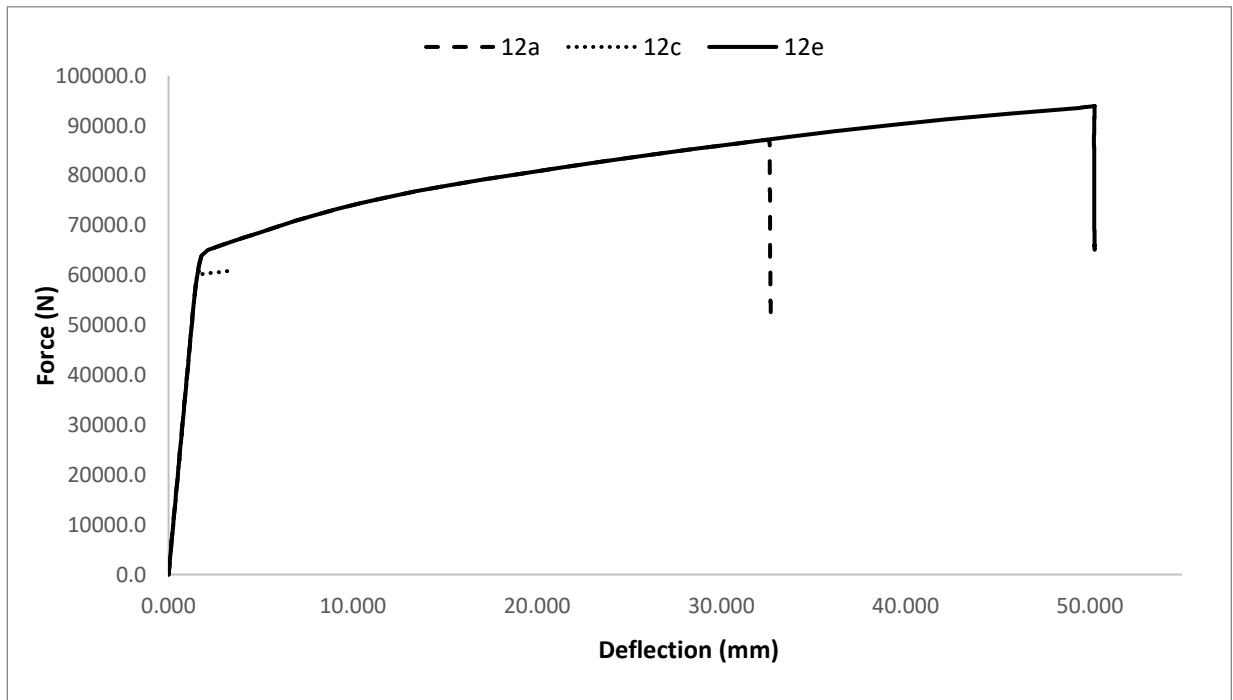
(b)

Figure 67 - (a) Stress - strain relationship and (b) force - deflection curve, for the FRCs with f_{R1k} = 12 MPa.

After a close look to the results displayed in Figure 66a and Figure 67a is possible to state that they are very similar to the ones displayed in Figure 60a Figure 60b respectively, which leads to conclude that its implementation in Abaqus/CAE was successfully carried out.

When considering the constitutive law proposed for SLS, the three structural responses with f_{R1k} = 3 MPa, corresponding to strength classes 3a, 3c and 3e have very similar behaviors. The main difference is regarding the second post-peak stage (CD and DE branches), where the FRCs with the 3a, 3c and 3e materials have, respectively a, softening, perfectly plastic and hardening behavior. Regarding the initial post-peak response (BC branch) all three FRCs have a similar behavior, characterized by an abrupt drop of the tensile strength. Consequently, this material behavior leads to a similar rupture mode on the beams modelled with the distinct strength classes (see Figure 68 and Figure 69), with the localization a single macro-crack in the bottom flange nearby a lower central tie.

As stated in Model Code 2010 (FIB, 2010), the difference between modelling using the constitutive laws proposed for ULS and SLS, is that in SLS the behavior of the structure under serviceability conditions, i.e. for lower crack opening widths and lower deformation levels is modeled more accurately. On the other hand, the simplified tensile relationship for ULS only renders good performance at the late stage of the structural response, i.e. at the failing time. This is corroborated by comparing Figure 63a and Figure 63b with Figure 66b, in which the ultimate loads before rupture is observed are very similar when using the tensile diagram obtained for ULS and SLS.

(a)

(b)

Figure 68 - Plastic strains presented in the structures. (a) and (b) Principal plastic strains and directions of the plastic strains, respectively, using the 3a material.

(a)

(b)

(c)

(d)

Figure 69 - Plastic strains presented in the structures. (a) and (b) Principal plastic strains and directions of the plastic strains, respectively, using the 3c material; (c) and (d) Principal plastic strains and directions of the plastic strains, respectively, using the 3e material.

Regarding FRCs with a higher strength class, namely by defining a $f_{R1k} = 12$ MPa, both FRCs with a strength class of 12a and 12e undergo through an initial hardening. After that, the structure with the FRC strength class 12a undergoes through rupture, for a load of 86 kN at a deflection over 30 mm (see Figure 67). On other hand, the FRC structure with the class strength 12e, the material keeps hardening before rupture up to a higher deflection level, over 50 mm, the rupture occurred for a load of approximately 94 kN (see Figure 67). Both these structures are characterized by an initial plasticizing of the central part of the bottom flange before rupture, thanks to the hardening properties assign to them. To emphasize the abovementioned, in the FRC with the strength class 12e, the structure exhibited a higher number of cracks with lower crack spacing that lead to the observed hardening and improved ductility due to the high capacity of stress redistribution (see Figure 71).

On the opposite, the latter kind of behavior was not verified in the beam with the strength class 12c. Analyzing Figure 62, Figure 63 and Figure 67 is possible to conclude that both structures with 3c and 12c materials assign have a very similar behavior, where the main difference is that the structure with 12c material endured a load of 60 kN, approximately three times bigger than the structure with the 3c material. This affirmation is also corroborated by looking to the rupture modules of both beams, where by comparing Figure 65b and Figure 70 is possible to see that they are very similar to each other.
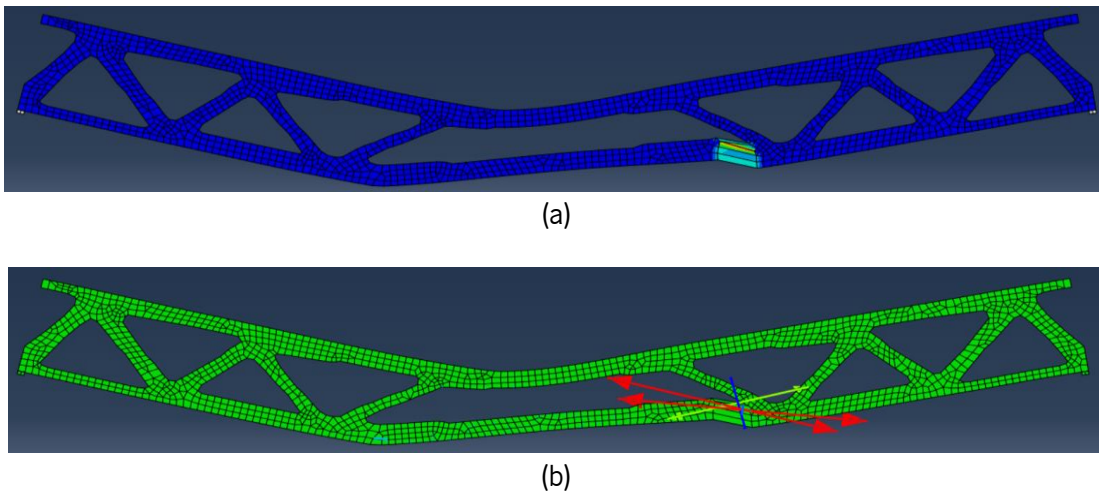

(c)

(d)
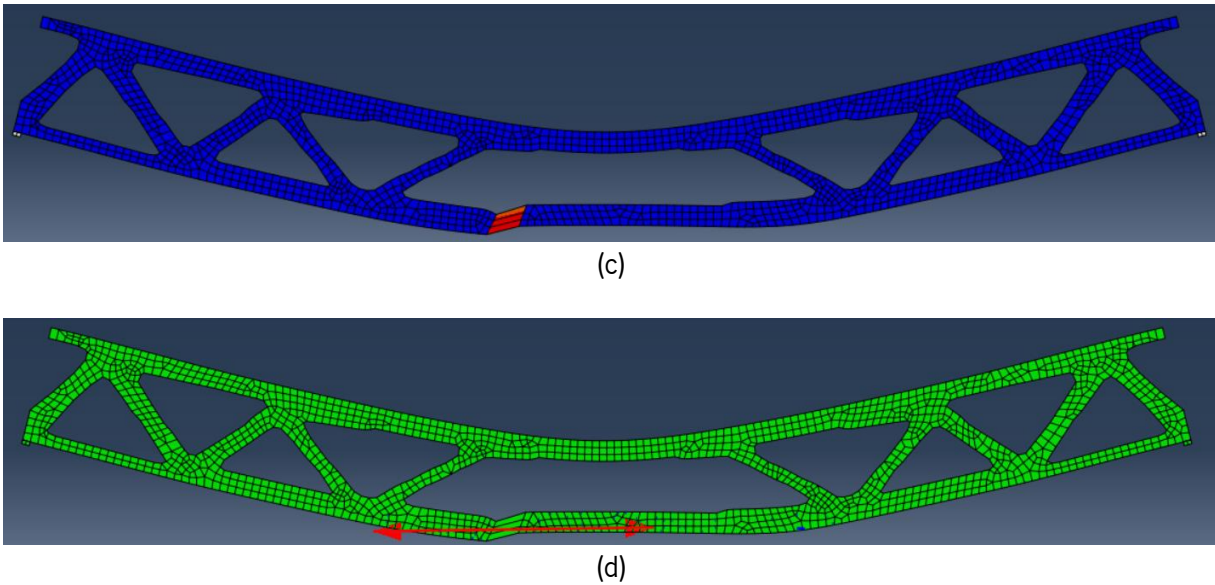
Figure 70 - Plastic strains presented in the structures. (a) and (b) Principal plastic strains and directions of the plastic strains, respectively, using the 12c material.
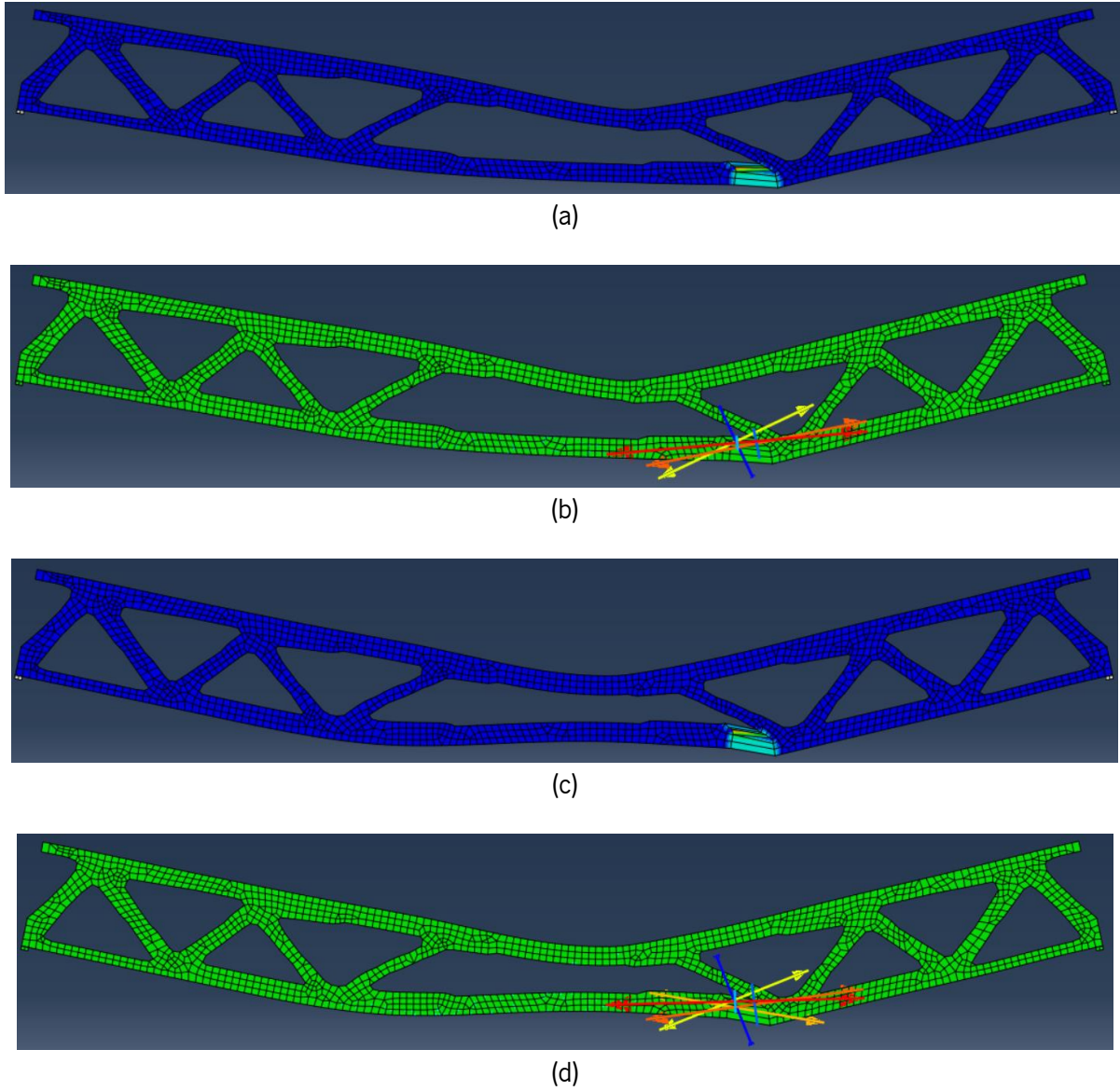
(a)

(b)

(c)

(d)
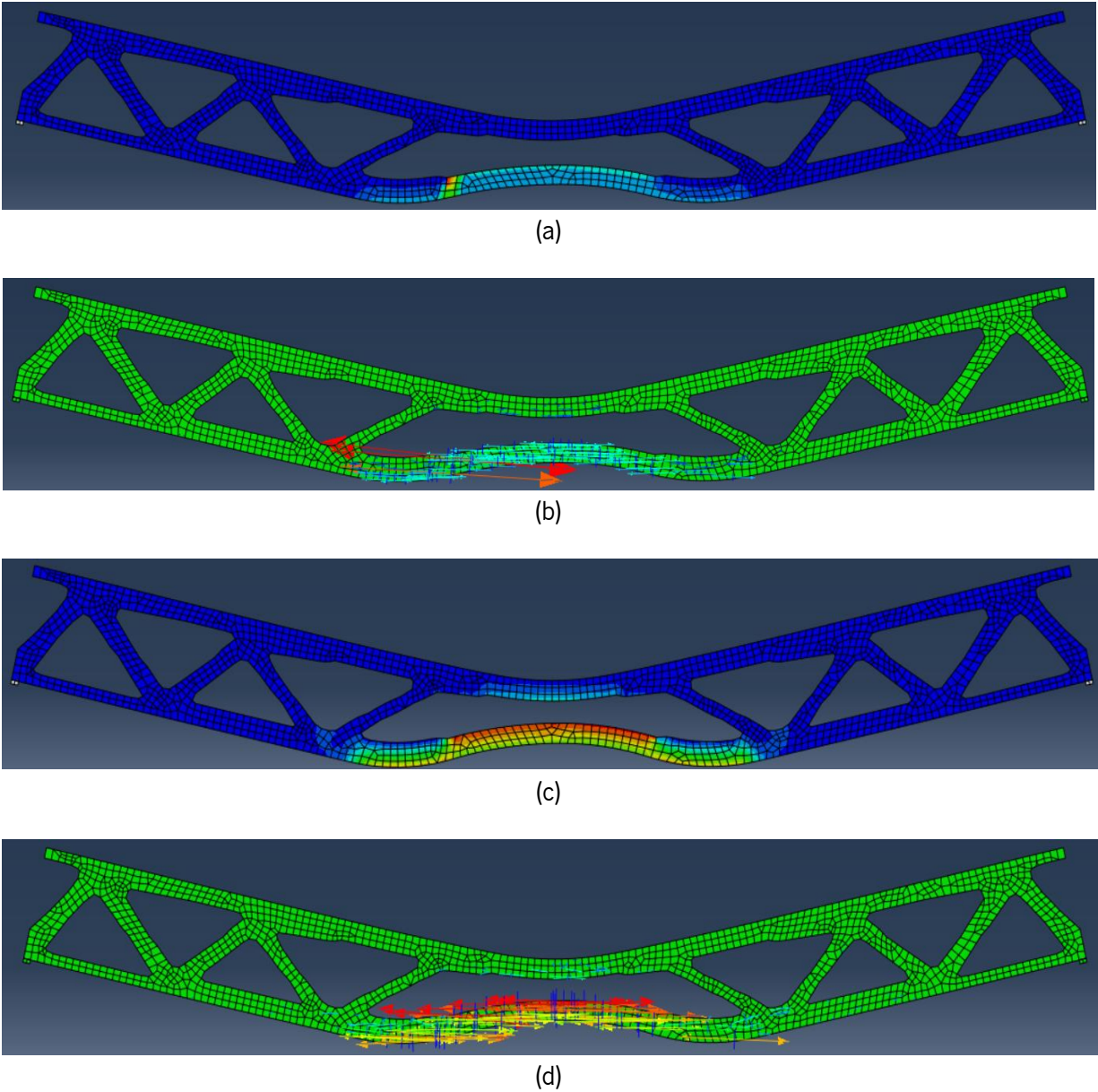
Figure 71 - Plastic strains presented in the structures. (a) and (b) Principal plastic strains and directions of the plastic strains, respectively, using the 12a material; (c) and (d) Principal plastic strains and directions of the plastic strains, respectively, using the 12e material.

A simulation for the structures with the materials of strength class 12 can be seen in video format, in attachment D.

5.5 Post structural optimization 3D Printing methodology

In this section a summarized explanation about the path to be followed in order to obtain to 3D model of the optimized structure, through 3D printing, will be made. After obtaining the optimization outcome, Abaqus/CAE offers the capabilities to export it, to STL format, as orphan mesh, as shown in Figure 72.
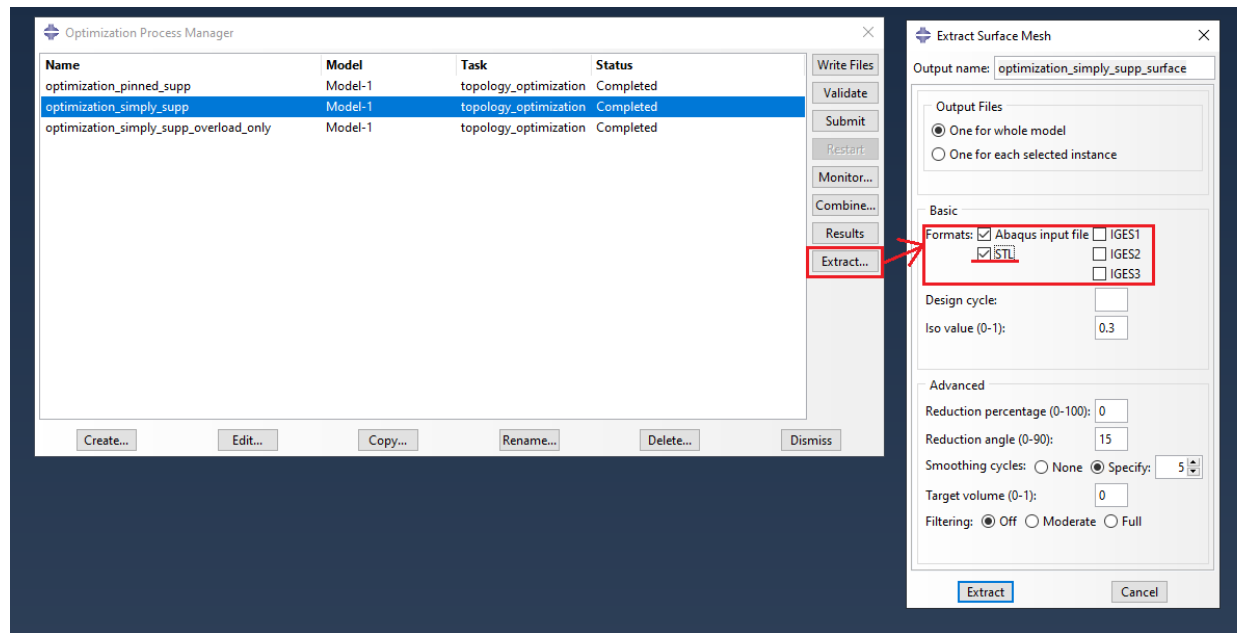
Figure 72 – Extract options in Abaqus/CAE

Since STL format is very commonly used in the modeling and manufacturing industry, there are many software's available to do the post optimization necessary tasks. For the present work the Fusion 360, presented in chapter 3, was used. There the orphan mesh format was converted to 2D drawing and then to 3D body, as shown in Figure 73. After that the structure was, again, converted to STL but now as an 3D body, with a geometry of 6 meters long for 0.6 meters tall and a width of 0.2 meters.

(a)

(b)

(c)
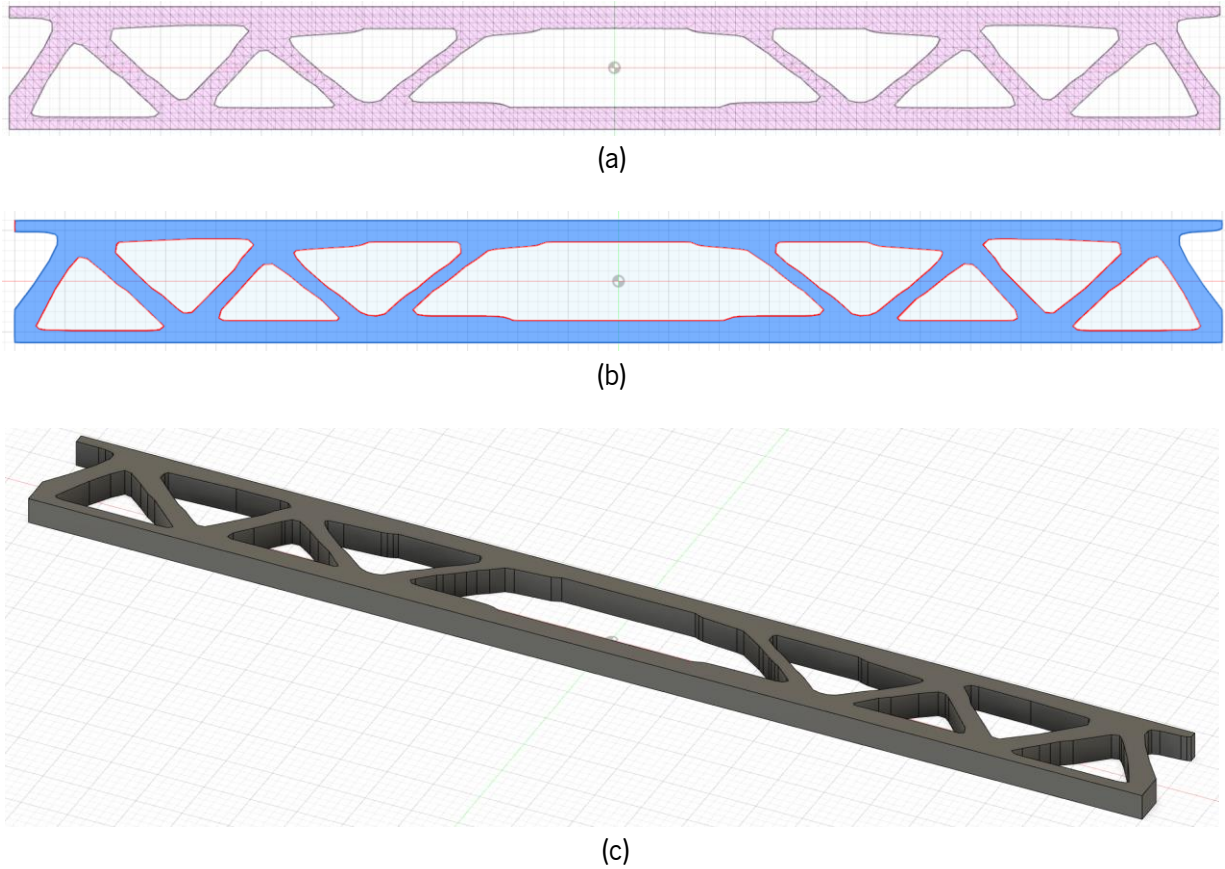
Figure 73– Methodology done in Fusion 360. (a) 2D orphan mesh; (b) 2D drawing; (c) 3D body

After that the Ultimaker Cura as used in order to simulate the 3D printing process. Ultimaker Cura is an open source 3D printing application, that works by slicing the user's model into layers and generating a printer-specific g-code. Once finished the g-code can be sent to the printer for the manufacture of the physical object (All 3DP, 2020). Figure 74 shows the 3D beam in Ultimaker Cura.
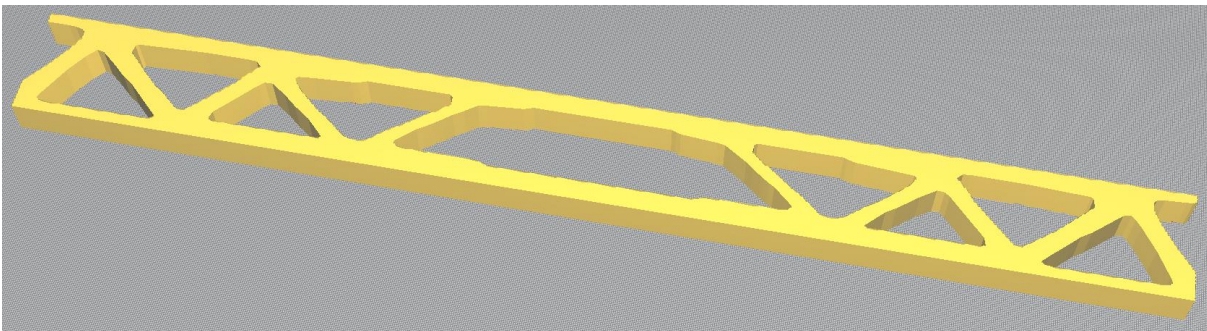
Figure 74 – 3D model of the optimized beam in Ultimaker Cura

Lastly all necessary settings were specified in order to proper simulate the 3D printing process. Of the many options that the program allows the user to use/customize (e.g. geometry of the printer, geometry of the nozzle, properties of the material, layers height, infill density, etc), worth noting that the layers height and infill density were set to 20 millimeters and 100%, respectively.

Three 3D printing processes were simulated, where the only variable that was changed was the diameter of the printed material, in order to simulate different types of printed refinements. Table 19 shows the material diameter values that were considered for the three printing processes. Figure 75 and Figure 76 shows the results of the printing simulations.

Table 19 – 3D printing settings considered

Printing process	Layers height (mm)	Infill density (%)	Material diameter (mm)
1	20	100	25
2	20	100	10
3	20	100	5
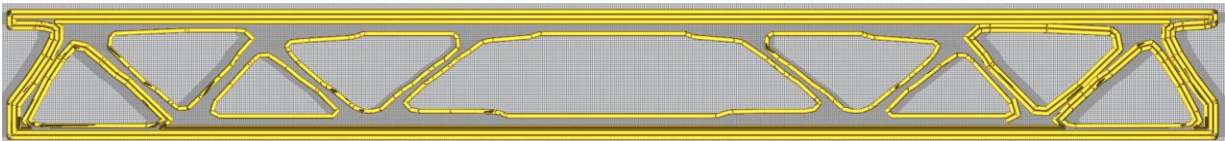
(a)
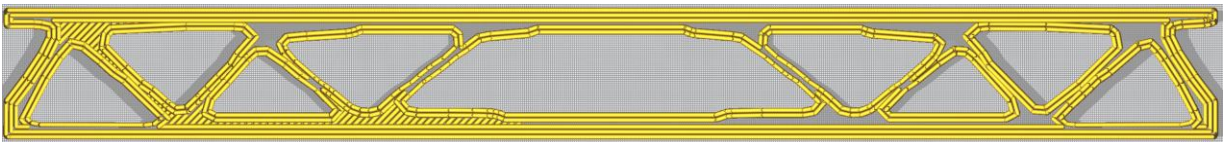
(b)
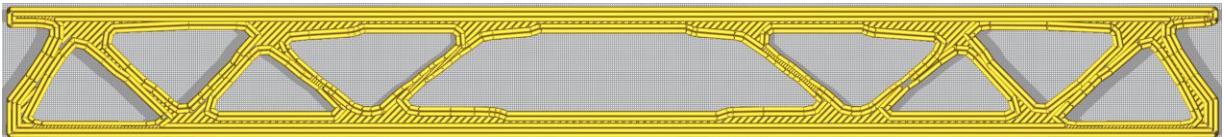
(c)

Figure 75 - 3D printing results for the 25mm diameter.

(a)

(b)

(c)

(d)

(e)

(f)
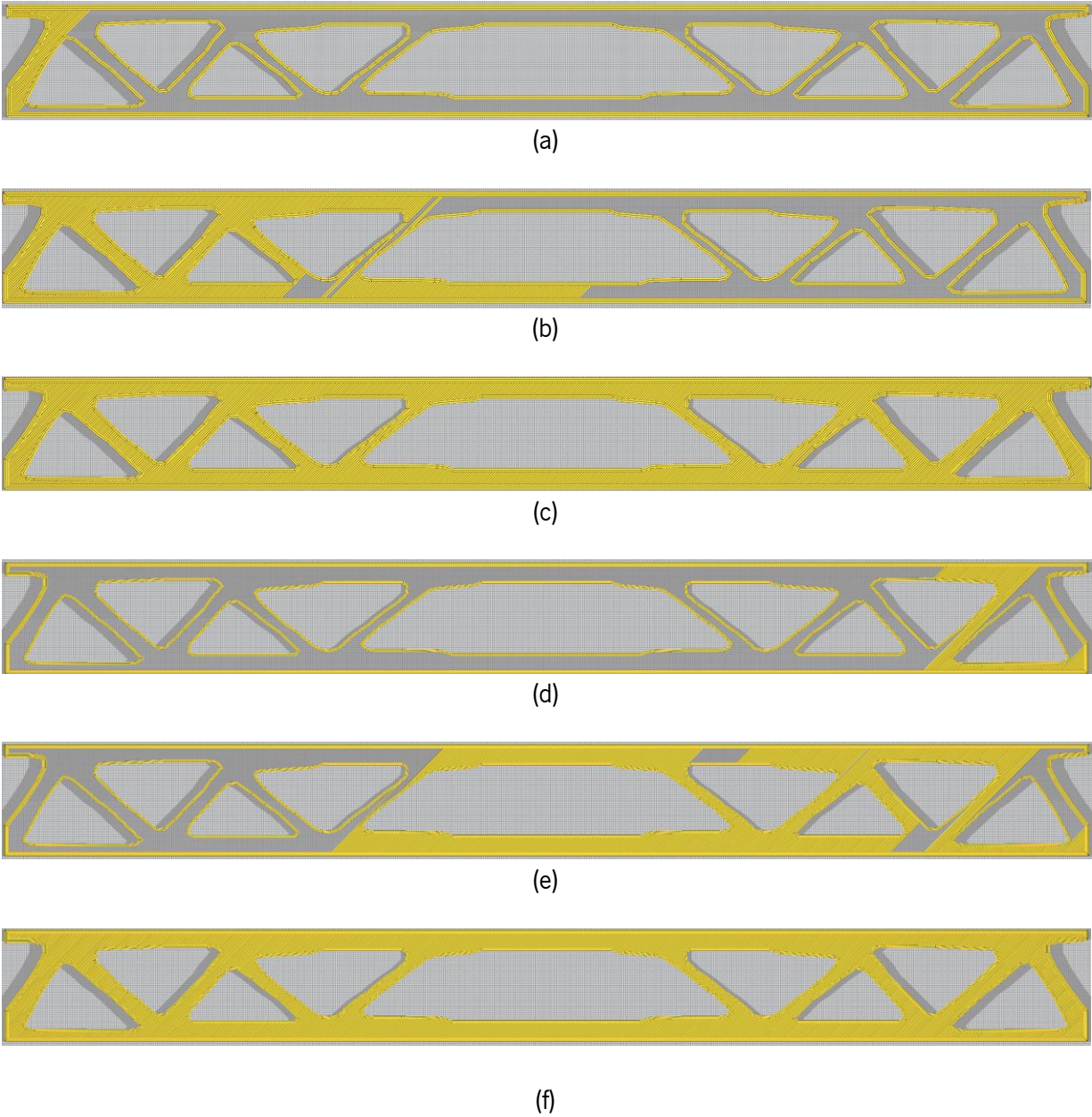
Figure 76 – 3D printing results. (a), (b), (c) material diameter of 10 mm; (d), (e), (f) material diameter of 5 mm.

After looking to Figure 75 and Figure 76 it can be concluded that results for the diameter of 25 mm (simulating a coarse refinement) were not that well achieved, where it can be perfectly notice the separation between the different printed lines, which will certainly have consequences in the structural capacity of the beam. So even though the printing time with the 25 mm diameter was significantly less than the other two the use of this diameter is not recommended.

On the other hand, the results from the 10 and 5 millimeters diameter have in general great definition, giving a feeling of a completely glued/homogeneous structure, so the use of these diameters is recommended. The main different is the printing time, where with the 5 mm diameter takes, approximately, twice the time. In Figure 77 is depicted a 3D view of different moments for the simulations with material the 10 mm diameter.
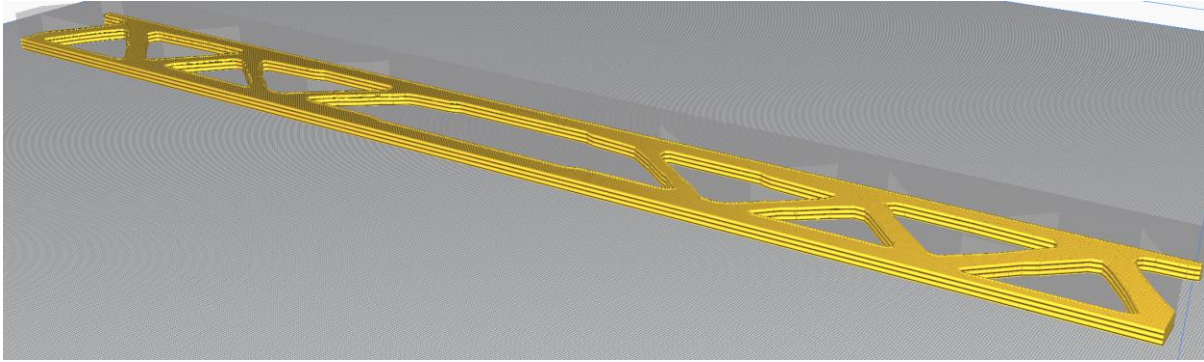
(a)
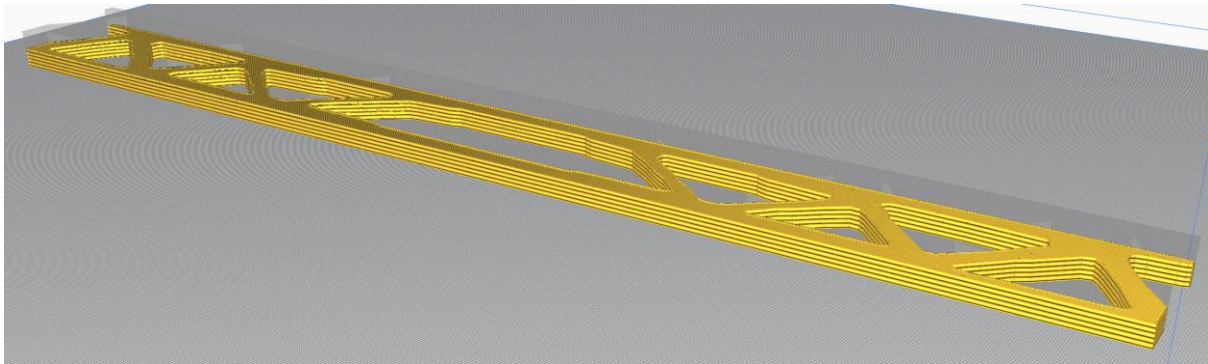
(b)
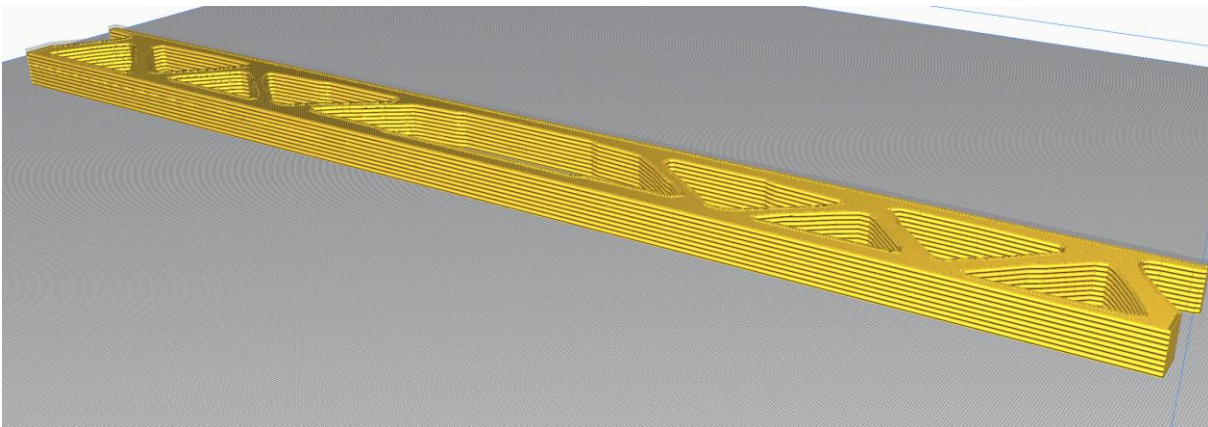
(c)

Figure 77 – 3D view of different moments for the simulations with material diameter of 10 mm

6. CONCLUSIONS AND FUTURE WORK

6.1 Conclusions

Nowadays, where sustainability issues are well established in the major global societal debates, the material efficiency, rational usage of raw materials have become an increasingly critical aspect within the Architecture, Engineering and Construction (AEC) industry. Topology optimization linked with digital manufacturing promises to contributing in mitigating the current negative environmental impacts observed within the construction industry. Although the AEC sector has made some developments within the scope of the digital manufacturing, it is still quite limited to research and innovation areas.

A preliminary study of distinct commercial optimization software was performed. From this analysis, it was concluded that Abaqus/CAE was the most suitable one, since that, even though some limitations, it allowed to carry out all the intended studies.

In the present dissertation, different topology optimizations processes were carried out. Firstly, a study of the influence of H/L ratio and supports conditions was done. For this study were chosen three different heights (0.6, 1.2 and 2 m), and two support conditions (simply and pinned supported). Before the optimization simulations, it was evaluated which were the best mesh refinements, as well as the best variables for the optimization algorithm to be used. After that, in a second stage, nonlinear simulations were carried out in order to proper evaluate the post-crack response of an optimized structure made of fiber reinforced concrete, FRC.

In relation to the study of the influence of H/L ratio and support conditions, it was concluded that the higher the beam height and more the horizontal constraints are, the more prevalent the arch effect and the more closed it will be, consequently making it more stiff, the formation of an arch would be more efficient in terms of minimizing the strain energy and transferring the applied loads to the bearings, turning the structural behavior predominantly under compressive stresses. Even in shallow beams, such as with 0.6 m height, pinned supported, since the horizontal displacements are constrained, the arch effect ist well present in the optimization process. Overall, the optimized shape obtained from the topology optimization provided quality

results, it can also be concluded that both the mesh refinement and the optimization variables and selected algorithm were important to the good results obtained.

The influence of the flexural longitudinal reinforcement in the optimization process was also assessed. For this, five optimization processes were carried out, each one with different amounts of reinforcement (As). From this parametric analysis, it was found that as higher the reinforcement area was, less material will be added to bottom flange of the optimized beam. Furthermore, the optimization results obtained assuming a plane stress state was compared with 3D analysis. Comparing the stresses values with the ones obtained in the 2D optimizations it can be stated that they are very similar, which leads to conclude that the plane stress assumption was correctly applied. Moreover, if the mesh refinement degree is high, the topology optimization will also be performed along the beam's width direction. Therefore, for the 3D analysis both the strain energy and deflection are slightly lower than the ones obtained for the correspondent 2D analysis.

Regarding the nonlinear numerical analysis of the fiber reinforced concrete, FRC, beams, it was assessed the influence of distinct methodologies proposed for defining the tensile constitutive law and their impact in the overall structural performance. For distinct strength classes was observed that the shape of the post-peak tensile law influenced considerably the maximum and ultimate load (i.e. at failure), as well as the rupture mode.

To sum it up, it can be stated that the combination of structural optimization with the intelligent usage of materials with high capacity of redistributing efforts (e.g. FRC materials) can be an excellent way of building lighter and more efficient structures. Moreover, the interoperability between advanced numerical tools under the scope of the FEM and digital fabrication may oblige engineers to rethink the way that they design structures.

6.2 Future works

Future work developments could be divided into short and long-term research. Regarding the short-term research, 3D printed samples and flexural test will be performed, in order to compare the tests results with the ones obtained in Abaqus /CAE simulations. This is a crucial aspect and very interesting to be done, which was not performed due to the shortage of time and the 2020 very particular conjuncture.

Concerning to long-term research would be very interesting to conduct different structural optimization processes considering the nonlinear behavior of the FRC material and make further comparisons with the ones obtained using the current methodology. For this, probably, some external script via MATLAB or other, along with Abaqus capabilities would be necessary, since Abaqus is very limited regarding the nonlinear material models that can be employed in conjunction with the topology optimization module (SIMULIA Abaqus manual 6.14). Furthermore, would be also interesting to consider the printing path and the orthotopic behavior of the FRC material in the optimization process.

7.References

2020 Best 3D Printer Slicer Software (Fall Update) | All3DP. (n.d.). Retrieved January 3, 2021, from https://all3dp.com/1/best-3d-slicer-software-3d-printer/

Abaqus/CAE. (n.d.). *Abaqus CAE - SIMULA™ by Dassault Systèmes®*. Retrieved October 18, 2020, from https://www.3ds.com/products-services/simulia/products/abaqus/abaquscae/

ABB Group. Leading digital technologies for industry — ABB Group. (n.d.). Retrieved December 22, 2020, from https://global.abb/group/en

Abrishambaf, A., Barros, J. A. O., & Cunha, V. M. C. F. (2015). Tensile stress-crack width law for steel fibre reinforced self-compacting concrete obtained from indirect (splitting) tensile tests. *Cement and Concrete Composites*. https://doi.org/10.1016/j.cemconcomp.2014.12.010

Add It Tech Pty Ltd | 3D Printing Services. (n.d.). Retrieved December 22, 2020, from https://www.addittech.com.au/

Allwood, J. M., Ashby, M. F., Gutowski, T. G., & Worrell, E. (2011). Material efficiency: A white paper. *Resources, Conservation and Recycling*, *55*(3), 362–381. https://doi.org/10.1016/j.resconrec.2010.11.002

Anell, L. H. (2015). *"Concrete 3d printer", MSc thesis, Civil engineering, Lund University*.

ASTM F2792-10. (n.d.). Retrieved December 22, 2020, from https://webstore.ansi.org/standards/astm/astmf279210

Austin, S. A., Goodier, C. I., & Robins, P. J. (2005). Low-volume wet-process sprayed concrete: Pumping and spraying. *Materials and Structures/Materiaux et Constructions*, *38*(276), 229–237. https://doi.org/10.1617/14025

Austin, S. A., Robins, P. J., & Goodier, C. I. (1999). The rheological performance of wet-process sprayed mortars. In *Magazine of concrete Research* (Vol. 38, pp. 341–352). https://doi.org/10.1680/macr.1999.51.5.341

Austin, S. A., Robins, P. J., & Goodier, C. I. (2002). Construction and repair with wet-process sprayed concrete and mortar (technical Report). *Concrete Society*.

Autodesk. (n.d.). *Fusion 360 | 3D CAD, CAM, CAE & PCB Cloud-Based Software | Autodesk*. Retrieved October 18, 2020, from https://www.autodesk.com/products/fusion-360/overview

Bachman, D. (2017). Grasshopper : visual scripting for Rhinoceros 3D. In *Industrial Press, Inc.*

Bakhtiari. (1996). *No Title*.

Barbosa. (2017). Reinventing Construction: A Route To Higher Productivity. *McKinsey & Company*, *February*, 168. www.revalue.dk

Behzad Zahabizadeh, João Pereira, Cláudia Gonçalves, V. M. C. F. C. (2020). *Inverse Analysis of Three-Point*

Bending Tests for 3D Printed Fibre Reinforced Mortars.

Bendsøe, M., & Sigmund, O. (2003). *Topology optimization. Theory, methods, and applications. 2nd ed., corrected printing*. https://doi.org/10.1007/978-3-662-05086-6

Bos, Ahmed, Z. Y., Jutinov, E. R., & Salet, T. A. M. (2017). Experimental exploration of metal cable as reinforcement in 3D printed concrete. *Materials*, *10*(11). https://doi.org/10.3390/ma10111314

Bos, F., Wolfs, R., Ahmed, Z., & Salet, T. (2016). Additive manufacturing of concrete in construction: potentials and challenges of 3D concrete printing. *Virtual and Physical Prototyping*, *11*(3), 209–225. https://doi.org/10.1080/17452759.2016.1209867

Buswell, R. A., Soar, R. C., Gibb, A. G. F., & Thorpe, A. (2007). Freeform Construction: Mega-scale Rapid Manufacturing for construction. *Automation in Construction*, *16*(2), 224–231. https://doi.org/10.1016/j.autcon.2006.05.002

Cesaretti, G., Dini, E., De Kestelier, X., Colla, V., & Pambaguian, L. (2014). Building components for an outpost on the Lunar soil by means of a novel 3D printing technology. *Acta Astronautica*, *93*, 430–450. https://doi.org/10.1016/j.actaastro.2013.07.034

Chen, Y., Veer, F., Copuroglu, O., & Schlangen, E. (2019). Feasibility of Using Low CO2 Concrete Alternatives in Extrusion-Based 3D Concrete Printing. *Digital Concrete*, *1*(RILEM International Conference on Concrete and Digital Fabricatiomn), 269–276. https://doi.org/10.1007/978-3-319-99519-9_25

Chu, D. N., Xie, Y. M., Hira, A., & Steven, G. P. (1997). On various aspects of evolutionary structural optimization for problems with stiffness constraints. *Finite Elements in Analysis and Design*. https://doi.org/10.1016/s0168-874x(96)00049-2

D., N. C., Y.M., X., A., H., & G.P., S. (1996). Evolutionary structural optimization for problems with stiffness constraints. *Finite Elements in Analysis and Design*.

Dassault, S. (n.d.). *Abaqus Unified FEA - SIMULIA™ by Dassault Systèmes®*. Retrieved October 18, 2020, from https://www.3ds.com/products-services/simulia/products/abaqus/

Delgado Camacho, D., Clayton, P., O'Brien, W. J., Seepersad, C., Juenger, M., Ferron, R., & Salamone, S. (2018). Applications of additive manufacturing in the construction industry – A forward-looking review. *Automation in Construction*, *89*(August 2017), 110–119. https://doi.org/10.1016/j.autcon.2017.12.031

FIB. (2011). Model Code 2010. In *fib Model Code for Concrete Structures 2010*.

Gerbert, P., Lorenz, M., Rubmann, M., Waldner, M., Justus, J., Engel, P., & Harnisch, M. (2015). Industry 4.0: The future of productivity and growth in manufacturing industries. *BCG Perspective*, 1–20. https://doi.org/10.1007/978-981-13-3384-2_13

Gosselin, C., Duballet, R., Roux, P., Gaudillière, N., Dirrenberger, J., & Morel, P. (2016). Large-scale 3D printing of ultra-high performance concrete - a new processing route for architects and builders. *Materials and Design*, *100*, 102–109. https://doi.org/10.1016/j.matdes.2016.03.097

Grinde, S. (2018). *TOPOLOGY OPTIMIZATION FOR ADDITIVE MANUFACTURING USING SIMP METHOD*.

Hafezolghorani, M., Hejazi, F., Vaghei, R., Jaafar, M. S. Bin, & Karimzade, K. (2017). Simplified damage plasticity model for concrete. *Structural Engineering International*. https://doi.org/10.2749/101686616X1081

Hook. (2016). *Industry 4.0: Building the digital enterprise - Engineering and construction key findings*. 1–36. https://www.pwc.com/gx/en/industries/industries-4.0/landing-page/industry-4.0-building-your-digital-enterprise-april-2016.pdf

Hopkinson, N., Gao, Y., & McAfee, D. J. (2006). Design for environment analyses applied to rapid manufacturing. *Proceedings of the Institution of Mechanical Engineers, Part D: Journal of Automobile Engineering*, *220*(10), 1363–1372. https://doi.org/10.1243/09544070JAUTO309

Huang, X., & Xie, Y. M. (2010). Evolutionary Topology Optimization of Continuum Structures: Methods and Applications. In *Evolutionary Topology Optimization of Continuum Structures: Methods and Applications*. https://doi.org/10.1002/9780470689486

Jipa, A., Bernhard, M., Dillenburger, B., Meibodi, M., & Aghaei-Meibodi, M. (2016). 3D-Printed Stay-in-Place Formwork for Topologically Optimized Concrete Slabs. *2016 TxA Emerging Design + Technology*, *November 2016*, 96–107. internal-pdf://0960461026/Jipa-2017.pdf%0Ahttps://www.research-collection.ethz.ch:443/handle/20.500.11850/237082

Kazemian, A., Yuan, X., Meier, R., & Khoshnevis, B. (2019). A Framework for Performance-Based Testing of Fresh Mixtures for Construction-Scale 3D Printing. *Digital Concrete 2018*, 39–52. https://doi.org/10.1007/978-3-319-99519-9_4

Khoshnevis, B., Bukkapatnam, S., Kwon, H., & Saito, J. (2001). Experimental investigation of contour crafting using ceramics materials. *Rapid Prototyping Journal*, *7*(1), 32–41. https://doi.org/10.1108/13552540110365144

Khoshnevis, Behrokh. (2004). Automated construction by contour crafting - Related robotics and information technologies. *Automation in Construction*, *13*(1), 5–19. https://doi.org/10.1016/j.autcon.2003.08.012

Khoshnevis, Behrokh, Bodiford, M. P., Burks, K. H., Ethridge, E., Tucker, D., Kim, W., Toutanji, H., & Fiske, M. R. (2005). Lunar contour crafting - A novel technique for ISRU-based habitat development. *43rd AIAA Aerospace Sciences Meeting and Exhibit - Meeting Papers*, *January*, 7397–7409. https://doi.org/10.2514/6.2005-538

Khoshnevis, Behrokh, & Dutton. (1998). Innovative rapid prototyping process makes large sized, smooth surfaced complex shapes in a wide variety of materials. *Materials Technology*, *13*(2), 53–56. https://doi.org/10.1080/10667857.1998.11752766

Khoshnevis, Behrokh, Hwang, D., Yao, K. T., & Yeh, Z. (2006). Mega-scale fabrication by Contour Crafting. *International Journal of Industrial and Systems Engineering*. https://doi.org/10.1504/IJISE.2006.009791

Khoshnevis, Behrokh, Yao, K.-T., Hwand, D., & Yeh, Z. (2006). Mega-scale fabrication by contour crafting * Dooil Hwang and Ke-Thia Yao Zhenghao Yeh. *Int. J. Industrial and Systems Engineering*, *1*(3), 301–320.

Krause, M., Otto, J., Bulgakov, A., & Sayfeddine, D. (2018). Strategic optimization of 3D concrete printing using the method of CONPrint3D®. *ISARC 2018 - 35th International Symposium on Automation and Robotics in Construction and International AEC/FM Hackathon: The Future of Building Things*, *July*. https://doi.org/10.22260/isarc2018/0002

Kwon, H. (2002). *Experimentation and analysis of contour crafting (CC) process using uncured ceramic materials :: University of Southern California Dissertations and Theses*. August. http://digitallibrary.usc.edu/cdm/ref/collection/p15799coll16/id/549034

L. Barretoa, B., A. Amarala, C., & T. Pereiraa, C. (2018). ScienceDirect ScienceDirect ScienceDirect ScienceDirect Studying noise measurement and analysis Costing models for capacity optimization in Industry 4 . 0 : Trade-off between used capacity and operational efficiency. *Procedia Manufacturing*, *22*, 533–538. https://doi.org/10.1016/j.promfg.2018.03.078

Le, T. T., Austin, S. A., Lim, S., Buswell, R. A., Law, R., Gibb, A. G. F., & Thorpe, T. (2012a). Hardened properties of high-performance printing concrete. *Cement and Concrete Research*, *42*(3), 558–566. https://doi.org/10.1016/j.cemconres.2011.12.003

Le, T. T., Austin, S. A., Lim, S., Buswell, R. A., Law, R., Gibb, A. G. F., & Thorpe, T. (2012b). Mix design and fresh properties for high-performance printing concrete. *Materials and Structures/Materiaux et Constructions*, *45*(8), 1221–1232. https://doi.org/10.1617/s11527-012-9828-z

Lim;, Buswell, R., Le, T., Wackrow, R., Austin, S. A., Gibb, A., & Thorpe, T. (2011). *Development of a viable concrete printing process*.

Lim, Buswell, R. A., Le, T. T., Austin, S. A., Gibb, A. G. F., & Thorpe, T. (2012a). Developments in construction-scale additive manufacturing processes. *Automation in Construction*, *21*(1), 262–268. https://doi.org/10.1016/j.autcon.2011.06.010

Lim, Le, T., Webster, J., Buswell, R., Austin, S., Gibb, A., & Thorpe, T. (2009). *Fabricating Construction Components using layer manufacturing technology. January*.

Lim, S., Buswell, R. A., Le, T. T., Austin, S. A., Gibb, A. G. F., & Thorpe, T. (2012b). Developments in construction-scale additive manufacturing processes. *Automation in Construction*, *21*(1), 262–268. https://doi.org/10.1016/j.autcon.2011.06.010

Lowke, D., Dini, E., Perrot, A., Weger, D., Gehlen, C., & Dillenburger, B. (2018). Particle-bed 3D printing in concrete construction – Possibilities and challenges. *Cement and Concrete Research*, *112*(November 2017), 50–65. https://doi.org/10.1016/j.cemconres.2018.05.018

Lu, B., Weng, Y., Li, M., Q., Y., L., K.F. Tan, M. J., & Qian, S. (2019). A systematical review of 3D printable cementitious materials. *Construction and Building Materials*, *207*, 477–490. https://doi.org/10.1016/j.conbuildmat.2019.02.144

Malaeb, Z., Hachem, H., Tourbah, A., Maalouf, T., El Zarwi, N., & Hamzeh, F. (2015). 3D Concrete Printing: Machine and Mix Design. *International Journal of Civil Engineering and Technology*, *6*(April), 14–22. http://www.researchgate.net/profile/Farook_Hamzeh/publication/280488795_3D_Concrete_Printing_Machine_and_Mix_Design/links/55b608c308aec0e5f436d4a1.pdf

Marchment, T., Sanjayan, J. G., Nematollahi, B., & Xia, M. (2019). Interlayer Strength of 3D Printed Concrete. In *3D Concrete Printing Technology* (Issue 3). Elsevier Inc. https://doi.org/10.1016/b978-0-12-815481-6.00012-9

McNeel Forum, K. (n.d.). *Karamba material properties - Grasshopper / Karamba3D - McNeel Forum*. Retrieved October 19, 2020, from https://discourse.mcneel.com/t/karamba-material-properties/104665/5

Mechtcherine, V., Grafe, J., Nerella, V. N., Spaniol, E., Hertel, M., & Füssel, U. (2018). 3D-printed steel reinforcement for digital concrete construction – Manufacture, mechanical properties and bond behaviour. *Construction and Building Materials*, *179*, 125–137. https://doi.org/10.1016/j.conbuildmat.2018.05.202

Mechtcherine, V., Nerella, V. N., Will, F., Näther, M., Otto, J., & Krause, M. (2019). Large-scale digital concrete construction – CONPrint3D concept for on-site, monolithic 3D-printing. *Automation in Construction*, *107*(April), 102933. https://doi.org/10.1016/j.autcon.2019.102933

Nerella, V. N. (2016). Studying the Printability of Fresh Concrete for Formwork-Free Concrete Onsite 3D Printing Technology (CONPrint3D). *3D Concrete Printing Technology*, *March*, 333–347. https://doi.org/10.1016/b978-0-12-815481-6.00016-6

Ngo, T. D., Kashani, A., Imbalzano, G., Nguyen, K. T. Q., & Hui, D. (2018). Additive manufacturing (3D printing): A review of materials, methods, applications and challenges. *Composites Part B: Engineering*, *143*(February), 172–196. https://doi.org/10.1016/j.compositesb.2018.02.012

Ogura, H., Nerella, V. N., & Mechtcherine, V. (2018a). Developing and testing of Strain-Hardening Cement-Based Composites (SHCC) in the context of 3D-printing. *Materials*, *11*(8), 1–18. https://doi.org/10.3390/ma11081375

Ogura, H., Nerella, V. N., & Mechtcherine, V. (2018b). Developing and testing of Strain-Hardening Cement-Based Composites (SHCC) in the context of 3D-printing. *Materials*, *11*(8), 10–11. https://doi.org/10.3390/ma11081375

Panda, B., Ruan, S., Unluer, C., & Tan, M. J. (2019). Improving the 3D printability of high volume fly ash mixtures via the use of nano attapulgite clay. *Composites Part B: Engineering*, *165*(November 2018), 75–83. https://doi.org/10.1016/j.compositesb.2018.11.109

Paul, S. C., Tay, Y. W. D., Panda, B., & Tan, M. J. (2018). Fresh and hardened properties of 3D printable cementitious materials for building and construction. *Archives of Civil and Mechanical Engineering*, *18*(1), 311–319. https://doi.org/10.1016/j.acme.2017.02.008

Paul, S. C., van Zijl, G. P. A. G., & Gibson, I. (2017). A review of 3D concrete printing systems and materials properties: current status and future research prospects. *Rapid Prototyping Journal*, *24*(4), 784–798. https://doi.org/10.1108/RPJ-09-2016-0154

Pegna, J. (1997). Exploratory investigation of solid freeform construction. *Automation in Construction*, *5*(5), 427–437. https://doi.org/10.1016/S0926-5805(96)00166-5

Perrot, A., Rangeard, D., & Pierre, A. (2016). Structural built-up of cement-based materials used for 3D-

printing extrusion techniques. *Materials and Structures/Materiaux et Constructions*, *49*(4), 1213–1220. https://doi.org/10.1617/s11527-015-0571-0

Pradhan, R. S. (2019). INDUSTRIAL DESIGN AND CLOUD-BASED 3D VISUALIZATION TOOL – AUTODESK FUSION 360. *International Journal of Engineering Applied Sciences and Technology*. https://doi.org/10.33564/ijeast.2019.v04i04.012

Preisinger, C. (2013). Linking structure and parametric geometry. *Architectural Design*. https://doi.org/10.1002/ad.1564

Puskás, E., & Bohács, G. (2019). Physical Internet – a novel application area for Industry 4.0. *International Journal of Engineering and Management Sciences*. https://doi.org/10.21791/ijems.2019.1.19.

Querin, O. M., Young, V., Steven, G. P., & Xie, Y. M. (2000). Computational efficiency and validation of bi-directional evolutionary structural optimization. *Computer Methods in Applied Mechanics and Engineering*. https://doi.org/10.1016/S0045-7825(99)00309-6

Rahul, A. V., Santhanam, M., Meena, H., & Ghani, Z. (2019). 3D printable concrete: Mixture design and test methods. *Cement and Concrete Composites*, *97*, 13–23. https://doi.org/10.1016/j.cemconcomp.2018.12.014

Readts, W. (2017). *Investigation into properties of fibre reinforced concrete in extrusion based adaptive manufacturing*. 92. http://dx.doi.org/10.1016/j.cemconcomp.2017.04.005

Rodrigues, P. (2014). *Combined topology and stacking sequence optimization of composit laminated structures for structural performance measure*.

Rutten, D. (2013). Galapagos: On the logic and limitations of generic solvers. *Architectural Design*. https://doi.org/10.1002/ad.1568

Sahin, R., & Tosun, Y. (2019). Developments of 3D Concrete Printing Process. *Development of 3D Concrete Printing Process*, April.

Sanjayan, J. G., & Nematollahi, B. (2018). 3D concrete printing for structural applications. *Spool*, *6*(2), 5–10. https://doi.org/10.7480/spool.2019.2.4366

Santos, B. P., Alberto, A., Lima, T., & Santos, B. (2018). Indústria 4.0: Desafios E Oportunidades. *Revista Produção e Desenvolvimento*, *4*, 111–124.

Shobeiri, V., & Ahmadi-Nedushan, B. (2019). TOPOLOGY OPTIMIZATION OF PRETENSIONED CONCRETE BEAMS CONSIDERING MATERIAL NONLINEARITY. In *INTERNATIONAL JOURNAL OF OPTIMIZATION IN CIVIL ENGINEERING Int. J. Optim. Civil Eng*.

SIEMENS. (2017). *Conceito de Indústria 4.0*. http://seer.spo.ifsp.edu.br/index.php/posgere/article/view/120

Sigmund, O. (2001). A 99 line topology optimization code written in matlab. *Structural and Multidisciplinary Optimization*. https://doi.org/10.1007/s001580050176

Sigmund, O., & Petersson, J. (1998). Numerical instabilities in topology optimization: A survey on procedures

dealing with checkerboards, mesh-dependencies and local minima. *Structural Optimization*. https://doi.org/10.1007/BF01214002

SIMULIA, A. documentation, & 6.14. (n.d.). *Abaqus 6.14 Documentation*. Retrieved October 18, 2020, from http://ivt-abaqusdoc.ivt.ntnu.no:2080/texis/search/?query=wetting&submit.x=0&submit.y=0&group=bk&CDB=v6.14

Smarsly, K., Peralta, P., Luckey, D., Heine, S., & Ludwig, H. (2020). *BIM-based concrete printing*. 1–11.

Soltan, D. G., & Li, V. C. (2018). A self-reinforced cementitious composite for building-scale 3D printing. *Cement and Concrete Composites*, *90*, 1–13. https://doi.org/10.1016/j.cemconcomp.2018.03.017

Søndergaard, A., & Per Dombernowsky. (2011). Unikabeton Prototype. *Making Digital Architecture*, 7.

The Fourth Industrial Revolution - CADM. (n.d.). Retrieved December 22, 2020, from https://www.cadm.com/the-fourth-industrial-revolution/

Van Der Putten, J., De Schutter, G., & Van Tittelboom, K. (2019). The Effect of Print Parameters on the (Micro)structure of 3D Printed Cementitious Materials. *RILEM International Conference on Concrete and Digital Fabrication*, *1*(RILEM Bookseries), 234–244. https://doi.org/10.1007/978-3-319-99519-9_22

Wonoto, N., & Blouin, V. (2018). Integrating grasshopper and matlab for shape optimization and structural form-finding of buildings. *Computer-Aided Design and Applications*. https://doi.org/10.14733/cadaps.2019.1-12

Yang, X. Y., Xie, Y. M., Steven, G. P., & Querin, O. M. (1999). Bidirectional evolutionary method for stiffness optimization. *AIAA Journal*. https://doi.org/10.2514/2.626

Yu, J., & Leung, C. K. Y. (2019). Impact of 3D printing direction on mechanical performance of strain-hardening cementitious composite (SHCC). In *RILEM Bookseries*. https://doi.org/10.1007/978-3-319-99519-9_24

Zahabizadeh, B., Cunha, V.M.C.F., Pereira, J., Gonçalves, C. (2019). The effect of loading direction on the compressive behaviour of a 3D printed cement-based material. In *Towards a Resilient Built Environment Risk and Asset Management* (pp. 1658–1665).

Zareiyan, B., & Khoshnevis, B. (2017). Interlayer adhesion and strength of structures in Contour Crafting - Effects of aggregate size, extrusion rate, and layer thickness. *Automation in Construction*, *81*(March), 112–121. https://doi.org/10.1016/j.autcon.2017.06.013

Zhang, J., & Khoshnevis, B. (2013). Optimal machine operation planning for construction by Contour Crafting. *Automation in Construction*, *29*, 50–67. https://doi.org/10.1016/j.autcon.2012.08.006

Zhang, X., Li, M., Lim, J. H., Weng, Y., Tay, Y. W. D., Pham, H., & Pham, Q. C. (2018). Large-scale 3D printing by a team of mobile robots. *Automation in Construction*, *95*(August), 98–106. https://doi.org/10.1016/j.autcon.2018.08.004

8. ATTACHMENTS

8.1 Attachment A

https://vimeo.com/502187751

https://vimeo.com/502187782

https://vimeo.com/502187817

8.2 Attachment B

https://vimeo.com/502106538

https://vimeo.com/502106576

https://vimeo.com/502106731

8.3 Attachment C

https://vimeo.com/502105650

8.4 Attachment D

https://vimeo.com/502190713